UNIVERSITAT POLITÈCNICA DE CATALUNYA BARCELONATECH

Fluorescence quantum yield and the open circuit voltage in perovskite solar cells

Mariia Kramarenko

FLUORESCENCE QUANTUM YIELD AND THE OPEN CIRCUIT VOLTAGE IN PEROVSKITE SOLAR CELLS

Mariia KRAMARENKO

Under the supervision of

Prof. Jordi MARTORELL

Submitted this thesis in partial fulfilment

of the requirements of the degree of

DOCTOR

by the

UNIVERSITAT POLITÈCNICA DE

CATALUNYA

BARCELONA, 2023

Acknowledgments

First, I would like to acknowledge and thank Jordi Martorell and ICFO for providing me with an opportunity to conduct my research and complete my doctoral degree.

The completion of this Ph.D. would not have been possible without the guidance and support of my advisors, Jordi Martorell and Johann Toudert. I am grateful for their time, effort, and understanding in helping me succeed in my studies. Their guidance helped me in all the time of research and writing of this thesis.

Besides my advisors, I would like to thank present and former members of the Organic Nanostructured Photovoltaics group for their cooperation, continuous support and stimulating discussions. I express special thanks to Catarina Ferreira, Guillermo Martinez-Denegri, Fransico Bernal, Constanza Sansierra and Hui Zhang for assistance with theoretical and experimental studies. Additionally, I would like to express gratitude to Gregory Kozyreff, who helped me develop a theoretical model during my stay at ULB.

My work would not be possible without the support of all ICFO departments, in particular, the training provided by Johann Osmond and Vittoria Finazzi. I also appreciate all the support I received from the maintenance team on solving various issues faced during my research and mechanical workshop for providing solutions to different problems. My sincere thanks also go to the Academic Affairs and Human Resources teams for providing administrative assistance during the period of my Ph.D.

Finally, I am grateful to my family and friends for their encouragement and support throughout my doctoral degree.

List of publications derived from this thesis

1. **Kramarenko, M.**; Ferreira, C. G.; Martínez-Denegri, G.; Sansierra, C.; Toudert, J.; Martorell, J. Relation Between Fluorescence Quantum Yield and Open-Circuit Voltage in Complete Perovskite Solar Cells, Sol. RRL, 2020, 4, 1900554.
2. Zhang, H.; **Kramarenko, M**.; Martínez-Denegri, G.; Osmond, J.; Toudert, J.; Martorell, J. Formamidinium Incorporation into Compact Lead Iodide for Low Band Gap Perovskite Solar Cells with Open-Circuit Voltage Approaching the Radiative Limit. ACS Appl. Mater. Interfaces, 2019, 11 (9), 9083–9092.
3. **Kramarenko, M.;** Ferreira, C. G.; Toudert, J.; Martorell, J. Photon recycling and antireflection dielectric multilayers for achieving ultimate efficiencies in planar geometry perovskite solar cells. (in preparation)

Other publications

1. Zhang, H.; **Kramarenko, M.**; Osmond, J.; Toudert, J.; Martorell, J. Natural Random Nanotexturing of the Au Interface for Light Backscattering Enhanced Performance in Perovskite Solar Cells. ACS Photonics, 2018, 5, 6, 2243-2250.
2. Martínez-Denegri, G.; Colodrero, S.; **Kramarenko, M.**; Martorell, All-Nanoparticle SnO2/TiO2 Electron-Transporting Layers Processed at Low Temperature for Efficient Thin-Film Perovskite Solar Cells J. ACS Appl. Energy Mater., 2018, 1, 10, 5548-5556.
3. Ferreira, C. G.; Martínez-Denegri, G.; **Kramarenko**, **M.**; Toudert, J.; Martorell J., Light Recycling Using Perovskite Solar Cells in a Half-Cylinder Photonic Plate for an Energy Efficient Broadband Polarized Light Emission, Adv. Photonics Res., 2021, 2, 10, 2100077.
4. Liu, Q.; Toudert, J.; Li, T.; **Kramarenko**, **M.**; Martínez-Denegri, G.; Ciammaruchi, L.; Zhan, X.; Martorell J., Inverse Optical Cavity Design for Ultrabroadband Light Absorption Beyond the Conventional Limit in Low-Bandgap Nonfullerene Acceptor–Based Solar Cells Adv. Energy Mater., 2019, 9, 20, 1900463.
5. Martínez-Denegri, G.; Ferreira, C. G.; Ruiz-Preciado, M. A.; Fassl, P; **Kramarenko**, **M.**; Paetzold, U. W.; Martorell J., Wide Bandgap Perovskite Photovoltaic Cells for Stray Light Recycling in a System Emitting Broadband Polarized Light, Adv. Energy Mater., 2022, 12, 36, 2201473.

Resum

Per mitigar la crisi energètica i climàtica que ja estem enfrontant i abordar l'augment del consum d'energia, és fonamental fomentar estratègies de transició energètica. L'èxit de la transició energètica depèn en gran menera de poder transformar el sector energètic mundial de fonts basades en combustibles fòssils a fonts d'emissió de diòxid de carboni neutres o zero. Un estudi de dècades sobre la fotovoltaica ha produït diverses generacions de tecnologies de conversió d'energia solar que no emeten gasos d'efecte hivernacle ni contaminació de l'aire quan funcionen. Tanmateix, tenint en compte que el sol és la font d'energia més abundant del nostre planeta, en comparació amb els combustibles fòssils, l'ús de la fotovoltaica és encara molt limitat. En aquesta transició dels combustibles fòssils a la fotovoltaica, és essencial millorar l'assequibilitat combinada amb una alta eficiència. En els darrers anys, les cèl·lules solars de perovskita s'han convertit en la tecnologia fotovoltaica de pel·lícula prima més destacada per proporcionar una alta eficiència simultàniament a un baix cost. En aquesta tesi, estudiem cèl·lules solars basades en perovskites i rutes òptiques per maximitzar la seva eficiència de conversió d'energia. El límit teòric per convertir la llum solar en electricitat mitjançant l'efecte fotovoltaic va ser establert per primera vegada per William Shockley i Hans-Joachim Queisser el 1961 basant-se en el principi de l'equilibri detallat. Segons el seu treball, una cèl·lula solar pot assolir una eficiència limitadora si s'eliminen tots els mecanismes de pèrdua i el rendiment quàntic de fluorescència és igual a la unitat. L'eficiència de conversió de totes les tecnologies fotovoltaiques encara és considerablement inferior al límit d'eficiència de Shockley - Queisser, però les basades en perovskita han demostrat propietats optoelectròniques excepcionals i rendiments quàntics de fluorescència elevats, que poden ajudar a apropar la seva màxima eficiència fotovoltaica a aquest límit. En aquesta tesi, proporcionem diverses rutes òptiques per optimitzar els paràmetres fotovoltaics de les cèl·lules solars de perovskita, posant un èmfasi especial en la tensió de circuit obert estudiant la seva relació amb l'absorció i emissió de fotons per part de la capa de perovskita.

Aquesta tesi està organitzada en cinc capítols. El capítol 1 serveix com a introducció, que inclou una discussió sobre la demanda mundial actual d'energia i les tecnologies fotovoltaiques disponibles, centrant-se més en les basades en materials perovskites. El límit d'eficiència de Shockley-Queisser i el mecanisme de pèrdua de potència també es descriuen en aquest capítol. Al capítol 2, analitzem la relació entre la tensió de circuit obert i el rendiment quàntic de fluorescència en cèl·lules solars basades en perovskita, tant teòricament com

experimentalment, i discutim la desviació observada del comportament previst. El capítol 3 descriu el nou mètode de fabricació de perovskites d'alta qualitat amb bandes buides baixes i gran mida de gra. El mètode de creixement compacte de dos passos amb plantilla PbI_2 va facilitar l'assoliment de cèl·lules solars amb un alt rendiment quàntic de fluorescència i tensió de circuit obert. Al capítol 4, hem desenvolupat un model i un algorisme d'optimització per trobar les estructures òptiques òptimes per millorar òpticament els paràmetres fotovoltaics per a diferents cèl·lules solars de perovskita de banda bretxa. Els resultats teòrics d'aquest capítol suggereixen que una simple multicapa dielèctrica col·locada a la part superior del substrat de la cèl·lula solar pot millorar simultàniament la tensió de circuit obert i el corrent de curtcircuit, donant lloc a un guany relatiu d'eficiència de conversió de potència superior al 4%. Finalment, en el capítol 5, s'implementa experimentalment el concepte estudiat teòricament en el capítol anterior. La multicapa dielèctrica es fabrica i es col·loca a sobre d'una cèl·lula solar de perovskita, donant com a resultat una tensió de circuit obert millorada i una eficiència de conversió d'energia.

Abstract

To mitigate the energy and climate crisis we are already facing and address the increasing energy consumption, it is essential to foster energy transition strategies. The energy transition success largely depends on being able to transform the global energy sector from fossil fuel-based to neutral or close to zero carbon dioxide emission sources. A decades-long study of photovoltaics has produced several generations of solar energy conversion technologies that do not emit greenhouse gases or air pollution when they operate. However, considering the sun is our planet's most abundant energy source, when compared to fossil fuels, the use of photovoltaics is still very limited. In such a transition from fossil fuels to photovoltaics, it is essential to enhance affordability combined with high efficiency. In recent years, perovskite solar cells have emerged as the most prominent thin-film PV technology to provide high efficiency simultaneously at a low cost. In this thesis, we study perovskite-based solar cells and optical routes to maximise their power conversion efficiency. The theoretical limit for converting sunlight into electricity by the photovoltaic effect was first established by William Shockley and Hans-Joachim Queisser in 1961 based on the principle of detailed balance. According to their work, a solar cell can reach a limiting efficiency if all loss mechanisms are eliminated and the fluorescence quantum yield is equal to unity. The conversion efficiency for all PV technologies is still considerably lower than the Shockley – Queisser efficiency limit, but perovskite-based ones have demonstrated outstanding optoelectronic properties and high fluorescence quantum yields, which may help get their maximum PV efficiency closer to such limit. In this thesis, we provide several optical routes to optimise the photovoltaic parameters of perovskite solar cells, placing a special emphasis on the open circuit voltage by studying its relation to the absorption and emission of photons by the perovskite layer.

This thesis is organised into five chapters. Chapter 1 serves as an introduction, which includes a discussion of the current world energy demand and available photovoltaic technologies, focusing more on the ones based on perovskite materials. The Shockley – Queisser efficiency limit and power loss mechanism are also described in this chapter. In Chapter 2, we analyse the relationship between open circuit voltage and fluorescence quantum yield in perovskite-based solar cells, both theoretically and experimentally, and discuss the observed deviation from the predicted behaviour. Chapter 3 describes the new fabrication method of high-quality perovskites with low band gaps and big grain size is described. The

two-step compact PbI_2-templated growth method facilitated the achievement of solar cells with high fluorescence quantum yield and open circuit voltage. In Chapter 4, we developed a model

and optimisation algorithm to find the optimum photonic structures to optically enhance the photovoltaic parameters for different band gap perovskite solar cells. Theoretical results from this chapter suggest that a simple dielectric multilayer placed on top of the substrate of the solar cell can simultaneously improve the open circuit voltage and short circuit current, resulting in a relative gain of power conversion efficiency larger than 4%. Finally, in Chapter 5, the concept theoretically studied in the previous chapter is experimentally implemented. The dielectric multilayer is fabricated and placed on top of a perovskite solar cell, resulting in an enhanced open-circuit voltage and power conversion efficiency.

Table of Content

List of figures

List of tables

List of Abbreviations

A(E, θ)	Absorbance
B(E)	Blackbody radiation
BCP	Bathocuproine
C60	Buckminsterfullerene
CZTSS	Copper zinc tin sulphur selenide
DM	Dielectric multilayer
DSSC	Dye-sensitised solar cell
E	Photon energy
E_g	Band gap
e-h	Electron-Hole
EQE	External quantum efficiency
ETL	Electron-transporting layer
FF	Fill factor
FTO	Fluorine-doped tin oxide
HTL	Hole-transporting layer
ITO	Indium tin oxide
J_0	Dark saturation current
J_{sc}	Short-circuit current
k	Boltzmann constant
OPV	Organic photovoltaics
PCBM	Phenyl-C61-butyric acid methyl ester

PCE	Power conversion efficiency
PLQY	Fluorescence quantum yield
PTAA	Poly(triaryl amine)
PV	Photovoltaic
PVK	Perovskite
q	Elementary charge
R_s	Series resistance
R_{sh}	Shunt resistance
S(E)	Sun radiation
SEM	Scanning electron microscope
S-Q	Shockley and Queisser
T_c	Temperature of the solar cell
TCO	Transparent conductive oxide
TMM	Transfer market method
V_{oc}	Open-circuit voltage
$V_{oc,rad}$	Radiative open-circuit voltage
XRD	X-ray powder diffraction
δV	Voltage loss
η_{int}	Internal quantum yield
θ	Angle of incidence
6LDM	6-layer dielectric multilayer

Chapter 1

Introduction

1.1 World energy demand, energy sources and prospects of their usage

Electricity demand has changed the course of humanity over the past few decades. Not only have new sources of electrical energy been deployed, but their share in world electrical energy production has also increased. The annual global energy consumption is estimated at 580 million terajoules. Still, world energy obtained from fossil fuels is 8%. Oil is the largest energy source, followed by coal and natural gas. For now, most of the increase in global energy consumption will be covered by burning more coal and gas, which is critical to the environment as it releases enormous amounts of CO_2 into the atmosphere. Other well-known drawbacks and repercussions of using fossil fuels include: they are non-renewable. Therefore humanity cannot rely on them indefinitely, and any incident involving fossil fuels is usually disastrous for the environment. Burning fossil fuels is considered to be the main contributor to climate change. This makes the development of green energy sources absolutely essential.

Between 2011 and 2030, renewable energy is expected to grow from 2 to 6 per cent of global primary energy use. However, this projected increase in the use of renewable energy will not be enough to cover the worldwide increase in energy demand. While renewable energy's share of the global market is on the rise – the use of coal and gas still remains much higher. Consequently, alternatives to completely transform the global energy system are needed. Currently, Europe is facing another energy-related problem, which is its dependence on fossil fuels provided by external suppliers causing price increases for all consumers, from industry to private households. Reducing reliance on fossil fuels and transitioning to low-carbon alternatives can make the European economy more sustainable. European countries should work together to achieve these two goals.

Global energy demand and energy-related carbon emissions will continue to rise through 2050. According to the World Economic Forum, the low-carbon and renewable energy sources and technologies needed to achieve fast and deep decarbonisation currently exist. A renewable energy source means energy that is sustainable, it cannot run out, or is endless, like the sun, wind, hydro, geothermal and biomass. For example, nuclear-generated electricity is not

renewable, but it is close to zero-carbon, which means its generation emits low levels or almost no CO_2, just like renewable energy sources. But renewable sources are more sustainable and reliable in the long run. The challenge is to make them energy-efficient and to apply them at a high pace and scale, but there is still a long way to go. Solar energy is one of the most abundant and easily accessible energy sources, and photovoltaics, which convert sunlight directly into electricity, is one of the most promising renewable technologies. Unlike hydro or wind energy, which requires specific conditions for the installation of turbines or dams, solar panels are more versatile and can be installed anywhere where sunlight reaches them. The environmental impact of solar cells is also low compared to wind energy, which creates low-level noise, and hydro energy, which requires flooding specific areas, both affecting wildlife. The only obstruction on the usage of solar cells is their limited power conversion efficiency. Conventional solar panels have an efficiency varying from 15% to 20 %. Our work is focused on overcoming the fundamental limitations on the efficiency of photovoltaic devices, particularly solar cells, hence, making this technology more energy-efficient and advantageous for widespread implementation.

1.2 The Shockley–Queisser efficiency limit for the photovoltaic conversion

The first approach and one of the most fundamental studies to establish the maximum theoretical power conversion efficiency of sunlight to electricity by the photovoltaic effect was performed by William Shockley and Hans-Joachim Queisser in 1961. In this pioneering work, the authors discussed the performance limit of p-n junction solar cells, which are photovoltaic devices based on the junction of p-type and n-type semiconductors. In such a junction, there exists an electric field which is formed as electrons move from the positive p-side to the n-side of the junction while holes move in the opposite direction. When light is incident on one of such junctions, energy from the photons can be transferred to the electrons that are transferred to a higher energy state as the conduction band, leaving behind a "hole" in the valence band, thus creating an electron-hole pair (e-h pair). The energy difference between the conduction and valence bands is known as the band gap, which sets an upper limit for the electrical potential or the open circuit voltage (V_{oc}) of the solar cell. Only photons with energy equal to or higher than the band gap can be absorbed by the semiconductor. The photogenerated charge carriers populate the valence and conduction bands, provided they are not trapped by mid-gap localised energy states arising from defects in the lattice, which may be caused by structural distortions or material impurities of the such lattice. Electrons in the conduction band and holes

in the valence band are free to move through the material, a displacement may result in a non-vanishing current flowing through the cell in a short circuit. The power conversion efficiency (PCE) of a solar cell can be shown to be determined by the product of the short-circuit current density (J_{sc}), the open-circuit voltage, and a fill factor (FF). The fill factor is defined as the ratio of the maximum power from the solar cell to the product of open-circuit voltage and short-circuit current.

Under the assumption that both the sun and the cell are black body radiation emitters and applying a detailed balance in steady-state, Shockley and Queisser (S-Q) established the upper limit in the light to electrical current conversion efficiency for such photovoltaic devices. This upper limit is reached when the only recombination mechanism for the e-h is the radiative one. S-Q assumed a device employing the photoelectric effect with a single cut-off frequency. Such efficiency upper limit for solar cell energy conversion is linked to the energy gap, certain geometrical factors such as the solid angle of the sunlight and the angle of the emitted radiation, and other parameters. The probability of absorbing a photon to create an electron-hole pair is approximated to unity in the S-Q model as well. Another important assumption considered in the S-Q model is a step-function-like absorption for the semiconductor, being one above the band gap (E_g) and 0 below the band gap at the temperature of the cell: T_c. According to detailed balance, in thermal equilibrium, each process of e-h pair generation or recombination has to be compensated by an equivalent reverse process. At steady state, this can be written in terms of current densities equality:

$$J_{ph} + J_{rg} - J_r(V) - J_{dg} - J_d(V) - J(V) = 0 \quad (1.1)$$

The different terms in this equation are described as follows. The photogenerated current J_{ph} corresponds to the e-h pair generation due to solar radiation:

$$J_{ph} = q \iint A(E,\theta)S(E)d\theta dE \quad (1.2)$$

where E is the photon energy, q is the elementary charge, A(E, θ) is the absorbance by the active material of the cell and S(E) is the sun radiation spectrum.

The blackbody-generated current J_{rg} corresponds to the e-h pair generation due to radiation, other than sun photons, surrounding the cell:

$$J_{rg} = q \iint A(E,\theta)B(E)d\theta dE \quad (1.3)$$

where B(E) is the blackbody radiation at temperature T_c.

The radiative recombination current $J_r(V)$ corresponds to the loss of e-h pairs due to radiative recombination under the voltage V:

$$J_r(V) = J_r(0)e^{\frac{qV}{kT_c}} \tag{1.4}$$

where q is the elementary charge and k is the Boltzmann constant.

When there is no voltage applied and the cell is in thermal equilibrium with the surrounding bath at T_c, the rate of emission of photons due to recombination must be exactly equal to the rate of photon absorption:

$$J_r(0) = J_{rg} \tag{1.5}$$

The J_{dg} term corresponds to the direct non-radiative e-h pair generation. Non-radiative recombination current $J_d(V)$ corresponds to the loss of e-h pairs due to direct non-radiative recombination under the voltage V.

$$J_d(V) = J_d(0)e^{\frac{qV}{kT_c}} = J_{dg}e^{\frac{qV}{kT_c}} \tag{1.6}$$

The current density J(V) is the total current density in the cell, which using **Eqs.** (1.2 -1.6), it can be shown to be:

$$J(V) = J_0\left(e^{\frac{qV}{kT_c}} - 1\right) - J_{sc} \tag{1.7}$$

where J_{sc} is the cell's short circuit current density that fulfils $J_{sc} = J_{ph}$ if charge collection by the contacts is perfect, while J_0 is the saturation current density that relates to the external fluorescence quantum yield (PLQY) of the cell, which is a ratio of the number of photons emitted by the active layer and escaping the cell to the number of incident photons absorbed by the semiconductor, according to:

$$J_0 = J_{rg} + J_{dg} = \frac{J_{rg}}{PLQY} \tag{1.8}$$

When the cell is under open-circuit conditions, it delivers the open-circuit voltage V_{oc} and $J(V_{oc}) = 0$, so that according to **Eq. (1.7)**:

$$V_{oc} = \frac{kT_c}{q}\ln\left(\frac{PLQY\,J_{sc}}{J_{rg}} + 1\right) \approx \frac{kT_c}{q}\ln\left(\frac{J_{sc}}{J_{rg}}\right) + \frac{kT_c}{q}\ln(PLQY) \tag{1.9}$$

or

$$V_{oc} = V_{oc,rad} + \frac{kT_c}{q}\ln(PLQY) \tag{1.10}$$

where the radiative open-circuit voltage $V_{oc,rad}$ is:

$$V_{oc\,rad} = \frac{kT_c}{q}\ln\left(\frac{J_{sc}}{J_0}\right) \tag{1.11}$$

The V_{oc} as well as PCE of the solar are found to be dependent on the PLQY. The S-Q model predicts that a planar geometry single junction solar cell where the only loss mechanism is the radiative recombination (PLQY=100%), it will exhibit a maximum efficiency of 30%. When taking into account the global solar spectra AM 1.5 instead of a 6000K black-body spectrum approximation, as reported by Green, the predicted maximum power conversion efficiency for a single junction planar geometry solar cell becomes 33.7% at 1.34 eV band gap. When this figure is compared to the maximum efficiency achievable for a system operating between two heat sources at 6000K and 300K based on the second law of thermodynamics, the efficiency estimated by the S-Q model is rather low. This limitation arises from the presence of several loss mechanisms, which affect the photovoltaic parameters of the solar cells.

A first classification of such loss mechanisms is to separate them as providing extrinsic and intrinsic losses. The extrinsic losses, such as parasitic absorption and cell geometry, which includes undesired reflections and contact shadowing, can substantially limit the J_{sc}. However, they are theoretically avoidable and consequently are not considered when calculating the fundamental limiting efficiency. Such losses can be avoided by careful selection of materials used in the cell to minimise parasitic absorption, anti-reflection coatings can also be implemented to improve the light transmittance to the active material, which will bring the J_{sc} of an actual solar cell closer to the efficiency limit.

The intrinsic losses have a strong effect on both the J_{sc} and the V_{oc} of the device. The non-radiative recombination limits the PLQY of the solar cell and is linked to the presence of defects in the bulk of the active material and at the interfaces. This loss mechanism is not taken into account in the S-Q model as it can be minimised by improving the semiconductor quality. The conversion of thermal energy into electrical work requires some energy to be sacrificed to the cold reservoir and hence will always incur an energy penalty, which is called a Carnot factor, namely Carnot loss. According to Kirchoff's law, absorbers must also be emitters and as such cell emission further reduces conversion efficiency, as any photon which does not produce the electron-hole pair is counted as a loss. The thermalisation loss corresponds to thermalisation down to the bandgap energy of photo-generated charge carriers excited with more energy than the one corresponding to the band gap. The imperfect absorption loss is due to the mismatch between the broad solar spectrum and the relatively narrow absorption of a single bandgap, which means that the photons with energy is below the bandgap are not absorbed by the active material. Finally, the Boltzmann loss, also called an entropy loss, arises from the mismatch

between the photon absorption and emission angles. Such inequality contributes to an entropy generation process. The relative contribution of the imperfect absorption loss, the thermalisation loss, the emission loss, the Carnot loss and the Boltzmann loss as a function of the bandgap of active material, illustrated by Hirst et. al, is depicted in **Figure 1.1**.

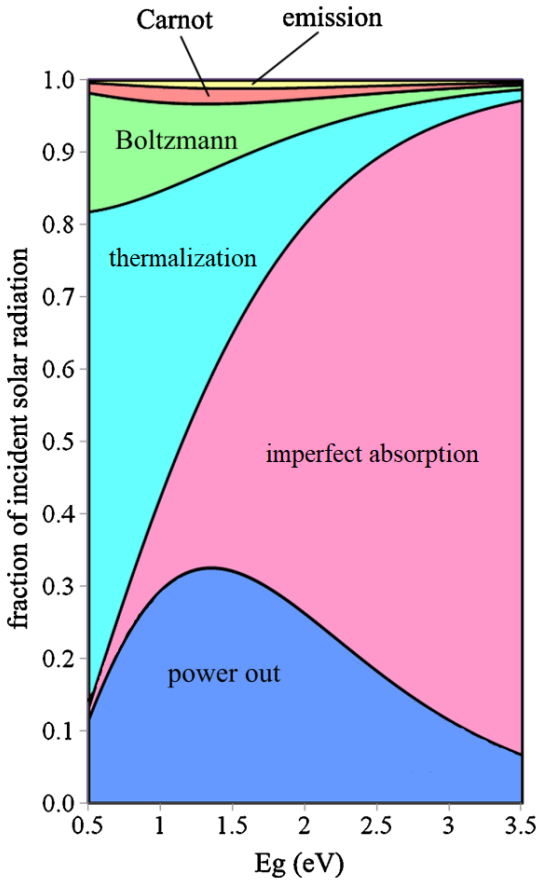

Figure 1.1 Intrinsic loss processes. The Carnot loss – energy penalty due to the thermal energy conversion into electrical work. The emission loss – any photon that does not produce the electron-hole pair is a loss. The disparity between the angles of emission and absorption causes the Boltzmann loss. The thermalisation loss results from photo-generated charge carriers exiting beyond the band gap down to the band-gap energy. The mismatch between the wide solar spectrum and the comparatively narrow absorption of a single bandgap causes the imperfect absorption loss.

While in a planar geometry solar cell, Carnot, emission, thermalisation and imperfect absorption losses are unavoidable for a cut-off frequency absorption type material, the Boltzmann loss can be minimised even when the cell geometry is planar. According to S-Q

detailed balance $V_{oc,rad}$ is a function of J_{sc} and J_0 and is proportional to the ratio of J_{sc}/J_0. This ratio is proportional to the Boltzmann loss and such a ratio could be optically manipulated to increase the $V_{oc,\,rad}$, and hence the ultimate V_{oc} of the solar cell. As it will be discussed later in this thesis, it is worth noticing that such Boltzmann losses could be reduced in a single junction planar geometry solar cell introducing an appropriate optical configuration to reduce the emission cone. This type of approach to lower e-h recombination, which was overlooked in the original S-Q discussion, is of a fundamental character an may eventually lead to upper limit efficiencies beyond the S-Q limit.

1.3 The review of power conversion efficiencies of established, and emerging solar cells.

At the moment of writing this thesis, the highest PCE of a single junction solar cell has been obtained for a GaAs device with PCE = 27.6%, as seen from the **Figure 1.2**. It corresponds to an 82% of the S-Q efficiency limit and it was possible to achieve provided the high quality of the material and an outstanding quantum yield of 99%. Although GaAs has a close to ideal band gap, solar cells based on such material, it may be difficult to fabricate GaAs solar cells reaching the upper limit efficiency provided constructing the ideal device geometry may be complicated. The silicon based solar cells have an indirect band gap around 1.1 eV and have a significantly higher defect density than GaAs. In addition Si is an indirect gap semiconductor favouring other recombination mechanisms over the radiative one. Current commercial mono-crystalline silicon solar cells reach about 24% conversion efficiency, while the record laboratory cell exhibited an efficiency of 26.8%. The InP semiconductor exhibits a direct band gap of 1.35 eV, which is an optimum band gap, but a high defect density limits the efficiency of InP-based solar cells to 24.2%, which is 25% below the S-Q limit. GAInP solar cells also demonstrated relatively low PCE due to low material quality and non-optimal band gap. Solar cells with thinner active material layers such as CIGS and CdTe have a polycrystalline structure and, although their band gaps are close to optimal, such cells suffer from incomplete light trapping and parasitic absorption, which limits their efficiency. Solution processed CZTSS, DSSC and OPV solar cells, also called third generation photovoltaic cells, provide relatively low efficiencies. All these solar cells suffer from a strong non-radiative recombination in the bulk of the material and at interfaces which limits their V_{oc}, hence the overall efficiency.

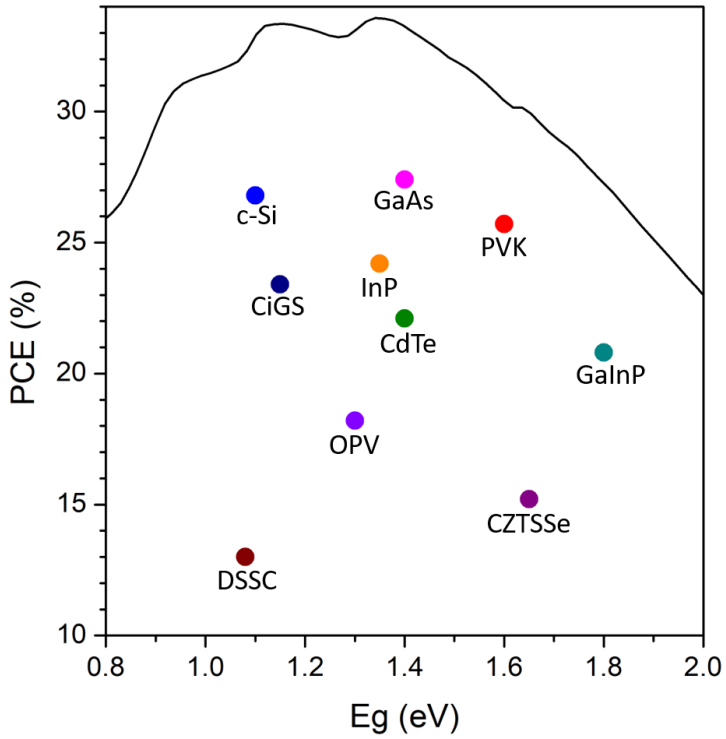

Figure 1.2 Record PCEs of different types of solar cells as a function of band gap of active material and a fundamental efficiency limit.

Another type of solution proceeded solar cells, which stands out from other third generation photovoltaics, are perovskite-based solar cells. Perovskite cells achieved an outstanding performance comparable to crystalline and polycrystalline devices with a record PCE reaching 25.7%. In addition, the PLQY of perovskite based cells have been reported to be above 40%, which is an outstanding value for a third generation material. Unlike GaAs solar cells, the perovskite solar cells can have various structural configurations. The perovskite-based solar cells consist of several thin layers of materials: transparent conductive oxide (TCO), electron-transporting layer (ETL), active layer of perovskite (PVK), hole-transporting layer (HTL) and a back electrode acting as a mirror. This provides room for different strategies for improving the performance of the devices. It has been shown that the PLQY of perovskites can be enhanced by chemical engineering, passivation of active material and a careful selection of the charge transporting layers. Optical strategies for improving the performance of the perovskite solar cells have also been developed, mostly targeting a J_{sc} enhancement, which is a straightforward way of increasing a PCE of the device. A more efficient light absorption in

perovskite films can be achieved by light trapping approaches, antireflection coatings, implementation of scattering layers, nanoparticles, structured substrates, etc. However, the optical effect on the open-circuit voltage has been studied to a lesser extent. As demonstrated in **Eq. (1.10)**, and discussed above, the $V_{oc,rad}$ is a function of J_{sc} and J_0 and is proportional to the logarithm of J_{sc}/J_0 ratio. This ratio can be manipulated by changing the escape cone of the emitted photons by the active materials using wavelength and angle selective photonic structures, which can be designed to trap the emitted photons. As perovskites have demonstrated low defect densities, slow Auger recombination rate, high absorption coefficient, long carrier diffusion length, and high PLQY the trapping of emitted photons may effectively reduce the J_0, contribute to J_{sc} and simultaneously increase the J_{sc}/J_0 ratio, reducing the Boltzmann loss.

1.4 Perovskite materials for photovoltaic application

Perovskite is one of the most abundant crystalline structural families. In this thesis we focus on an organic–inorganic hybrid perovskite material, with the general crystal structure of ABX_3, in which A is the larger cation, confined within a cage determined by the octahedral coordination of a smaller cation B, with X is the anion.

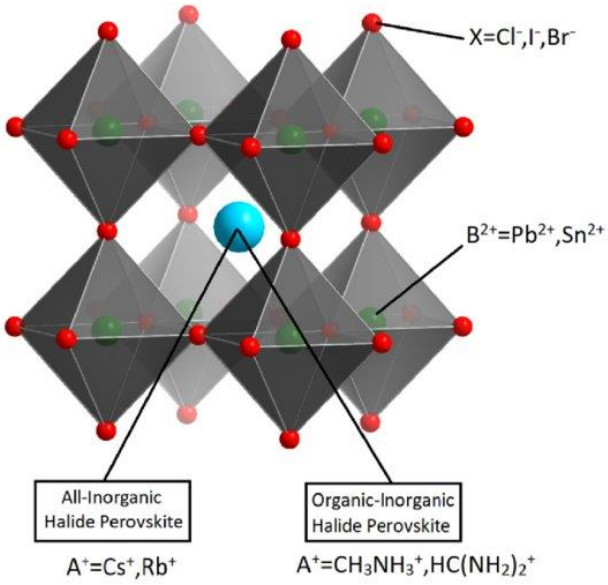

Figure 1.3 Schematic diagram of ABX_3 lead halide perovskite crystal structure. Figure reprinted from Dai et. al.

The family of perovskites can be constructed with many possible combinations of elements or molecules that may be incorporated in each one of the three components that constitute the overall structure. First time implemented as an active material of a solar cell in 2009 by Tsutomu Miyasaka et al., perovskites have emerged among other third-generation photovoltaics such as CZTS, DSSC, OPV and QDSC based on other types of materials. For solar cell applications, the most widely used composition is the organic-inorganic lead halide perovskite. However, the composition can be changed which allows the fabrication of all-inorganic or lead-free perovskites. The fabrication of perovskite materials can be carried out with earth-abundant materials and low-cost methods, which makes them very attractive for a large-scale solar energy to electricity conversion Most of the layers of such solar cells can be deposited by solution processes and scaled up for industrial manufacturing. The major challenges of perovskite materials are their stability and use of toxic materials, which need to be overcome for it to be commercialised on a wide scale, but this topic is out of scope in this thesis.

Perovskites semiconductor materials are characterised by a high absorption coefficient, a long charge carrier diffusion length and lifetime, and a high carrier mobility. Another important parameter of perovskites is a relatively high PLQY in contrast to other third generation materials. Internal PLQYs provide the information about the fraction of radiative recombination relative to other recombination pathways in the material and sets the fundamental limitation on the PCE of solar cells achieved with such material. For example, the GaAs solar cells have reached the highest efficiency so far, having a PLQY of more than 99%, while Si-based solar cells, which have also been widely studied, could not reach such a high PCE due to the limited PLQYs of around 20%.

The internal PLQYs of the perovskite films have been reported to exceed 95% as demonstrated by Sam Stranks et. al., which is approaching the values obtained for GaAs. Another work by Ian L. Braly et.al. demonstrated the PLQYs of the perovskite films to be around 92%. Paul Fassl et. al. applied an accurate quantification of photon recycling approach and reported internal PLQYs of perovskite films as high as 78%. External PLQYs, which not only depend on the radiative and non-radiative recombination rates but also on the geometry and configuration of the material, were shown to exceed 66% as reported by Mojtaba Abdi-Jalebi et. al. It was demonstrated by Richter et. al. that by changing the geometry of the perovskite film, from planar to textured, the external PLQY was enhanced from 15% to 57%, which corresponded to 70% internal PLQY. To further enhance the PLQYs of perovskite

films, different fabrication methods and passivation approaches have been developed. Perovskites are sensitive to the environment and it was demonstrated by Giles E. Eperon et. al. that the presence of moisture during the crystallisation process improves the PLQY from 1% to 13%. Nobuya Sakai et. al reported that the toluene-assisted crystallisation method increases the external PLQY from 3% to 11.5%. The low-pressure vapor-assisted solution process fabrication method developed by Carolin M. Sutter-Fella improved PLQY by an absolute 10%. The metal ion doping method reported by Jacob Tse-Wei Wang effectively improved the quality of the perovskite, hence enhanced the external PLQY from 6% to 16%. Nakita K. Noel et. al. reported the Lewis base passivation approach, which allowed to enhance the external PLQY of an already high quality film from 15% to 24%. The passivation method using electron-donating molecules such as n-trioctylphosphine oxide has demonstrated an outstanding external PLQY of 35%, as reported by Dane W. deQuilettes et. al.

Provided relatively high PLQY, perovskites have been shown to be an attractive material, not only for solar cell applications but also for LED, laser and even detector applications. All these applications require the material to have a low non-radiative recombination rate, which can also be achieved by the fabrication of perovskite single crystals. Yingqi Wang et. al. demonstrated that a one-dimensional perovskite single crystal can have an external PLQY as high as 90% if put under pressure to suppress non-radiative losses. Yeasin Khan et al. fabricated a millimetre-sized perovskite single crystal with external PLQY of up to 70% by replacing halides with formate anions and changing the perovskite structure.

To maintain the high external PLQYs in the solar cell, the solar cell configuration and buffer layers must be carefully selected. Note that perovskite based solar cells consist of several layers of materials. Moreover, they can have a n-i-p or p-i-n structure, planar or mesoporous configurations, as depicted in **Figure 1.4.**

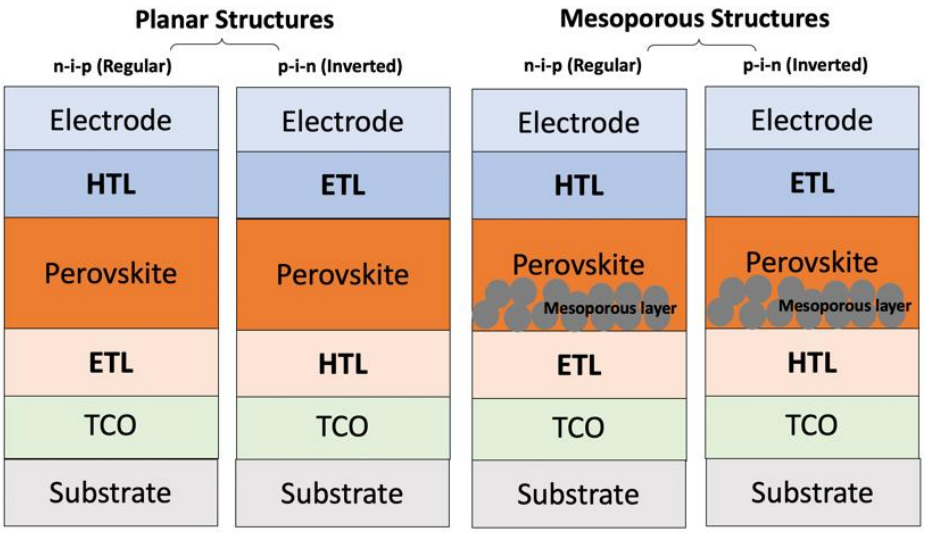

Figure 1.4. Four device configurations of perovskite solar cells: planar and mesoscopic structures. Figure reprinted from S. B. Dkhil.

As mentioned above, the external PLQY of a perovskite film is affected by its geometry and when embedded into the solar cell a quenching of PLQYs is observed. When writing the current thesis, the external PLQY of perovskite-based solar cells had been demonstrated to be as high as 5%, as reported by Sergiu Draguta et. al and Zhifa Liu et. al. The quenching of the PLQY is attributed to the introduction of non-radiative recombination sites at the interfaces of the active material with other layers in the cell and parasitic absorption. Even though an external PLQY of 5% is rather a low, an outstanding V_{oc} of 1.26 eV has been achieved for such solar cells fabricated by Zhifa Liu et. al. Such a solar cell exhibited one of the smallest V_{oc} losses relative to its radiative V_{oc} suggesting that the quality of the active layer and the internal PLQY are reasonably high for such a device. Indicating that, even though the external PLQY of the perovskite-based solar cells is relatively low, the internal PLQY is high enough to consider perovskites as a good candidate for studying fundamental loss mechanisms and approaches to overcome them.

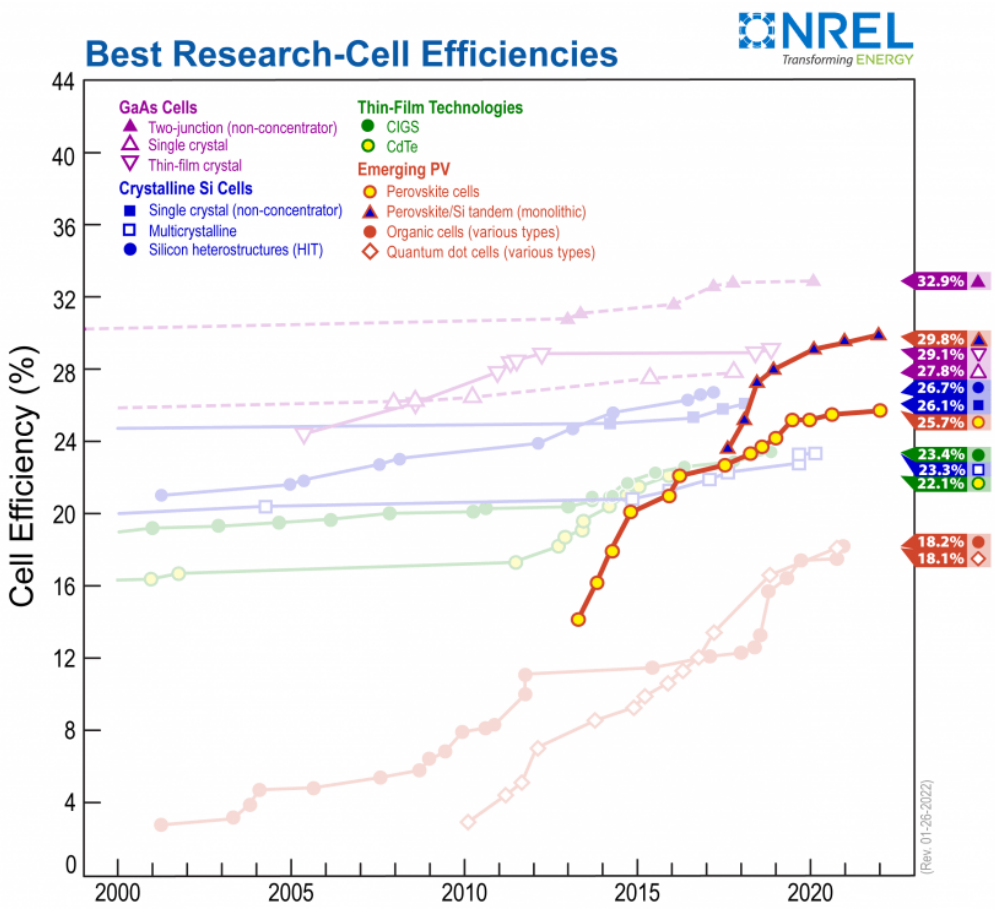

Figure 1.5 Solar cell efficiency chart by NREL-National Renewable Energy Lab, where perovskite based solar cells are highlighted.

Since comprehensive research on perovskite materials for solar cell applications began efficiency of perovskite-based devices has rocketed from an original 3.8% in 2009 to 25.7% in 2021. This rapid PCE increase was achieved by material optimisation to grow smooth polycrystalline perovskite films, strategies for defect passivation and compositional engineering to achieve favourable band gaps, and by addressing stability issues of the material. After, the interface engineering became the key strategy and facilitated reaching PCE above 25% and high PLQYs. Since 2020 the trend of efficiency increase has slowed down, meaning that new strategies should be applied. At the moment of writing this thesis, the highest PCE of a single junction perovskite is 25.7% which lags below the predicted efficiency limit, meaning there is room for improvement for such devices. The strategy of optical optimisation may turn the tide and help to surpass the efficiency plateau which appears to be reached now.

1.5 Thesis objectives and outline

This thesis focuses on studying the relation between the V_{oc} of the perovskite solar cells and the propagation, absorption and emission of photons within such devices and provides some routes for such V_{oc} enhancement. The strategy of optical enhancement of V_{oc} has been rarely studied, and was experimentally demonstrated by Steiner et. al. only for GaAs solar cells. As it was mentioned in section 1.2, the V_{oc} of the solar cells depends on PLQY and is limited by non-radiative recombination and fundamental losses, such as the Boltzmann loss. Achieving high V_{oc} requires maximising the PLQY and handling the incoming and emitted photons, limiting the escape cone of the latter ones. To ensure that perovskites are suitable in this endeavour, a comprehensive study of the material and routes to enhancing the PLQYs must be conducted. This also requires demonstrating that the V_{oc} and PLQY of perovskite solar cells follow the relation predicted by S-Q.

Chapter 2 of this thesis focuses on determining whether perovskite solar cells follow the behaviour predicted by S-Q theory. Experimental measurements are backed by electromagnetic simulations based on a full-wavevector detailed balance and a fluorescence power-loss model that describes the behaviour of perovskite solar cells in terms of the PLQY. The model proposed increases the accuracy relative to already existing models, as it takes into account realistic optical parameters of the material used in the cell, includes computations for normal and oblique incidence of the light, and determines the actual absorption by the perovskite active layer in the presence of light interference. The relation between PLQY and V_{oc} of the perovskite solar cells is established, with some deviations which are explained. The next step was to fabricate a perovskite material with enhanced PLQY, hence reduced non-radiative recombination.

To obtain such material, the two-step compact PbI_2 – template fabrication method was developed and is described in Chapter 3. Perovskites normally form polycrystalline films, constituting grains, also called crystals of the material. The open-circuit voltage of a solar cell is directly related to the quality of the active material. Hence, to achieve decent V_{oc}s, material defects must be reduced to a minimum. Depending on the fabrication method, the grain size can vary from tens of nanometres to micrometres, the density of defects and the quality of grain boundaries, which will affect the performance of the device, can also be controlled. Our fabrication method provides a better crystal control and minimises interface nonradiative recombination in perovskite films, meaning that the PLQY was enhanced and such perovskites are eligible for our purpose and further studies to relate the V_{oc} and PLQY can be conducted.

Chapter 4 is devoted to discuss the approach we implemented to optically increase the V_{oc} of perovskite solar cells. For this purpose, the theoretical model is modified to include an optical multilayer structure on top of the glass substrate on the opposite side of the solar cells. An inverse integration based on a genetic optimisation algorithm is incorporated in our model to obtain the optimal optical structure to increase the V_{oc} and the overall performance of the cell. Such angle- and wavelength-restricting photonic structure does not require a sophisticated fabrication process and can be achieved with a dielectric multilayer (DM). A dielectric multilayer can target two loss mechanisms at a time, extrinsic loss due to reflections at the air/substrate interface and the Boltzmann loss. The next step was to establish the experimental route for confirmation of this phenomena. This required the fabrication of the computed photonic structures and implementation of such structures onto the solar cell, which is demonstrated and discussed in Chapter 5. The enchantment of the V_{oc} has been demonstrated, however, it cannot be attributed only to Boltzmann loss reduction and requires further investigation.

Chapter 2

Relationship between V_{oc} and PLQY in perovskite-based solar cells

2.1 Introduction

The relationship between the actual V_{oc} of a given perovskite solar cell and the PLQY may not be as simple as can be inferred from the oversimplified solar cell diode-based models discussed in the introduction chapter of the current thesis. In this chapter we consider what the side effect of reducing non-radiative recombination may be on the final cell V_{oc}. We consider a route to increase the PLQY of a $FA_{0.8}MA_{0.2}PbI_{3-y}Br_y$ perovskite and explain why such an increase in PLQY is not reflected in the experimentally measured V_{oc}s for the fabricated cells. Alternative approaches based on other perovskite cells fabricated by other research groups are also analysed in view of the computational model we describe in section 2.2. A model that modifies the S-Q approach by taking into account the layered structure of perovskite cells and the parasitic absorption from all such cell layers. In other words, in this chapter we investigate how the V_{oc} of actual devices differs from theoretical predictions, which mechanisms limit the V_{oc} and establish the first reported V_{oc}(PLQY) relation for perovskite solar cells.

2.2 Full-wave generalised detailed balance model for the $V_{oc,rad}$ calculation

Prior to designing perovskite solar cells with enhanced PLQY and V_{oc}, fundamental research combining experiments and realistic simulations is needed to determine and understand the relation between V_{oc} and PLQY for such type of cells. First, we consider a model that fully describes photon absorption and emission in the cell multilayer structure shown in depicted in **Figure 2.1**.

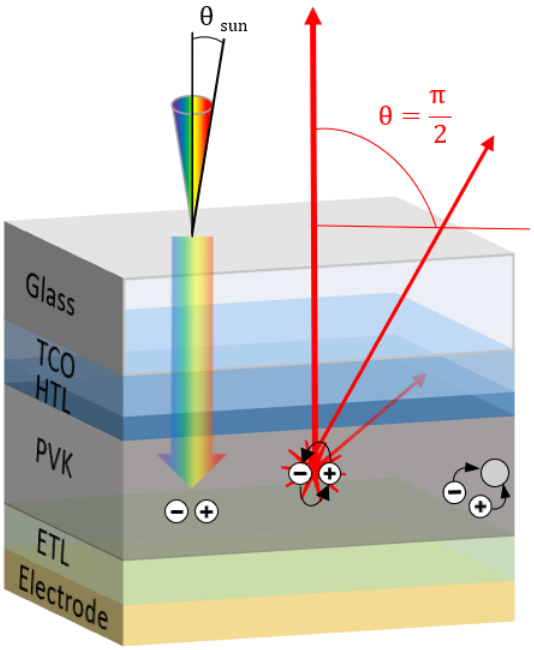

Figure 2.1. Schematic configuration of the perovskite solar cell, including optoelectronic mechanisms at open-circuit conditions: generation of electron-hole pair, radiative recombination of e-h pair, escape of emitted photon, parasitic absorption, and non-radiative recombination.

By following the S-Q detailed balance model, the expression for $V_{oc\ rad}$ can be rewritten as:

$$V_{oc,rad} = \frac{kT}{q} \ln\left(\frac{\int_0^{\theta_{sun}} \int_0^{\infty} A(E,\theta) S(E) \sin\theta\cos\theta d\theta dE}{\int_0^{\frac{\pi}{2}} \int_0^{\infty} A(E,\theta) B(E) \sin\theta\cos\theta d\theta dE}\right) \quad (2.1)$$

The numerator stands for the sunlight absorbed by the perovskite layer, and the denominator stands for the fluorescence of this layer escaping from the cell, as shown in **Figure 2.1**. S(E) is the solar spectrum, B(E) is the blackbody radiation spectrum of the cell, and A(E,θ) is the energy and angle-dependent absorbance of the perovskite layer. A(E,θ) is calculated using the coherent transfer matrix formalism. To compute A(E,θ) for the perovskite cells considered in this chapter, a realistic layered structure was used with the energy-dependent dielectric functions of the layers constituting the cell being determined experimentally. Our simulation method is based on the exact calculation of A(E,θ). This contrasts with most other methods reported in the literature, which neglect coherent effects in the computation of absorbance or assume that absorbance is angle-independent and/or presents a step-function energy profile.

Such simplifications are not correct for perovskite solar cells due to the wavelength-scale thickness of the different layers. In perovskite solar cells, optical interference and cavity modes make the absorbance depart from the incoherent optics (Beer-Lambert) prediction and exhibit an angular dependent and a non-step-function energy absorption profile. For an accurate determination of $V_{oc,rad}$, these features must be taken into account by calculating exactly $A(E,\theta)$, as done in this thesis. At a given photon energy/wavelength, the absorbance of the perovskite layer of the solar cell is defined by:

$$A_{pvk} = \frac{1}{S_0^{S(P)}} \int Q_{z,pvk}^{S(P)}(z)dz \tag{2.2}$$

where, $S_0^{S(P)}$ is the sun irradiance with S(P) polarisation and $Q_{z,pvk}^{S(P)}(z)$ is the optical power dissipated at depth z in the perovskite layer for each polarisation of the light. For S and P polarisation, the dissipated optical power is expressed by:

$$Q_{z,pvk}^{S}(z) = \frac{1}{2} c\varepsilon_0 p_{pvk} \alpha_{pvk,\theta} \left|E_{y,pvk}(z)\right|^2 \tag{2.3a}$$

$$Q_{z,pvk}^{P}(z) = \frac{1}{2} c\varepsilon_0 p_{pvk} \alpha_{pvk,\theta} \left(\left|E_{x,pvk}(z)\right|^2 + \left|E_{z,pvk}(z)\right|^2\right) \tag{2.3b}$$

where $p_{pvk} = \frac{1}{k_0} \mathrm{Re}\{k_{z,pvk}\}$, $\alpha_{pvk,\theta} = 2\mathrm{Im}\{k_{z,pvk}\}$, while $E_{y,pvk}(z)$, $E_{x,pvk}(z)$ and $E_{z,pvk}(z)$ are the components of the electric field at a depth z inside the perovskite layer.

The distribution of the electric field in the cell can be derived from Fresnel equations. Our solar cell consists of a thick glass substrate and a stack of thin layers, so in our model we are taking into account incoherent calculations for the thick glass substrate and coherent calculations for the stack of thin layers.

In the coherent calculations (stack of thin layers), the electric field in layer j, at the interface with layer k, is calculated as a function of the field in layer n+1 at the interface with layer n following:

$$\begin{bmatrix} E_j^+ \\ E_j^- \end{bmatrix} = I_{j,k} L_k I_{k,k+1} \dots L_n I_{n,n+1} \begin{bmatrix} E_{n+1}^+ \\ E_{n+1}^- \end{bmatrix} = M \begin{bmatrix} E_{n+1}^+ \\ E_{n+1}^- \end{bmatrix} \tag{2.4}$$

where E^+_j, E^-_j and E^+_{n+1} are incident, reflected and transmitted waves.

The interface matrix $I_{j,k}$ relates the fields on both sides of the interface between the layers j and k:

$$\begin{bmatrix} E_j^+ \\ E_j^- \end{bmatrix} = I_{j,k} \begin{bmatrix} E_k^+ \\ E_k^- \end{bmatrix} = \frac{1}{t_{j,k}} \begin{bmatrix} 1 & r_{j,k} \\ r_{j,k} & 1 \end{bmatrix} \begin{bmatrix} E_k^+ \\ E_k^- \end{bmatrix} . \quad (2.5)$$

Fresnel coefficients $r_{j,k}$ and $t_{j,k}$ can be obtained for normal and oblique incidence for different polarisations and at the chosen photon energy/wavelength.

For s-polarisation:

$$r_{j,k}^S = \frac{\eta_j \cos\theta_j - \eta_k \cos\theta_k}{\eta_j \cos\theta_j + \eta_k \cos\theta_k} \quad (2.6a)$$

$$t_{j,k}^S = \frac{2\eta_j \cos\theta_j}{\eta_j \cos\theta_j + \eta_k \cos\theta_k} \quad (2.6b)$$

For p-polarisation:

$$r_{j,k}^P = \frac{\eta_j \cos\theta_k - \eta_k \cos\theta_j}{\eta_j \cos\theta_k + \eta_k \cos\theta_j} \quad (2.7a)$$

$$t_{12}^P = \frac{2\eta_j \cos\theta_j}{\eta_j \cos\theta_k + \eta_k \cos\theta_j} \quad (2.7b)$$

where η is the complex photon energy/wavelength-dependent refractive index of the layer.

The matrix L_j describes propagation across layer j:

$$\begin{bmatrix} E_j^+ \\ E_j^- \end{bmatrix} = L_j \begin{bmatrix} E_k^+ \\ E_k^- \end{bmatrix} = \begin{bmatrix} e^{-ik_{z,j}d_j} & 0 \\ 0 & e^{ik_{zj}d_j} \end{bmatrix} \begin{bmatrix} E_k^+ \\ E_k^- \end{bmatrix} \quad (2.8)$$

where $k_{z,j}$ is the projected wavevector and d_j is the layer thickness.

The components of the electric field at a depth z inside the perovskite layer can be derived from:

$$E_{y,pvk}(z) = \left[t_{pvk}^+ e^{ik_{z,pvk}z} + t_{pvk}^- e^{-ik_{z,pvk}z}\right] \quad (2.9a)$$

$$E_{x,pvk}(z) = \frac{k_{z,pvk}}{\eta_{pvk} k_0}\left[t_{pvk}^+ e^{ik_{z,pvk}z} + t_{pvk}^- e^{-ik_{z,pvk}z}\right] \quad (2.9b)$$

$$E_{z,pvk}(z) = \frac{k_{x,0}}{\eta_{pvk} k_0}\left[t_{pvk}^+ e^{ik_{z,pvk}z} + t_{pvk}^- e^{-ik_{z,pvk}z}\right] \quad (2.9c)$$

where k_0 is the wavenumber, t^-_{pvk} and t^+_{pvk} are the so-called internal transfer coefficients of the perovskite layer, which can be calculated by using the transfer matrices described above.

The incoherent calculations are used to determine the value of the incoming electric field onto the stack of thin layers. With the reflectance and transmittance of the air-glass interface being R_{01} and T_{01} and those of the stack being R_{stack} and T_{stack}, the total reflectance of the whole structure is:

$$R_{tot} = \frac{R_{01}+R_{stack}-2R_{01}R_{stack}}{1-R_{01}\,R_{stack}}. \quad (2.10)$$

Thus, in order to take into account the effect of the thick glass substrate, the incoming electric field onto the stack of thin layers is normalised by $(1\text{-}R_{01})/n_{glass}(1\text{-}R_{01}R_{stack})$. Optical constants of materials used for simulations, the absorption coefficient of the perovskite and the consistency check of the model are shown in Appendix A.1.1-3. Moreover, the colour plots of the calculated absorbance of the perovskite layer and other layers constituting the cell are shown in Appendix A.1.4.

2.3 Solar cell structure and optical properties

A series of solar cells based on a $FA_{0.8}MA_{0.2}PbI_{3-y}Br_y$ perovskite were produced with the two-step method. The fabrication recipe is described in Appendix A.2. The cells present a n-i-p configuration with the structure depicted in **Figure 2.2** (a): Glass/ITO/SnO_2/PVK/Spiro-OMeTAD/Au. In this structure, a 100 nm ITO layer grown on a glass substrate acts as front electrode, a 20 nm SnO_2 layer as electron transporting layer, a 550 nm thick perovskite acts as active layer, a 140 nm Spiro-OMeTAD layer acts as hole transport layer, and a 80 nm Au layer acts as reflecting back electrode. As exemplified in **Figure 2.2** (b), the fabricated perovskite presents a bandgap absorption edge near 1.54 eV (805 nm), and the cells exhibit a clear fluorescence (PL) signal peaking at this edge. Note that all the cells in this chapter of the thesis were fabricated to present similar optical and photovoltaic properties. In particular, the layer thicknesses in all the fabricated cells are similar to those in the cells shown in **Figure 2.2** (a). However, due to the limited reproducibility that impacts in particular the electronic properties of the perovskite layer, as discussed later in section 2.4, the different cells present different PLQYs and V_{oc}s.

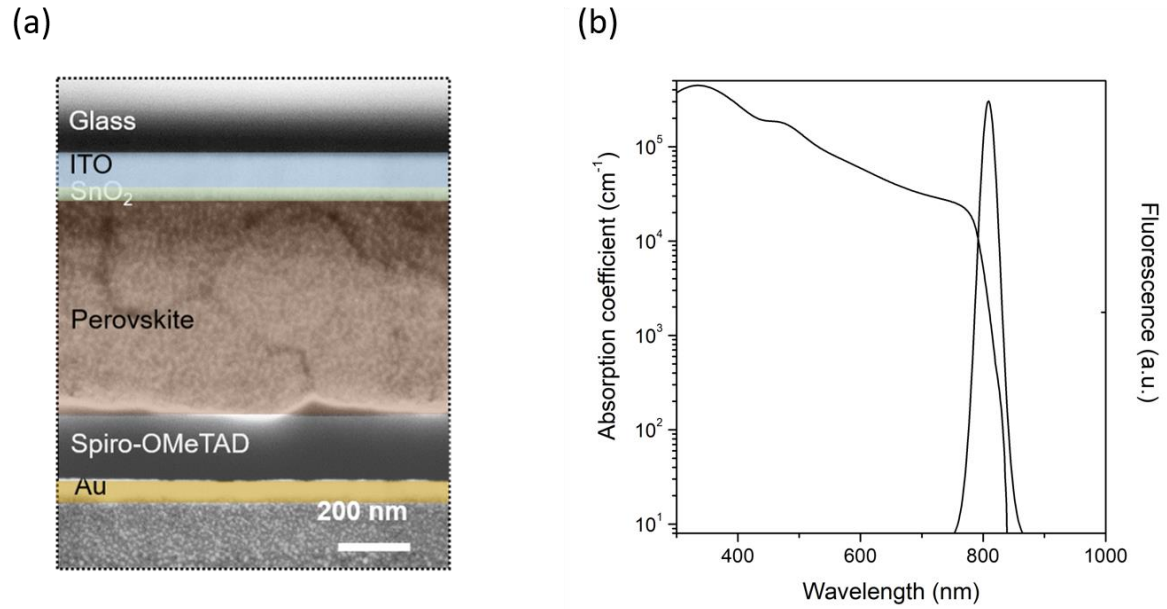

Figure 2.2. (a) Typical structure of the fabricated cells (scanning electron microscope image). (b) Spectrum of the absorption coefficient of the $FA_{0.8}MA_{0.2}PbI_{3-y}Br_y$ perovskite and a typical fluorescence spectrum of the cells.

2.4 Measured PLQY and V_{oc}

The PLQY of the solar cells was measured with a home-built integrating sphere - based setup with the configuration shown in **Figure 2.3** (a). A 532 nm laser beam with a 1 sun-equivalent intensity was used to excite the perovskite fluorescence. The reflected/scattered laser intensity and fluorescence intensity were collected separately to determine PLQY. The V_{oc} of the cells was measured with a solar simulator. For comparison, V_{oc} was also measured under laser illumination (532 nm, 1-sun equivalent) on selected cells. Similar V_{oc} values were obtained with both approaches. Further details about the measurement methods are given in Appendix A.3.1.

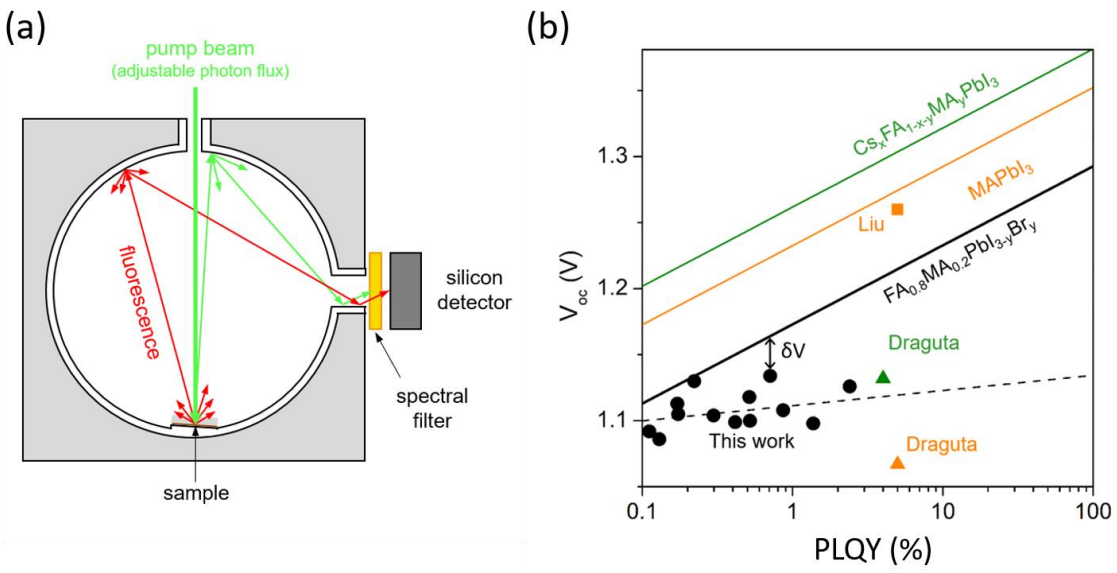

Figure 2.3. (a) Schematic representation of the external fluorescence quantum yield measurement setup. A green pump laser beam (wavelength of 532 nm) is shined onto the sample placed inside an integrating sphere. (b) Measured V_{oc} and PLQY of our $FA_{0.8}MA_{0.2}PbI_{3-y}Br_y$ solar cells (black dots), of $Cs_xFA_yMA_{1-x-y}PbI_3$ (green triangle) and $MAPbI_3$ (orange triangle) cells from **Ref. 25** (Draguta et. al.), and of the $MAPbI_3$ cell from **Ref. 26** (Liu et. al.) - orange square. The black dashed line is a guide for the eye to show the experimental V_{oc} = f(PLQY) relation for our cells. The solid lines represent the simulated ideal diode V_{oc} = f(PLQY) according to **Eq. (1.9)** with $V_{oc,rad}$ obtained from **Eq. (2.1)** for each type of cell: our $FA_{0.8}MA_{0.2}PbI_{3-y}Br_y$ solar cells (black line), $Cs_xFA_yMA_{1-x-y}PbI_3$ solar cell from **Ref. 25** (green line), $MAPbI_3$ solar cells from **Ref. 26** (orange line). As an example, the voltage loss δV is shown for one of our $FA_{0.8}MA_{0.2}PbI_{3-y}Br_y$ cells.

Figure 2.3 (b) depicts the PLQYs and V_{oc}s measured for our series of solar cells providing values ranging from 0.1 to 3% and from 1 to 1.13 V, respectively. All the solar cells used in this work were fabricated by the same method and have the same structure. As mentioned in section 2.1, different values of PLQY and V_{oc} from cell to cell are not caused by deliberately different fabrication parameters but by a limited reproducibility impacting in particular the electronic properties of the perovskite layer. Despite reaching rather high values compared with the literature, the measured V_{oc}s lag significantly below the $V_{oc,rad}$ of 1.28 V obtained from **Eq. (2.1)** using the structure and layer thicknesses taken from **Figure 2.2** (a). This can be attributed in part to the low PLQY of the cells. Another cause to the non-optimal V_{oc} of the cells is the deviation from the ideal diode behaviour: the measured V_{oc}s depart from the ideal diode V_{oc} =

f(PLQY) calculated from **Eq. (1.9)** with $V_{oc,rad}$ of 1.28 V and the measured PLQY. This deviation, materialised by a voltage loss $\delta V = V_{oc,ideal\ diode} - V_{oc,measured}$, increases with the PLQY. This suggests that, in the cells, the microscopic mechanism that leads to an improved PLQY also introduces non-idealities that limit the V_{oc} increase and thus do not allow it to approach $V_{oc,rad}$. For the sake of completeness, also presented in **Figure 2.3** (b), are the data from two recent works that reported V_{oc} and PLQY measurements on finished perovskite solar cells and the calculated ideal diode V_{oc} = f(PLQY) relations for those cells, which have been obtained from **Eq. (2.1)** with the cell structures and layer thicknesses taken from the corresponding references. The thereby calculated relations yield higher V_{oc}s than those calculated for our cells. This is mainly because the perovskites considered in such works ($MAPbI_3$ and $Cs_xFA_yMA_{1-x-y}PbI_3$) present a larger bandgap, thus implying a higher $V_{oc,rad}$. Note, that in the cells from **Ref. 25** the $MAPbI_3$ layer was very thin (280 nm), which contributes to further enhancing $V_{oc,rad}$. Comparing experimental and numerically computed data, it is seen that the $MAPbI_3$ and $Cs_xFA_{1-x-y}MA_{1y}PbI_3$ cells from **Ref. 26** present PLQYs as high as those of our most fluorescent cells, and a similar or higher δV. In contrast, the $MAPbI_3$ cell from **Ref. 25** shows a PLQY of 5% and a negligible δV. Consequently, it presents the highest V_{oc} reported in the literature for a $MAPbI_3$ cell (V_{oc} = 1.26 V).

2.5. Origin of the low PLQY

2.5.1 Non-radiative recombination

To determine the cause of the low PLQY of the solar cells, the contribution of non-radiative recombination was first studied. With such an aim, their PLQYs, shown in **Figure 2.4,** were measured as a function of the incident light intensity I_{exc}, from 1 to 120 suns. The sample was illuminated with an expanded and collimated monochromatic continuous laser beam to illuminate completely the solar sells surface as in the solar simulator. More details are provided in Appendix A.3.2.

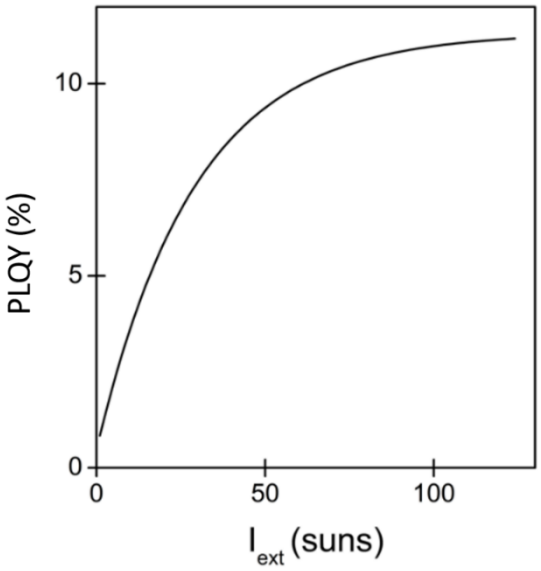

Figure 2.4. Experimentally measured PLQY as a function of excitation intensity for a selected solar cell. The solar cell was illuminated with 532 nm monochromatic continuous wave laser excitation. The curve represents the fit of the experimental data point.

Figure 2.5 shows the PLQY of the solar cells measured for different I_{exc}, plotted as a function of the corresponding PLQY measured under I_{exc} = 1 sun. Upon increasing I_{exc}, the PLQY of a given cell increases strongly, exhibiting a saturation behaviour. This shows that the low PLQY of the cells at 1 sun is in an important part due to non-radiative recombination at long-lived traps. Upon increasing I_{exc}, the traps are filled thus removing non-radiative recombination paths and improving PLQY. Note that the PLQY increase with I_{exc} is more pronounced for the cells with the lowest PLQY at 1 sun, indicating that they present the highest density of long-lived traps. Note also that, at the maximum I_{exc} used in our measurements, the PLQY of the different cells does not reach the same value. The cells with the smallest PLQY at 1 sun still present a smaller PLQY than those with the highest PLQY at 1 sun. The first possible cause for this different PLQY's at high I_{exc} is that the long-lived traps in the cells with the lowest PLQY are not fully saturated even at the highest I_{exc} considered here. Another possible origin to the observed trend could be the existence of short-lived traps, which cannot be saturated upon increasing I_{exc}, and whose density would scale with that of the long-lived traps.

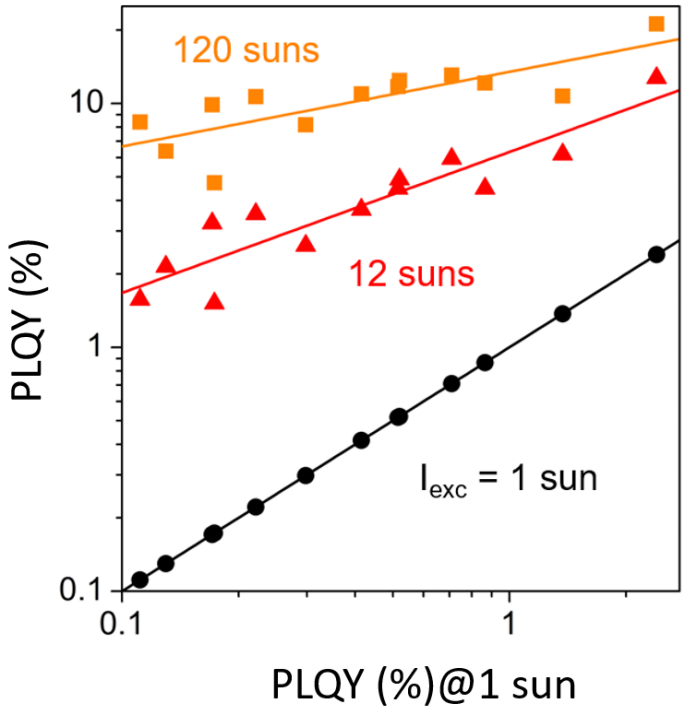

Figure 2.5. Excitation intensity-dependent PLQY of our perovskite solar cells. PLQY of our $FA_{0.8}MA_{0.2}PbI_{3-y}Br_y$ solar cells measured for different incident light intensities I_{exc} plotted as a function of the corresponding PLQY measured under I_{exc} = 1 sun. The full lines have been obtained by fitting the measured data (symbols).

These effects may also partly explain why the maximum PLQY reached in **Figure 2.5** for the I_{exc} = 120 suns is only 20%. Another possible cause of the much below 100% is parasitic absorption. Even if non-radiative recombination in the perovskite layer were to be suppressed, absorption of the re-emitted photons in the non-active layers yields a non-optimal PLQY. The next section is focused on quantifying the effect of parasitic absorption as a limiting factor of the PLQY.

2.5.2 Parasitic absorption

Quantifying the contribution of parasitic absorption to the PLQY of a solar cell requires determining the fluorescence power losses in the layers constituting the cell. To estimate how drastically parasitic absorption limits the PLQY of the considered cell structure, a model that calculates the fluorescence power dissipated in each layer (TCO, HTL, perovskite, ETL and

electrode) and escaping the cell was developed. Its main assumption is that fluorescence power is homogeneously distributed within the cell. The fluorescence is based on emission by randomly oriented dipoles, thus resulting in an isotropic internal emission process. Moreover, an important fraction of the internally emitted photons falls outside the escape cone and is trapped in the cell by total internal reflection. These trapped photons are re-absorbed and eventually re-emitted, with a loss of memory of their initial wavevector. This provides an extra randomisation mechanism of the fluorescence, which can develop in planar structures. In a cell, part of the incident optical power is absorbed by the perovskite and re-emitted internally via fluorescence with the quantum efficiency η_{int}. The internally and directly re-emitted power is P_{em}. This contributes to generating a pool of fluorescence photons, with an equilibrium power P_{int} which is assumed to be homogenised inside the cell. To reach such equilibrium, other mechanisms are involved: escape of fluorescence photons from the cell (P_{esc}), loss of fluorescence photons by absorption in the mirror or non-active layers of the cell (P_{par}), re-absorption of fluorescence photons by the perovskite layer (P_{reabs}), re-emission of part of these re-absorbed photons with the quantum efficiency η_{int} (or recycled, P_{recyc}). At steady state:

$$P_{em} - P_{esc} - P_{par} - P_{reabs} + P_{recyc} = 0 \tag{2.11}$$

Hereafter we explicit the different terms. The calculation is based on the same assumptions Kim. et. al.

Internally and directly re-emitted power P_{em}:

$$P_{em} = \eta_{int} < E > \int \frac{A(E)S(E)}{E} dE \tag{2.12}$$

Where A(E) is the absorbance spectrum of the perovskite layer, S(E) is the solar spectrum at room temperature, E is photon energy, <E> is the average photon energy of emission.

Power escaping the cell P_{esc}:

$$P_{esc} = \int P_{int}(E) X_{esc}(E) dE \tag{2.13}$$

where:

$$X_{esc}(E) = \int_0^{\pi/2} (1 - R(E,\theta)_{glass/air}) \sin\theta\cos\theta d\theta \quad (2.14)$$

In this equation, $R(E,\theta)_{glass/air} = 0.5 \left| r_s(E,\theta)_{glass/air} \right|^2 + 0.5 \left| r_p(E,\theta)_{glass/air} \right|^2$ is the polarisation-averaged reflectance of glass/air interface, $r_{s,p}(E, \theta)_{glass/air}$ being the corresponding Fresnel reflectance coefficient.

Power lost by parasitic absorption P_{par}, part is lost in the back metal electrode (mirror), and part is lost in the other non-active layers so that:

$$P_{par} = P_{mirror} + \Sigma_j P_{par,j} \quad (2.15)$$

with:

$$P_{mirror} = \int P_{int}(E) X_{mirror}(E) dE \quad (2.16)$$

where:

$$X_{mirror}(E) = \int_0^{\pi/2} (1 - R(E,\theta)_{spiro/Au}) \sin\theta\cos\theta d\theta \quad (2.17)$$

In this equation, $R(E,\theta)_{spiro/Au} = 0.5 \left| r_s(E,\theta)_{spiro/Au} \right|^2 + 0.5 \left| r_p(E,\theta)_{spiro/Au} \right|^2$ is the polarisation-averaged reflectance of the spiro-OMeTAD/back metal electrode interface, $r_{s,p}(E,\theta)_{spiro/Au}$ is the corresponding Fresnel reflectance coefficient. To calculate this reflectance, we assumed a semi-infinite medium. This seems acceptable, since the 80 nm Au layer in the considered cells transmits only 1% of light in the spectral region of the perovskite fluorescence.

$$P_{par,j} = \int P_{int}(E) X_{par,j}(E) dE \quad (2.18)$$

where:

$X_{par.j}(E) = 2\,\alpha_j(E)\,d_j$

$\alpha_j(E)$ being the absorption coefficient of layer j and d_j its thickness.

Power lost by re-absorption in the perovskite layer P_{reabs}:

$$P_{reabs} = \int P_{int}(E) X_{reabs}(E) dE \quad (2.19)$$

where:

$X_{reabs}(E) = 2\,\alpha(E)\,d$

$\alpha(E)$ is the absorption coefficient of the perovskite layer and d its thickness.

Power gained by re-emission of the re-absorbed photons by the perovskite layer P_{recyc}:

$$P_{recyc} = < E > \int \frac{X_{recyc}(E) P_{int}(E)}{E} dE \quad (2.20)$$

Where $X_{recyc}(E) = \eta_{int} X_{reabs}(E)$ (2.21)

After rearranging the equations, PLQY is given by:

$$PLQY = \frac{\eta_{int} < E > \int_0^{\infty} \frac{X_{esc}(E)}{X(E)} \alpha(E) B(E) dE}{\int_0^{\infty} (E - \frac{\eta_{int} < E > X_{reabs}(E)}{X(E)}) \alpha(E) B(E) dE} \quad (2.22)$$

where $X(E) = X_{esc}(E) + X_{par}(E) + X_{reabs}(E)$.

Figure 2.6 shows the PLQY = f(η_{int}) curves calculated from **Eq. (2.22)** for the cell structure and layer thicknesses taken from **Figure 2.2** (a). In a first calculation, experimentally-measured dielectric functions were used for all the layers. Among these layers, only the Au and ITO ones cause parasitic absorption due to their non-zero optical absorption in the spectral region of the perovskite fluorescence. SnO_2, Spiro-OMeTAD and glass do not contribute to parasitic absorption because they are transparent to the emitted photons. In a second calculation, the optical absorption by ITO was removed in the spectral region of the perovskite fluorescence. In a third calculation, the optical absorption by both ITO and Au was removed. This enables estimating the contribution of parasitic absorption in these two materials. For small η_{int} values, taking parasitic absorption into account makes a negligible difference on the PLQY value. In contrast, parasitic absorption would have a drastic effect on PLQY if radiative recombination was eliminated, i.e. for η_{int} = 100%. In this case, parasitic absorption in both ITO and Au limits the cell PLQY to 60%. By removing the absorption from the ITO, PLQY increases to 90%. By cancelling the absorption by ITO and Au, 100% PLQY is recovered. Therefore, the main factor limiting PLQY in this case is parasitic absorption in the ITO front electrode.

For the sake of completeness, predictions of the current model are compared with those of one of the most advanced models recently used by M. G. Abebe et. al. to compute the effect of parasitic absorption on the PLQY and V_{oc} of perovskite solar cells (see Appendix A.4). This

model stands on the use of Green functions and thus includes coherent effects to rigorously determine the spatial power distribution of dipole emission. In spite of the simplifying assumption of a homogeneous power distribution made to derive **Eq. (2.22)**, both models lead to comparable PLQY values when $\eta_{int} \rightarrow 100\%$ and to the same conclusion that most parasitic absorption occurs in the ITO.

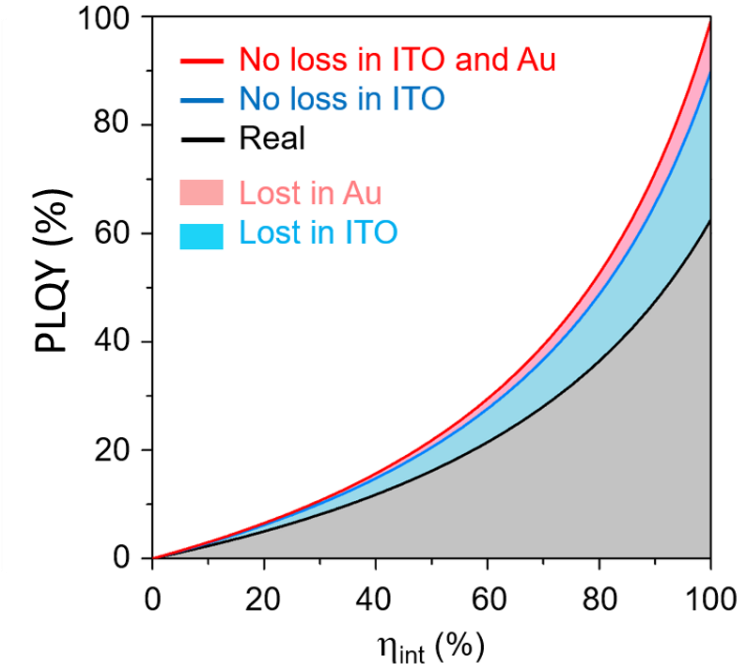

Figure 2.6. Effect of parasitic absorption on the PLQY for our perovskite solar cells, calculated as a function of η_{int} according to **Eq. (2.22)** with the cell structure and layer thicknesses of **Figure 2.2** (a) and experimentally-determined dielectric functions for the different layers (black solid line), with optical absorption cancelled in the ITO (blue solid line, no loss in ITO), with optical absorption cancelled in the ITO and Au (red solid line, no loss in ITO and Au). The losses in ITO and Au are shown as coloured areas (blue and pink, respectively).

2.5.3 Energy barriers causing a deviation from the ideal diode behaviour

To determine the origin of the deviation from the ideal diode observed in section 2.4, a correlation was searched between the voltage loss δV and the photovoltaic parameters of the cells: PCE, J_{sc}, R_s, FF, R_{sh}. As already discussed in the caption of **Figure 2.3** (a), the δV of each cell is the difference between its simulated ideal diode V_{oc} and the measured V_{oc}. The simulated ideal diode V_{oc} of a given cell from the $FA_{0.8}MA_{0.2}PbI_{3-y}Br_y$ series is calculated using **Eq. (1.9)**, with $V_{oc,rad}$ = 1.28 V being obtained from **Eq. (2.1)** and PLQY being set at the

measured value for this cell. **Figure 2.7** (a) shows the current-voltage curves of selected cells representative of the whole series together with the corresponding V_{oc}, J_{sc}, FF and PCE. The current-voltage curves of the champion device are depicted in Appendix. A.5. The different PCE of these cells mainly occurs due to their different FF and J_{sc}, while their V_{oc} is similar. The effect of shunt resistance (R_{sh}) on V_{oc} has been simulated and shown that the shunt resistance values obtained experimentally do not affect the V_{oc}, see Appendix A.6. The PCE, J_{sc}, FF, series resistance (R_s) and R_{sh} appear to be correlated, a high PCE occurring together with a high J_{sc}, high FF, low R_s and high R_{sh}, as seen in **Figure 2.8**. δV seems to present a correlation with these photovoltaic parameters, as shown in **Figure 2.7** (b) where δV tends to decreases when PCE increases.

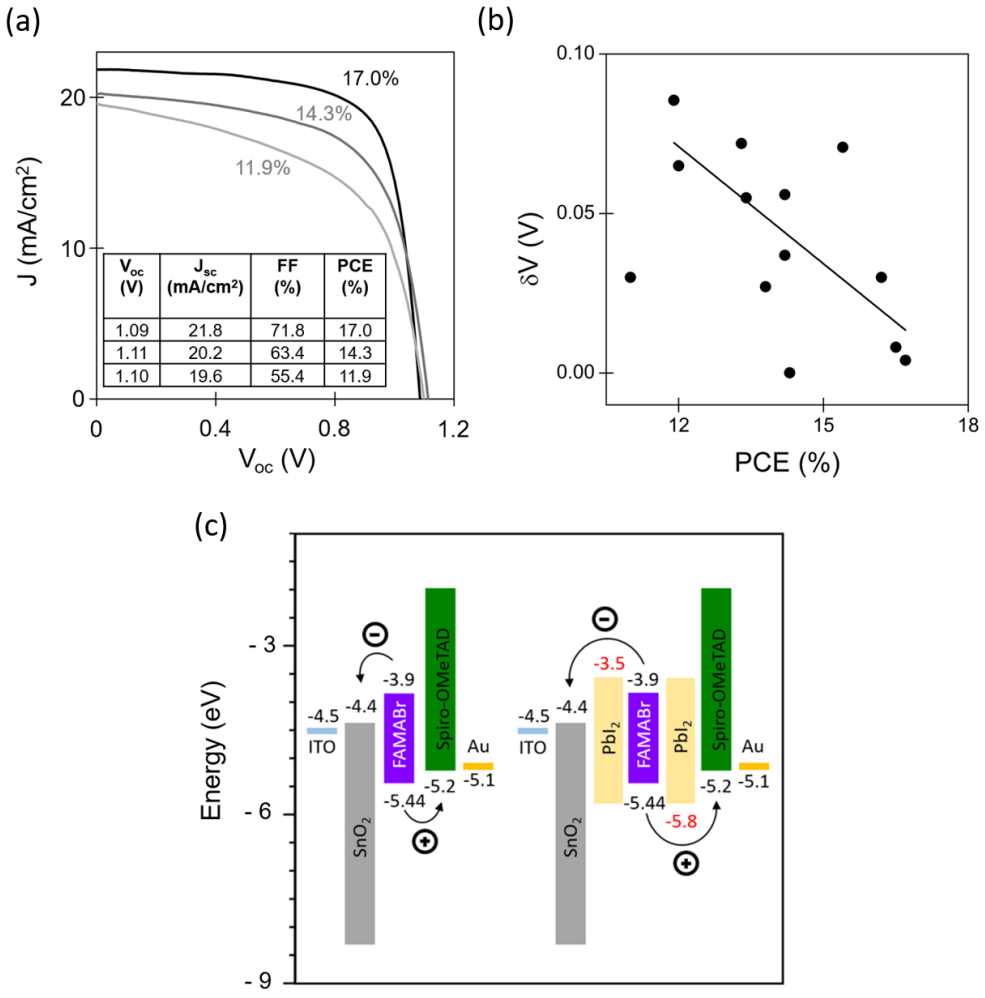

Figure 2.7. (a) Current-voltage curves of selected solar cells representative of the whole series. (b) Voltage loss δV plotted as a function of PCE. The solid line was obtained by fitting the experimental data points. (c) Energy diagrams for $FA_{0.8}MA_{0.2}PbI_{3-y}Br_y$ (FAMABr) solar cells without and with passivating PbI_2 layer.

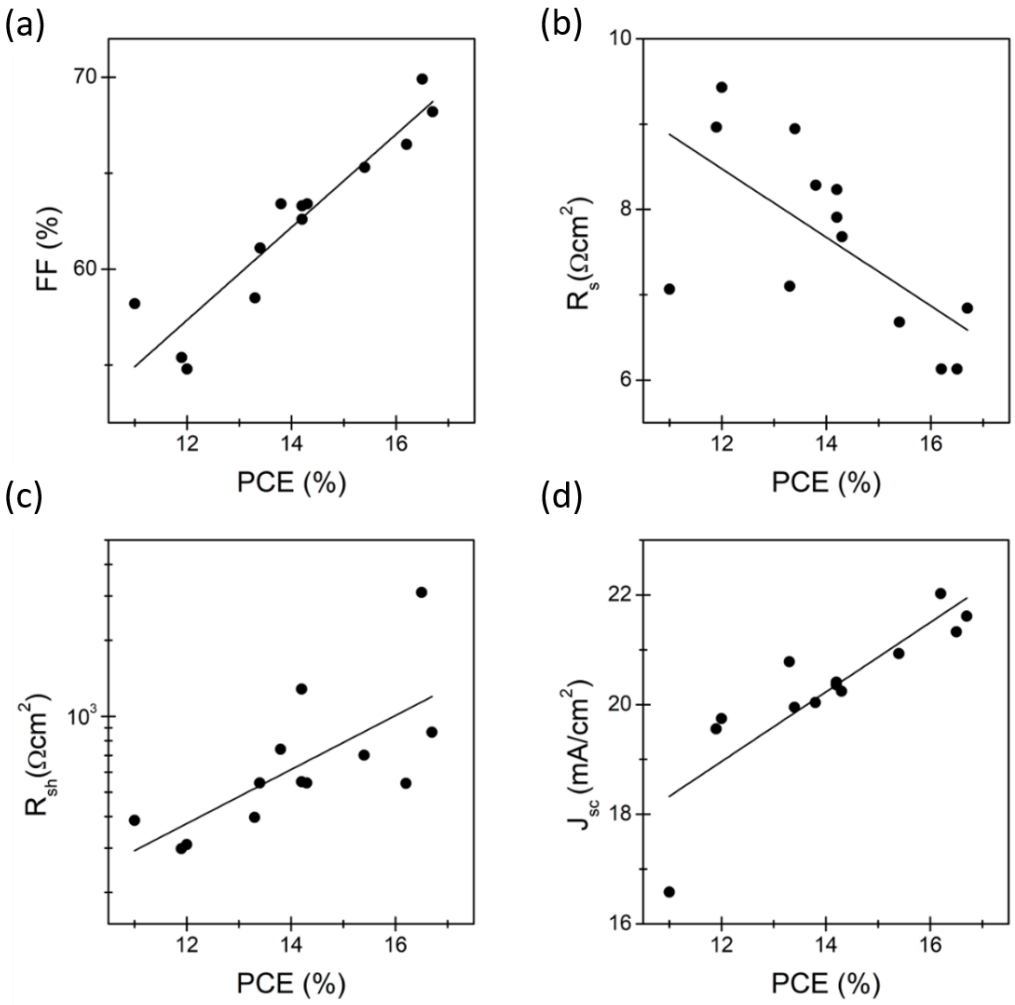

Figure 2.8. (a) Fill factor, (b) series resistance, (c) shunt resistance (d) and short circuit current as a function of power conversion efficiency of $FA_{0.8}MA_{0.2}PbI_{3-y}Br_y$ based perovskite solar cells. Shunt and series resistance values have been derived from J-V curves for a range of solar cells.

By combining the information from **Figure 2.7** (b) and **Figure 2.3** (b), one sees that the cells with a high PCE present a low PLQY and a low δV. On the opposite side, cells with a low PCE present a high PLQY and a high δV. This suggests that trap removal (high PLQY) occurs together with the formation of energy barriers that lower the PCE and induce an internal voltage drop (high δV). In particular, the lowered PCE is linked with a degraded charge extraction (low J_{sc}). It is proposed that these three phenomena occur simultaneously when the perovskite contains an excess PbI_2. Excess PbI_2 passivates electron traps in the perovskite and thus tends to increase PLQY. If accumulated in a too large amount at the electron transport layer/perovskite interface, it introduces simultaneously a negative energy mismatch with SnO_2

and a positive mismatch with the perovskite, as shown in the proposed energy diagram of **Figure 2.7** (c). Such opposite mismatches are responsible for an internal voltage drop due to the offset of the electron quasi - Fermi level and a degraded electron extraction, respectively. Similar effects can be caused due to an excess PbI_2 at the perovskite/Spiro-OMeTAD interface. In such cases, as also shown in **Figure 2.7** (c) the PbI_2 introduces a negative energy mismatch with the perovskite that may induce an internal voltage drop due to the offset of the hole quasi – Fermi level, and a positive energy mismatch that degrades hole extraction. The presence of excess PbI_2 at both interfaces in the cells with a high PLQY, low PCE and high δV is confirmed by scanning electron microscopy are shown in **Figure 2.9**. In the corresponding microscope image, the bright regions correspond to PbI_2.

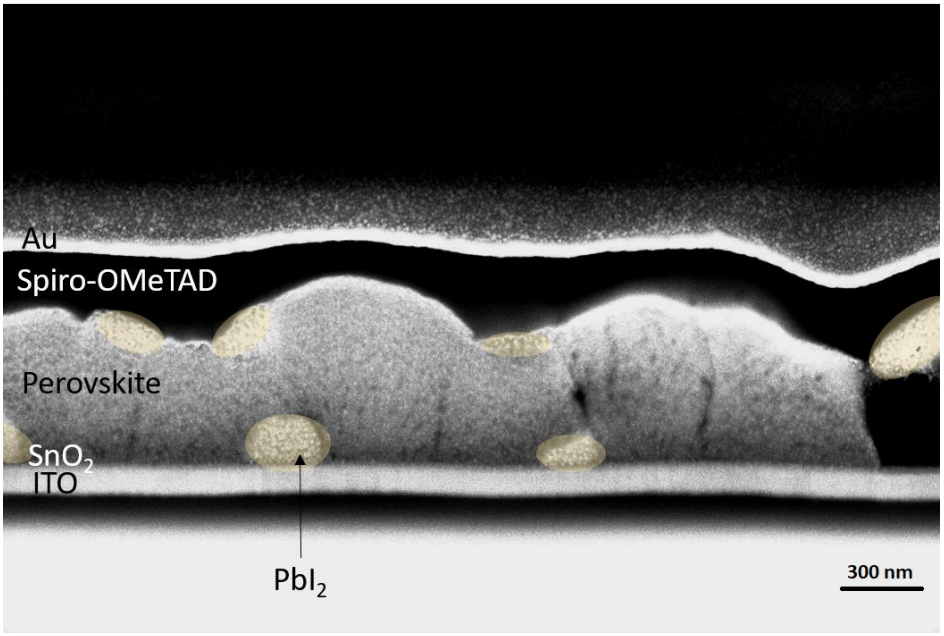

Figure 2.9. SEM cross-section image of a perovskite solar cell with structure ITO/SnO_2/ $FA_{0.8}MA_{0.2}PbI_{3-y}Br_y$/Spiro-OMeTAD/Au. Lighter regions, the larger ones being highlighted in yellow, correspond to the passivating PbI_2 material. Fluctuations in the perovskite thickness between 450 nm and 700 nm can be seen.

These findings are in agreement with previous reports, which showed that having the right amount of PbI_2, enough to effectively passivate the defects but insufficient to limit the charge transport to the electrodes, in a perovskite solar cell is necessary for optimal cell performance. They also provide an example on how the variability of the two-step fabrication method can affect the perovskite composition and structure and thus the device performance. In other works, for example, the employed two-step approaches were shown to induce a PbI_2 deficiency

or microscale inhomogeneities affecting the energy band alignment in the cell, hence lowering the V_{oc}.

2.5.4 Dominant non-idealities in cells from the literature

In previous sections of this chapter, non-idealities that contribute to limiting the V_{oc} of our cells were observed. We analysed the non-radiative recombination and parasitic absorption that limit PLQY, the energy barrier that introduces a voltage drop δV with respect to ideal diode behaviour, and the contribution of these non-idealities. For the sake of completeness, a similar analysis is now provided for the cells reported in **Ref. 25** and **Ref. 26**, which present layered structures different from ours and were fabricated following different methods. This analysis gives insights into the impact of the cell structure and fabrication method on the different non-idealities and thus on V_{oc}. Recall that the measured V_{oc} and PLQY of these cells are shown in **Figure 2.2** (b) together with their calculated ideal diode V_{oc} = f(PLQY) relations. Their corresponding energy diagrams and calculated PLQY = f(η_{int}) diagrams are depicted in the figure below.

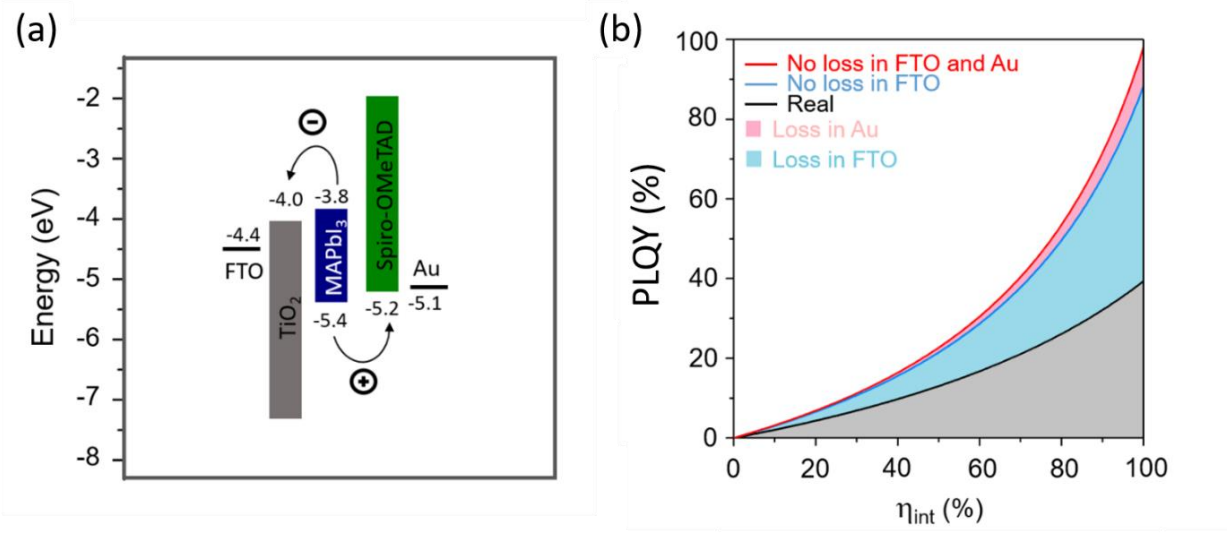

Figure 2.10. (a) Energy diagrams of the $MAPbI_3$ solar cell from **Ref. 25.** (b) PLQY calculated as a function of η_{int} showing the parasitic absorption contribution by the different layers in the solar cell. Energy levels for $MAPbI_3$ have been taken from reference literature.

For the cells of **Ref. 25** with a structure of Fluorine-doped Tin Oxide (FTO)/TiO_2/$MAPbI_3$ or $Cs_xFA_yMA_{1-x-y}PbI_3$/Spiro-OMeTAD/Au, the authors measured relatively high PLQYs (4-5%) resulting from an efficient reduction of non-radiative recombination. Nevertheless, their cell structure included a 500 nm thick FTO layer generating an important parasitic absorption. This parasitic absorption would limit the PLQY to 40% if non-radiative recombination were to

be fully removed. Moreover, they reported a significant δV that they tentatively attributed to losses at contacts, yet without further detail. Finding the origin of such δV is not straightforward. However, in the case of their $Cs_xFA_yMA_{1-x-y}PbI_3$ cell, a strong energy mismatch occurs at the perovskite/hole transport layer. In the case of their $MAPbI_3$ cell, the dominant energy mismatch occurs at the electron transport layer/FTO interface.

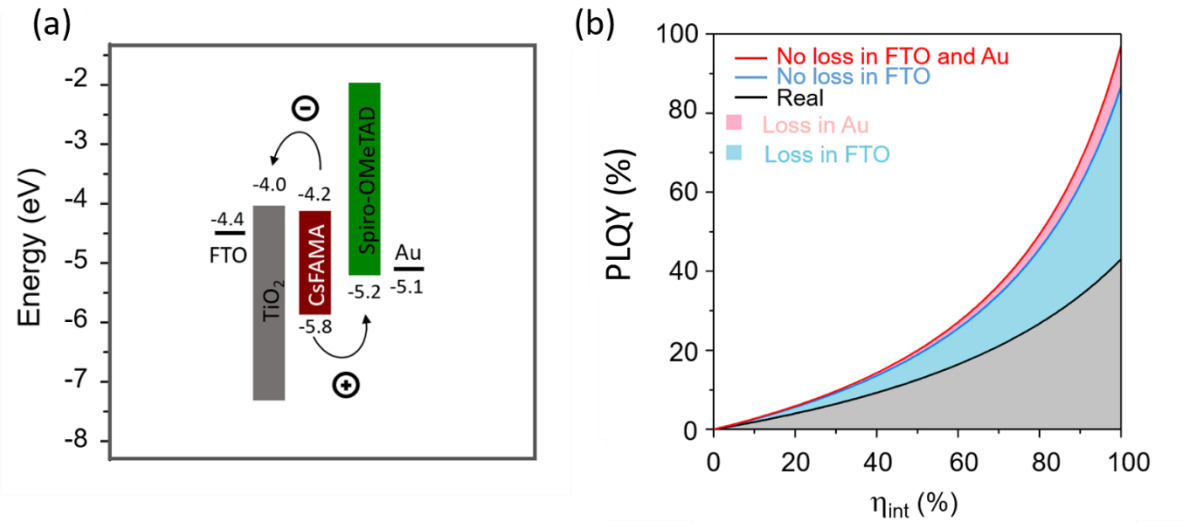

Figure 2.11. (a) Energy diagrams of the $Cs_xFA_yMA_{1-x-y}PbI_3$ (CsFAMA) solar cell from **Ref. 25**. (b) PLQY calculated as a function of η_{int} showing the parasitic absorption contribution by the different layers in the solar cell. Energy levels for $Cs_xFA_yMA_{1-x-y}PbI_3$ have been taken from the literature.

In **Ref. 26** ITO/ Poly(triaryl amine) (PTAA)/$MAPbI_3$/ Phenyl-C61-butyric acid methyl ester (PCBM)/Ag, the authors realised an efficient trap passivation by employing PTAA and PCBM charge transport layers, thus enabling a relatively high PLQY (5%) for their cells. This passivation, together with the material choice enabling a stair-like energy profile across the device with relatively small energy mismatches at the perovskite interfaces, led to a negligible voltage loss δV.

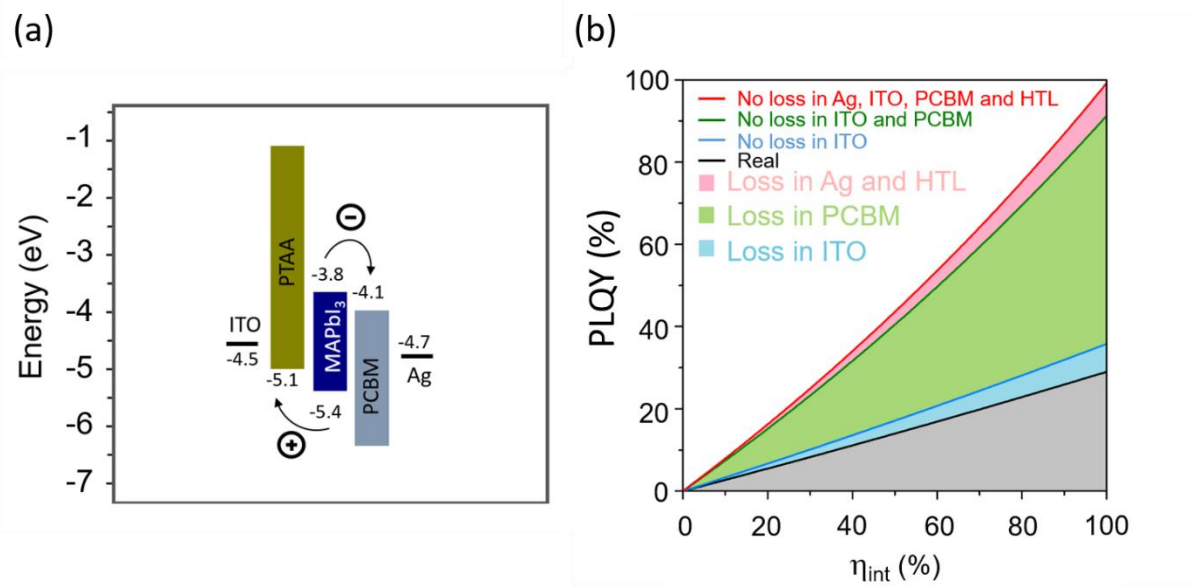

Figure 2.12. (a) Energy diagrams of solar cell from **Ref. 26**. (b) PLQY calculated as a function of η_{int} showing the parasitic absorption contribution by the different layers in the solar cell. Energy levels for $MAPbI_3$ have been taken from the literature.

The ITO layer was thinner than usual, thus reducing the probability of parasitic absorption in this layer. In fact, parasitic absorption mainly occurs in the PCBM layer, which presents significant optical absorption in the spectral region of the $MAPbI_3$ perovskite fluorescence. Parasitic absorption in the PCBM would play a central role in limiting the PLQY of this type of cell to 25% if non-radiative recombination were to be fully removed. Therefore, the PCBM layer provides simultaneously a positive effect on the perovskite layer, passivation of its surface, but introduces a parasitic absorption which has a negative effect. This example, together with the trends observed in our cells, demonstrate that a device design approach thought to reduce one of the non-idealities may enhance the others.

2.6 Conclusions

Summarising, the complete $FA_{0.8}MA_{0.2}PbI_{3-y}Br_y$ solar cells considered in this work present external quantum yields PLQYs ranging from 0.1 to 3% and V_{oc}s from 1 to 1.13 V. The measured V_{oc}s are still significantly lower than $V_{oc,rad}$ (1.28 V). The main reason for such low V_{oc} is the low PLQY of the cells. It was found that such low PLQY results to a large extent from non-radiative photocarrier recombination at long-lived traps in the cell. It was also predicted that not only non-radiative recombination limits the PLQY of complete solar cells.

If non-radiative recombination was suppressed, the PLQY would be far from reaching its maximum value because of parasitic absorption, first in the ITO front electrode and second in the Au mirror. The second and less expected reason for the non-optimal V_{oc} of the cells is a deviation from the ideal diode behaviour. This deviation is materialised by a voltage loss δV, which increases with PLQY. This shows that a too efficient trap passivation in our cells, likely mediated by excess PbI_2 as shown in **Figure 2.7**, while being positive for PLQY, introduces energy barriers that are detrimental to the V_{oc} and cell efficiency. In fact, the cell with the largest PCE measured presents a low level of trap passivation with a PLQY lower than 1% under one sun-equivalent illumination. After identifying the non-idealities that limit the V_{oc} of our cells and addressing their relative impact, their role in devices reported in the literature was discussed. The conclusion from such a discussion was that cell structure and preparation methods have important effects on these non-idealities, and that an approach thought to eliminate one of them may enhance the others. In the next chapter describe a fabrication method which avoids an over- passivation (PbI_2 excess) of the perovskite active layer and results in increased PLQY values.

Chapter 3

Fabrication of high-quality perovskites with low band gap and high open-circuit voltage

3.1 Introduction

In the previous chapter we analysed the overall effect on the performance of the solar cells when strategies are implemented to increase the PLQY. We saw that such an increase may, in general, not necessarily lead to a V_{oc} increase. In this chapter we implement the strategy of increasing the average perovskite crystal size within the corresponding layer in the solar cell to increase the PLQY. By following such an approach, we are able to reduce the specific interface area and by the same token reduce non-radiative recombination at the interface. By comparing the perovskite cells with larger crystalline domains to cells with smaller crystalline domains, we are able to clearly demonstrate that an increase in PLQY can be correlated to an increase in V_{oc}.

3.2 Compact PbI_2-templated growth for the fabrication of high-quality microcrystal

To fabricate a high crystal quality $FA_{1-x}MA_xPbI_3$ perovskite by the two-step method, we developed a "compact PbI_2-templated perovskite growth" approach whose main steps are depicted in **Figure 3.1** (a). A high-concentration FAI:MACl organic solution is spun onto a compact PbI_2 film, followed by a solvent annealing that consists in annealing the material under a solvent vapor. By combining the effects of the highly concentrated organic precursor solution, Cl^- addition, and solvent annealing, this approach enables an efficient interdiffusion of the organic precursor into the compact PbI_2 lattice, and the formation of a perovskite layer with crystal lateral dimensions larger than 1 μm as seen in the scanning electron microscopy (SEM) image from **Figure 3.1** (a). As shown by the X-ray diffraction (XRD) pattern of the fabricated perovskite layer shown in **Figure 3.1** (b), the compact PbI_2-templated growth approach enables the formation of perovskite crystals without any trace of the hexagonal phase. The peak positions, weakly shifted toward large angles compared with a reference $FA_{0.85}MA_{0.15}PbI_3$ pattern, indicate slightly smaller lattice dimensions, that is, a slightly higher MA+ content. This is consistent with the expected composition, $FA_{0.8}MA_{0.2}PbI_3$.

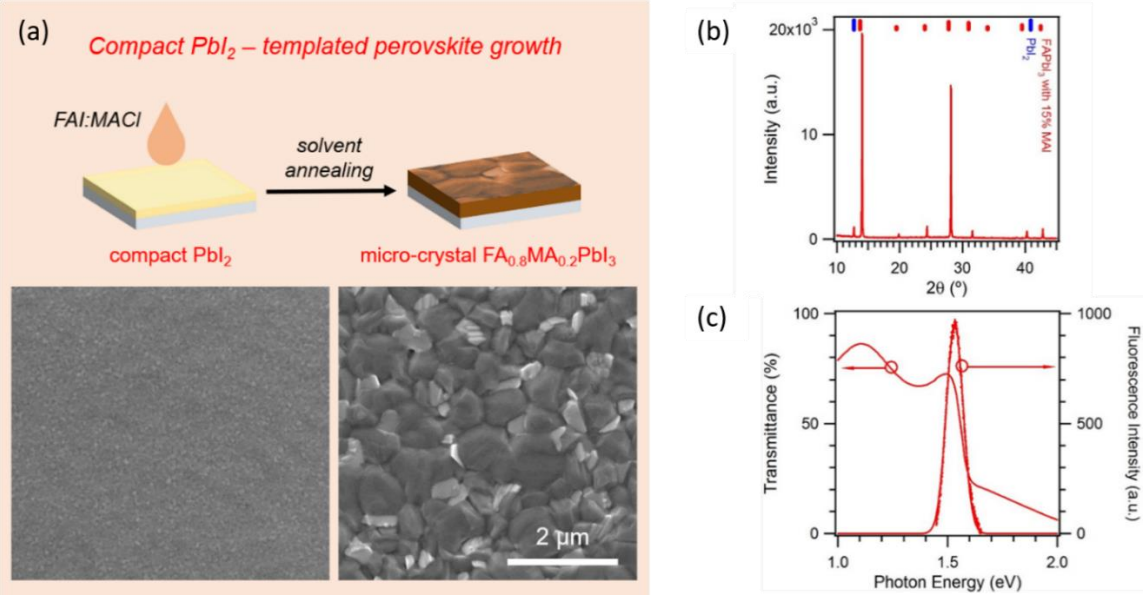

Figure 3.1. Two-step deposition: compact PbI_2-templated perovskite growth to achieve a high-quality microcrystal $FA_{0.8}MA_{0.2}PbI_3$ perovskite layer. (a) This approach consists in spin-coating a FAI:MACl solution onto a compact PbI_2 film, followed by solvent annealing (top panel). Because the initial PbI_2 layer can be considered as a single structure (bottom left panel, top-view SEM image), it does not limit the lateral growth of the perovskite crystals whose lateral size reaches beyond 1 µm (bottom right panel, top-view SEM image). (b) XRD pattern of the fabricated perovskite layer. The position of the main diffraction peaks of PbI_2 and a mixed cation hybrid lead halide perovskite are shown at the top for comparison. (c) Transmittance and fluorescence spectra of the fabricated perovskite layer.

Note that the proposed final composition does not include chlorine, which even if introduced during the preparation, is usually not present with a significant concentration in hybrid lead halide perovskites, owing to the small radius of the Cl^- anion that makes it easy to exodiffuse from the crystal lattice. The XRD pattern also indicates that a small amount of PbI_2 is present, probably because of a surface self-passivation of the perovskite crystals rather than the presence of unreacted PbI_2, as was already discussed in Chapter 2. This is confirmed from cross-section SEM images in Section 3.4. The transmittance and fluorescence spectra of the fabricated perovskite layer represented in **Figure 3.1** (c) show, respectively, the perovskite absorption onset and radiative recombination peak both near 1.52−1.53 eV (810 nm). Such values confirm that the band gap of the fabricated perovskite layer is narrower than that of $MAPbI_3$ perovskites (1.57 eV), as targeted by the FA+ incorporation. Note that, for the growth of crystals with the targeted large size and excellent optoelectronic properties using the

compact PbI_2-templated growth, a deliberate choice of specific and suitable fabrication conditions, combining the Cl^- anion addition to a highly-concentrated organic precursor with a post-spin-coating solvent annealing, is mandatory. As can be seen again in **Figure 3.2**, in such conditions (FAI:MACl + solvent annealing) one can obtain perovskite crystals with sizes above 1 μm. These are significantly larger than the crystal sizes one may achieve when following other more simple procedures where no Cl^- anions are added to the organic precursor (FAI:MAI + solvent annealing), or a standard thermal annealing is performed instead of the solvent annealing (FAI:MACl + thermal annealing), or a standard thermal annealing is performed with no Cl^- anions (FAI:MAI + thermal annealing). Without Cl^- anion addition, the dissolution of the compact PbI_2 template required for FA^+ ion incorporation is not efficient, thus leading to a limited perovskite crystal nucleation. During a standard thermal annealing, which is performed without solvent vapor, a poor mass transport takes place, thus limiting the growth of the perovskite crystals. To establish a reference for the study of the fluorescence and photovoltaic properties of the compact PbI_2-templated perovskites, we also grew $FA_{0.8}MA_{0.2}PbI_3$ perovskite layers following the "standard" approach based on using a porous PbI_2 film as the template. With this approach, which is called hereafter "porous PbI_2-templated growth", the perovskite formed consists of smaller crystals than the compact PbI_2-templated one, while presenting a similar position for its optical absorption onset and radiative recombination peak. The details on measurements of XRD patterns and SEM characterisation are shown in Appendix B.1.

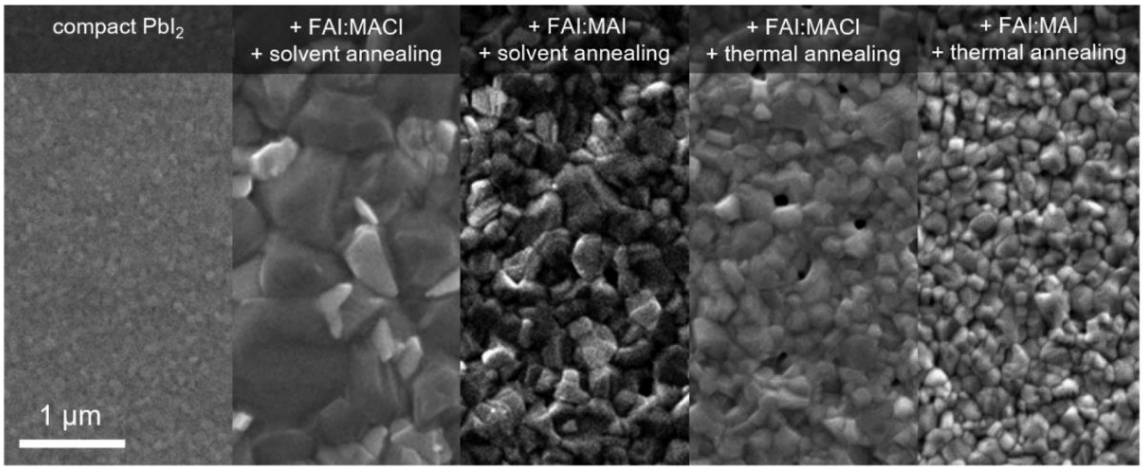

Figure 3.2. Top-view SEM images of the initial compact PbI_2 film and of perovskite films formed from it after: FAI:MACl + solvent annealing; FAI:MAI + solvent annealing (no Cl^-); FAI:MACl + thermal annealing (no solvent annealing); FAI:MAI + thermal annealing (no Cl^-, no solvent annealing). A microcrystal perovskite is obtained only with the combination of Cl^- incorporation and solvent annealing.

3.3 Fabrication, structure and optical properties of the porous PbI_2 - templated $FA_{0.8}MA_{0.2}PbI_3$ perovskite layer

With the approach called "porous PbI_2 – templated growth", a high-concentration FAI:MACl organic solution is spun onto a porous PbI_2 film, followed by a solvent annealing, as shown in **Figure 3.3** (a). The formed perovskite layer consists of crystals a few hundreds of nm in size. The XRD pattern of the fabricated perovskite layer is plotted in **Figure 3.3** (b), showing no trace of the hexagonal phase and a small amount of PbI_2 attributed to self-passivation of the perovskite crystals. The peak positions, weakly shifted toward large angles compared with a reference $FA_{0.85}MA_{0.15}PbI_3$ pattern, are consistent with the expected composition, $FA_{0.8}MA_{0.2}PbI_3$. The transmittance and fluorescence spectra of the fabricated perovskite layer represented in **Figure 3.3** (c) show, respectively, the perovskite absorption onset and the radiative recombination peak both near 1.52 – 1.53 eV (810 nm). More details on the fabrication process and a scheme of the process flow and perovskite formation mechanism are shown in Appendix B.2.

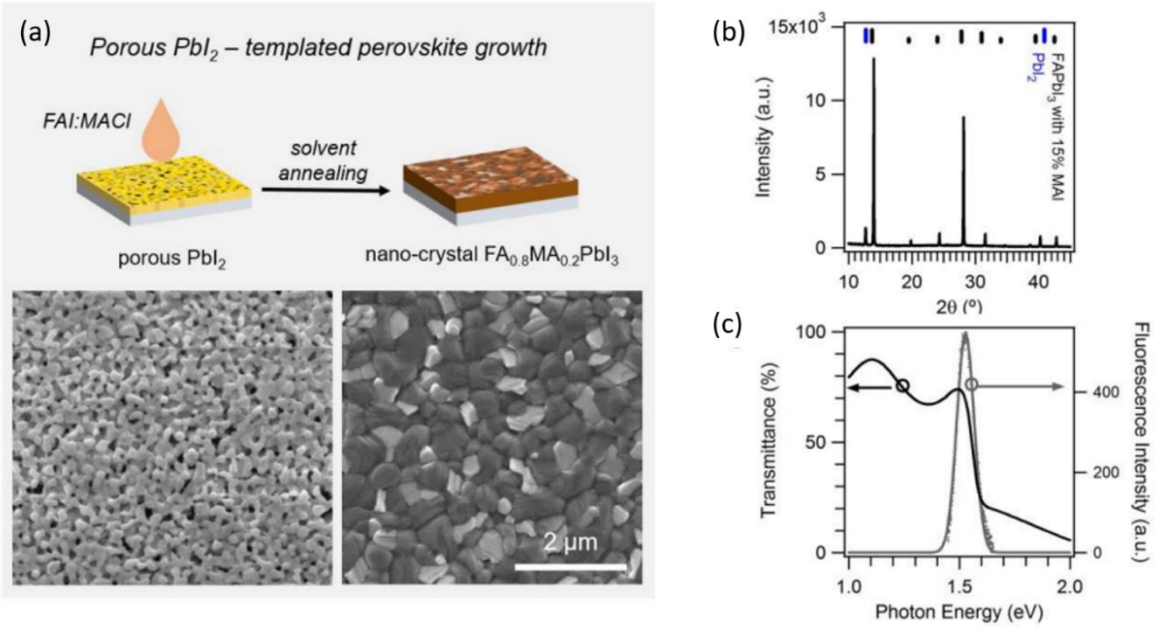

Figure 3.3. Two-step deposition: porous PbI_2 – templated perovskite growth to achieve a nano-crystal $FA_{0.8}MA_{0.2}PbI_3$ perovskite layer. (a) This approach consists in spin-coating a FAI:MACl solution onto a porous PbI_2 film, followed by a solvent annealing (top panel). The obtained perovskite layer (top-view SEM image, bottom right panel) consists of nanoscale crystals whose limit size is imposed by the dimensions and density of the initial PbI_2 structures (top-view SEM image, bottom left panel). (b) XRD pattern of the fabricated perovskite film. The position of the main diffraction peaks of PbI_2 and a mixed cation hybrid lead halide

perovskite ($FAPbI_3$ with 15% MAI) are shown at the top. (c) Transmittance and fluorescence spectra of the fabricated perovskite film.

3.4 Comparison of the structure, and optical properties of the compact PbI_2 – templated and porous PbI_2 – templated $FA_{0.8}MA_{0.2}PbI_3$ perovskite layers

As seen in **Figure 3.4** (a), the perovskite layer fabricated by compact PbI_2 – templated growth consists of larger crystals than those fabricated by porous PbI_2 – templated growth, with lateral sizes of a few μm versus a few hundreds of nm. The XRD pattern of such micro-crystal perovskite, depicted in **Figure 3.4** (b) shows peaks at similar positions as the nano-crystal perovskite fabricated by porous PbI_2 – templated growth, confirming that both have similar compositions.

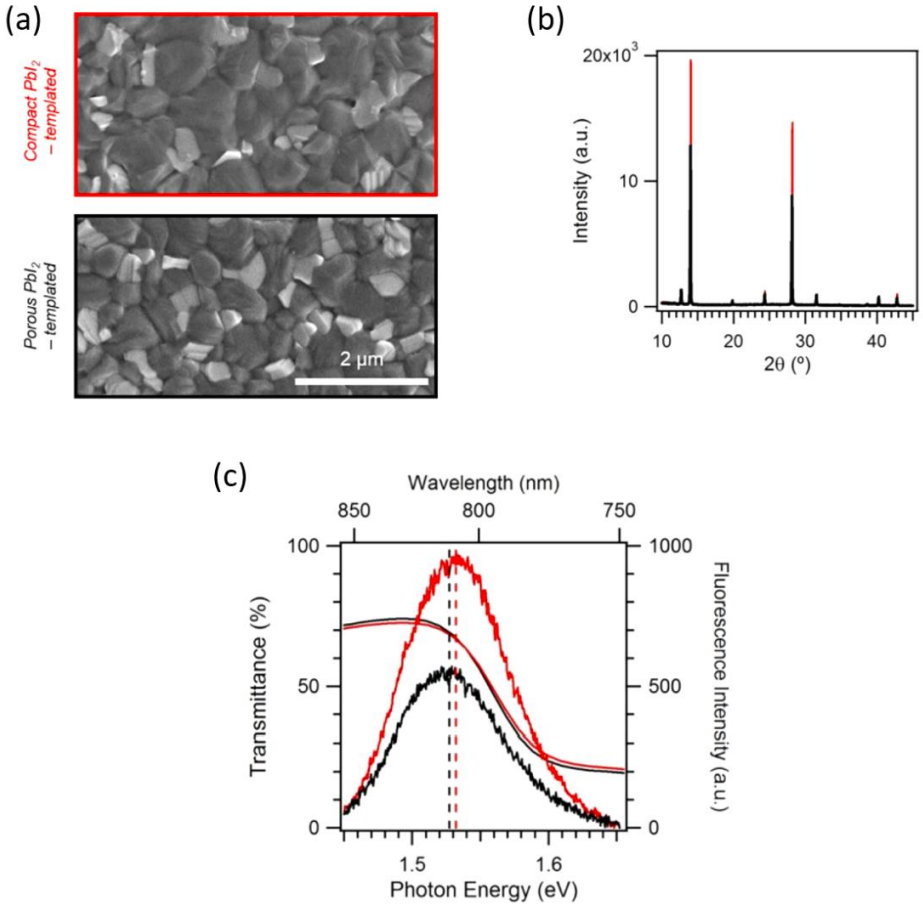

Figure 3.4. (a) Top-view SEM images of the compact PbI_2 – templated and porous PbI_2 – templated perovskite layers. Crystals with larger lateral dimensions were observed for the former (more than 1 μm) than for the latter (hundreds of nm). (b) XRD patterns of the two kinds of layers. They show similar peak positions but a stronger intensity for the compact PbI_2

– templated perovskite layer pointing at a better crystallinity (larger coherent diffraction domains). (c) Transmittance and fluorescence spectra of the two kinds of layers in the spectral region of the perovskite band gap. The perovskite band gap absorption onset and the perovskite fluorescence peak appear at similar photon energies, suggesting a similar band gap for both kinds of films. Nonetheless, the compact PbI_2 – templated one presents a stronger fluorescence signal.

This is further supported by the transmittance and fluorescence spectra in **Figure 3.4** (c) that show a similar position for the absorption onset and radiative recombination peak, which is near 1.52-1.53 eV for both perovskites. However, note that the perovskite fabricated by compact PbI_2 – templated growth presents stronger XRD and fluorescence peaks than that fabricated by porous PbI_2 – templated growth. This is consistent with the larger crystal size for the former perovskite than for the latter one.

3.5 Impact of the perovskite crystal size on the fluorescence quantum yield.

To evaluate the contribution of radiative and nonradiative recombination paths for photocarriers in the compact PbI_2-templated and porous PbI_2- templated perovskite layers, the external fluorescence quantum yield of such layers grown on a TiO_2 layer was measured using an integrated sphere-based setup depicted in **Figure 2.3** (a). The measurement has been performed in the same matter and conditions as described in Chapter 2. As shown in **Figure 3.5** (b), the perovskite layers fabricated by the two approaches present a high external fluorescence quantum yield, with a photon flux-dependent (increase saturation) behaviour that indicates that a trap-filling mechanism takes place. The different perovskite crystal size achieved with the two approaches has a strong controllable impact on the external fluorescence quantum yield. The compact PbI_2-templated perovskite layer, which has the largest crystals, presents the highest external fluorescence quantum yield at all photon fluxes, with values near 4% for a 1-sun equivalent illumination, and near 20% at saturation, for a 70-sun equivalent illumination. These are among the highest values for polycrystalline perovskite films found in the literature without specific passivation treatment, suggesting a particularly high contribution of radiative recombination paths, that is, a particularly low defect density. Note that the external fluorescence quantum yield of the porous PbI_2-templated perovskite layer for a 70-sun equivalent illumination reaches only 8%, suggesting the existence of another type of non-saturable defects opening additional nonradiative recombination paths.

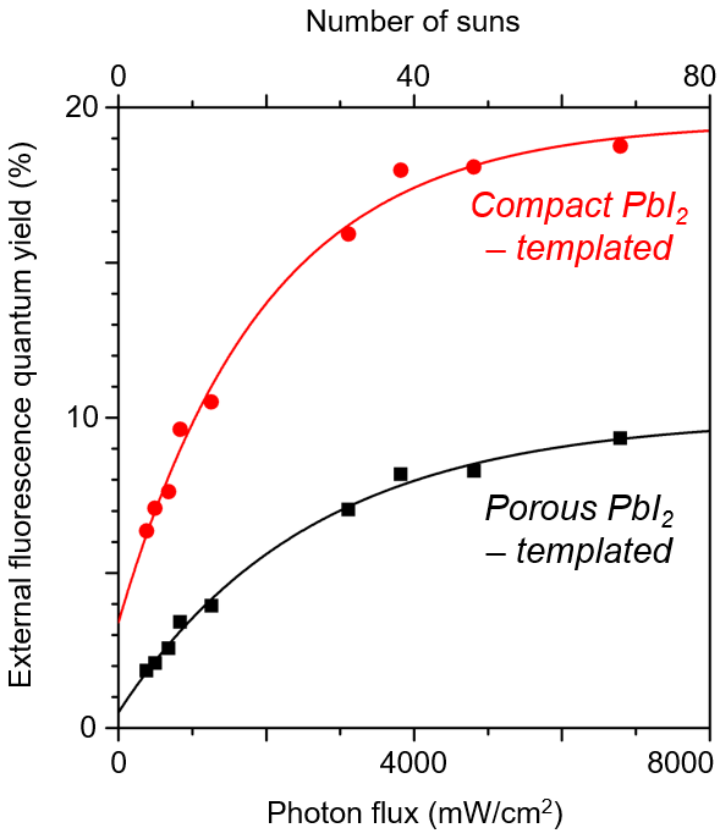

Figure 3.5. Measured external fluorescence quantum yield as a function of the incident photon flux. The compact PbI_2- templated perovskite layer shows a higher external fluorescence quantum yield at all fluxes than the porous PbI_2-templated one. The flux dependence of the external fluorescence quantum yield, represented by increased saturation, indicates an important trap-filling mechanism for both kinds of perovskites. The fit of experimental data points is represented by solid lines.

3.6 Impact of the perovskite crystal size on solar cell performance.

The crystal size in the fabricated perovskite layers impacts the photovoltaic properties of solar cells based on them. Although a series of 50 cells were fabricated following each approach, we first focused on comparing the nanostructure and photovoltaic properties of selected cells of each type to separate examples representative of the trends over the whole series. Cross-section SEM images corresponding to cells of the two types are shown in **Figure 3.6** (a). These images provide evidence of the dependence of the perovskite crystal size on the fabrication approach. In the compact PbI_2-templated cell, the perovskite crystals are not only particularly large in the lateral directions, having sizes superior to 1 μm, but also along the

direction perpendicular to the substrate. Additional SEM images are provided in Appendix B.4. Their height equals the thickness of the active perovskite layer, and the grain boundaries between the crystals are vertical. In contrast, in the porous PbI_2-templated cell, the active perovskite layer consists of a stack of crystals separated by transverse grain boundaries. The larger perovskite crystals in the compact PbI_2-templated cells and their lower nonradiative recombination probability correlate with a higher V_{oc}. This is illustrated in **Figure 3.6** (b) that shows the dependence of V_{oc} as a function of the incident photon flux below 1 sun, for a compact PbI_2-templated cell and a porous PbI_2-templated cell. A logarithmic relationship with a slope superior to kT/q is obtained for the cells fabricated following both approaches. This indicates the existence of a significant nonradiative trap-assisted recombination pathway. A smaller slope (1.16kT/q) is obtained for the compact PbI_2- templated cell than for the porous PbI_2-templated one (1.4kT/ q), indicating less energy loss from nonradiative trap-assisted recombination in the former case. Such a lower loss enables a higher V_{oc} at all photon fluxes in the investigated range. While the perovskite fabrication approach impacts markedly the V_{oc} of the cells, it affects less of their other photovoltaic parameters, in particular, J_{sc}. This is exemplified in **Figure 3.7** (c) which presents the optimal J−V curve of the best cell of each type. Both present similar J_{sc} values, which reflect a similar light-harvesting performance that can be further analysed from their external quantum efficiency (EQE) spectra shown in **Figure 3.7** (a). In contrast, a markedly higher V_{oc} is observed for the compact PbI_2-templated cell, being 1.13 V for compact PbI_2-templated and 0.99 V for porous PbI_2-templated. This higher V_{oc} is responsible for the higher PCE of this cell, being 19.3% for compact PbI_2-templated and 17.5% for porous PbI_2-templated. Note that the higher performance of the compact PbI_2-templated cell is also evidenced after stabilisation in steady state measurements, as shown in **Figure 3.7** (b), and that the compact PbI_2-templated cell shows a better stability than the porous PbI_2-templated one, as depicted in **Figure 3.7** (c). The most probable values of V_{oc}, J_{sc}, FF, and PCE obtained for the 50 cells of each type, depicted in **Table 3.1,** confirm that the examples above provide trends representative of the whole cell series. The details on photovoltaic measurements are provided in Appendix B.3.

Table 3.1. Photovoltaic performance of the compact PbI_2-templated and porous PbI_2-templated solar cells.

Device type		V_{oc} (V)	J_{sc} (mA/cm^2)	FF (%)	PCE (%)
Compact PbI_2 - template	Best	1.13	23.0	74.6	19.3
	50 devices	1.05 ± 0.04	22.8 ± 0.5	75.9 ± 2.3	18.0 ± 0.4
Porous PbI_2 - template	Best	0.99	23.2	76.2	17.5
	50 devices	0.97 ± 0.02	23.1 ± 0.5	72.1 ± 3.5	16.1 ± 1.3

The V_{oc} of the compact PbI_2-templated cell series is 8.3% higher than that of the porous PbI_2-templated ones. In contrast, a smaller relative difference in J_{sc} and FF between the two-cell series is found: it amounts to 1.3 and 5.2%, respectively. Therefore, the 11.8% higher PCE observed for the compact PbI_2-templated cell series results mainly from its higher V_{oc}. Such statistical correlation between V_{oc} and PCE is particularly clear from their distributions plotted in **Figure 3.6** (d) and (e). Both distributions peak at smaller values for the porous PbI_2-templated cell series (0.97 V, 16.1%) than for the compact PbI_2-templated one (1.05 V, 18.0%), with a small overlap between both series.

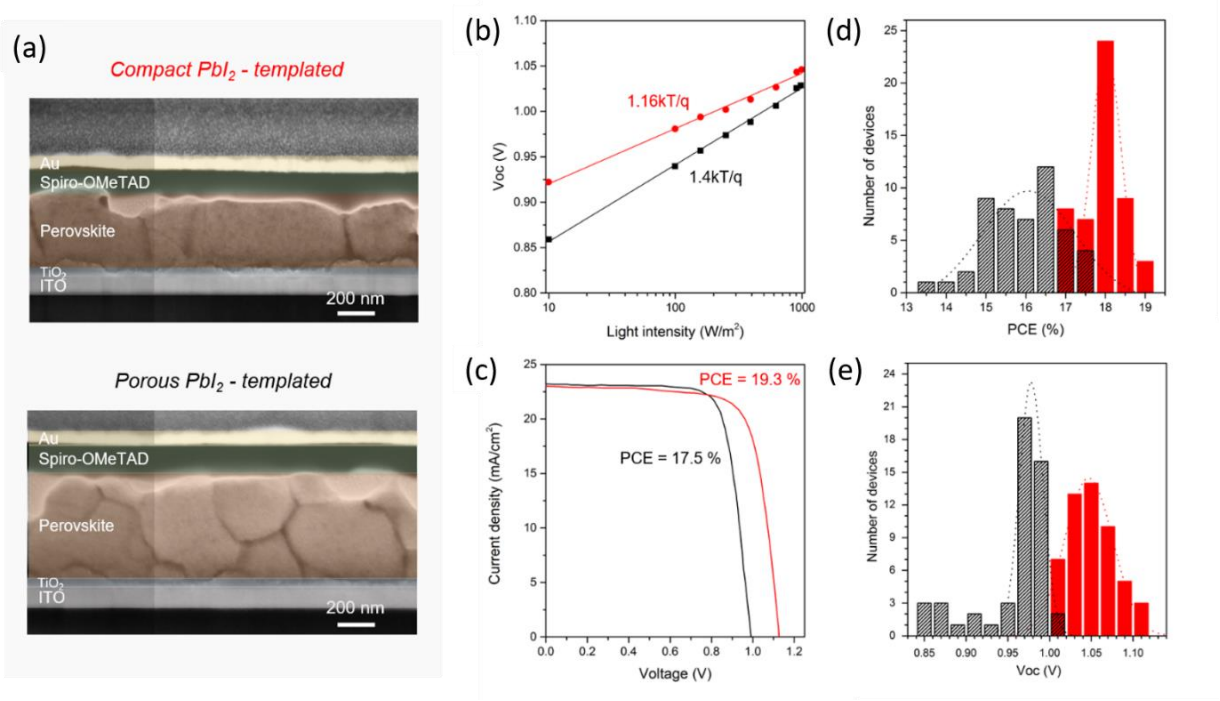

Figure 3.6. Structure and photovoltaic properties of solar cells based on perovskites fabricated with the compact PbI_2-templated and porous PbI_2- templated growth approaches. (a) Cross-section SEM images of selected solar cells produced by each approach. With the compact PbI_2-templated growth approach, the perovskite consists of microcrystals, with lateral dimensions beyond 1 μm. The crystal height is only limited by the layer thickness. With porous PbI_2-templated growth, the grains show smaller lateral dimensions (a few hundreds of nm). Furthermore, their height is smaller than the layer thickness, the layer consisting of a stack of crystals separated by transverse grain boundaries. The white contrasts at the top interface of the perovskite layer stand for a thin and discontinuous PbI_2 self-passivation coating formed during the perovskite annealing. The absence of white contrast elsewhere in the perovskite layer supports the absence of unreacted PbI_2. This suggests that the PbI_2 signal in the XRD pattern of **Figure 3.1** (b) originates only from the self-passivation at the top interface. (b) Light-intensity dependence of the V_{oc} of selected cells of both kinds, showing the relevant contribution of a trap-assisted recombination mechanism. This mechanism has a weaker impact for the compact PbI_2-templated perovskite, yielding a higher V_{oc} at all light intensities. (c) J−V curves of the best cells of each kind, showing a higher V_{oc} and PCE for the compact PbI_2-templated cell. (d) V_{oc} distribution and (e) PCE distribution measured for series of cells of the two types (compact PbI_2-templated and porous PbI_2-templated).

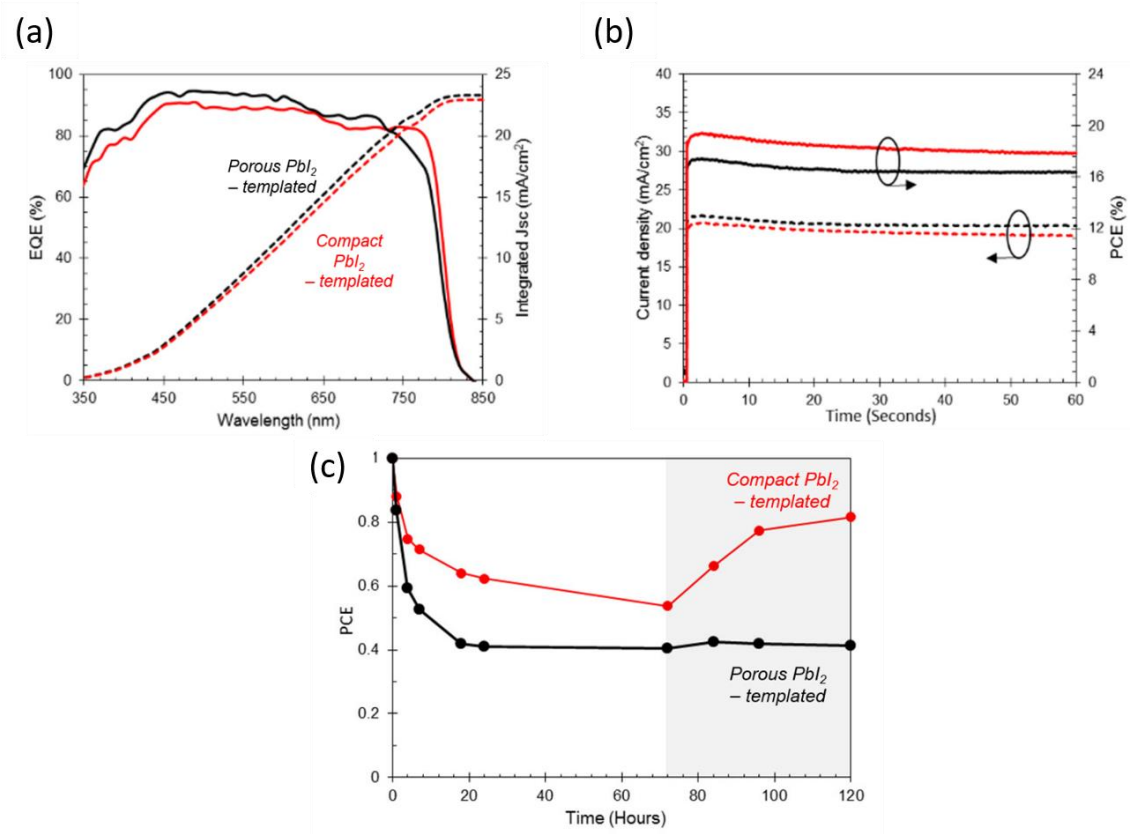

Figure 3.7 (a) EQE spectra of the best cells of each kind and corresponding integrated J_{sc}. (b) Steady-state measurements of the PCE and J_{sc} for both cells. Both J_{sc} and PCE increase to their maximum value in a few seconds, and then decrease slowly to reach a slightly smaller stabilised value after 60 s. After stabilisation, the compact PbI_2 – templated perovskite cell keeps showing a better performance than the porous PbI_2 – templated one. (c) Normalised PCE under constant 1 sun irradiation (white background) and when left in the dark in N_2 glovebox (grey background).

3.7 Discussion of recombination mechanisms in compact PbI_2-templated and porous PbI_2-templated cells

Several recombination channels are responsible for the reduction in V_{oc}, which remains, even for the best perovskite solar cells, significantly lower than the ideal one. Among these channels, the importance of nonradiative recombination, especially at interfaces, has been underlined. Here, we may assume that the main difference seen in V_{oc} between the compact PbI_2-templated and porous PbI_2-templated cells of the current thesis has its origin at the crystal interfaces within the bulk of the perovskite layer. For the larger crystals in the compact PbI_2-templated cells, the total interface area is reduced and consequently the number of surface

charge trapping states is reduced, too. The rest of the recombination channels should be similar for both types of cells, as similar compositions for the preparation of the active layer and the same charge transporting layers were used. As shown in Appendix B.5, the interface trap recombination current density can be directly compared with the current densities linked to direct recombination, either radiative, or nonradiative. Then, given that the band gap of both types of perovskites, and thus the ideal V_{oc}'s of the corresponding cells, are similar as discussed above, one may predict that the difference in V_{oc} between both cells should be proportional to the natural logarithm of the external fluorescence quantum yields ratio:

$$\delta V_{oc} = V_{oc}^{compact} - V_{oc}^{porous} = \frac{kT}{q} \ln\left(\frac{f^{compact}}{f^{porous}}\right) \quad (3.1)$$

where k is the Boltzmann constant, q the electrical charge, T the cell temperature, V_{oc} compact and V_{oc} porous correspond to the open-circuit voltages for the compact PbI_2-templated and porous PbI_2-templated cells, respectively, while $f^{compact}$ and f^{porous} are the external fluorescence quantum yields of the compact PbI_2-templated and porous PbI_2-templated cells, respectively. At 1 sun, the external fluorescence quantum yield ratio is taken equal to 5, as extracted from **Figure 3.5** (b). Then, using **Eq. (3.1)** we may determine that the δV_{oc} would amount to 40 mV, which falls within one standard deviation of the difference between the most probable measured V_{oc} values (70 mV ± 50 mV), as can be seen in **Figure 3.6** (d). One should note that, in general, there is a large dispersion in the reported V_{oc}'s from cells fabricated under the same exact conditions, and that higher V_{oc}'s than the one measured for the compact PbI_2-templated cells have been reported in the past. However, what is relevant is that the δV_{oc} we measured amounting to 70 mV corresponds to the difference in the most probable values for the open-circuit voltages from two types of cells fabricated in similar conditions but with a controllable and well-defined difference in the size of the crystals. This is a confirmation that the compact PbI_2-templated growth path we followed leads to a significant and clearly measurable increase in V_{oc} that can be directly linked to a measured increase in the external fluorescence quantum yield. Such increases are enabled by the larger crystal size that reduces the interface area and thus the density of interface nonradiative recombination pathways. Using **Eq. (3.1)** again, it is estimated that the highest V_{oc} achieved in this thesis is V_{oc} = 1.13 V and lags only 80 mV below the ideal, radiative limit value that corresponds to a 100% external fluorescence quantum yield for the perovskite crystals. This highest achieved V_{oc} value is equivalent to 93% of the ideal one. The trends found for FF and J_{sc}, shown in **Table 3.1**, are

consistent with theoretical expectations. Theoretical works by Pazos-Outon at. al. and Minemoto et. al. that quantified the dependence of V_{oc}, FF, and J_{sc} on trap density in perovskite solar cells indeed show that at the relatively low trap densities of the perovskites we fabricated, a decrease in trap density induces a smaller relative increase in FF than in V_{oc} and has no sizeable effect on J_{sc}. Changing the trap density has a smaller effect on FF because, at the maximum power point, the photocarrier density in the perovskite is small so that traps are in excess. This excess remains upon decreasing trap density, so that photocarrier concentration in the perovskite and thus the outgoing current experience a small increase only. Changing the trap density has no sizeable effect on J_{sc} because, at short-circuit, the internal electric field of the solar cell overcomes by far the coulombic field of the traps. Therefore, photocarriers do almost not interact with traps, so that decreasing trap density has no effect on charge extraction.

3.8 Conclusion

Summarising, in this chapter we report the development of a solution-processed fabrication approach based on the two-step method to produce, in a well-controllable way, $FA_{0.8}MA_{0.2}PbI_3$ perovskite layers with high-quality crystals larger than 1 μm. By using a compact PbI_2 layer as a template for the infiltration of the organic precursor, the limitations on the final perovskite crystal size intrinsic to the standard porous PbI_2-templated growth approach are overcome. We have shown that specific conditions, including the use of a highly concentrated organic precursor solution, Cl^- addition, and a post-spin-coating solvent annealing must be combined to enable the efficient incorporation of the large FA^+ cation into the PbI_2 lattice, a full PbI_2-to-perovskite conversion, and an efficient crystal growth. Note that such an approach can also be applied to fabricate high-quality perovskites with other compositions, for instance the triple cation ones. Owing to the efficient incorporation of FA^+ ions, the fabricated crystals present a smaller band gap than the $MAPbI_3$ perovskite. They show no trace of any inactive wide band gap hexagonal phase. In relation to its larger crystal size than the porous PbI_2-templated perovskite, the compact PbI_2 templated perovskite shows a higher external fluorescence quantum yield. It is near 4% under 1-sun equivalent illumination and near 20% at saturation under 70-sun equivalent illumination. Such more intense fluorescence reveals a higher contribution of radiative recombination, that is, a lower nonradiative recombination. Our results point to the importance of minimising nonradiative recombination of the defects at the interfaces within the active layer of perovskite solar cells. This enables obtaining a high fluorescence quantum yield that correlates with a high V_{oc}. The most natural and direct

approach to reach the radiative limit, and ultimately the Shockley−Queisser optimum consists in growing large crystals with the suitable composition, followed by an interface passivation. In this aspect, the compact PbI_2-templated growth approach we have used is particularly relevant. It opens the way to increasing in a well-controllable way the perovskite crystal size over 1 μm, together with incorporating large FA^+ cations. This enables at the same time bringing V_{oc} toward its radiative limit value and decreasing the band gap below that of the $MAPbI_3$ perovskites, thus improving the absorption of near-infrared photons and increasing J_{sc}. The achieved V_{oc} reaches 93% of the radiative value. This corresponds to a V_{oc} loss, the loss with respect to the electron charge times the band gap of the perovskite, or $qE_g - V_{oc}$, of 0.40 V, which, as shown in **Figure 3.8**, is one of the lowest reported for hybrid lead-halide perovskites.

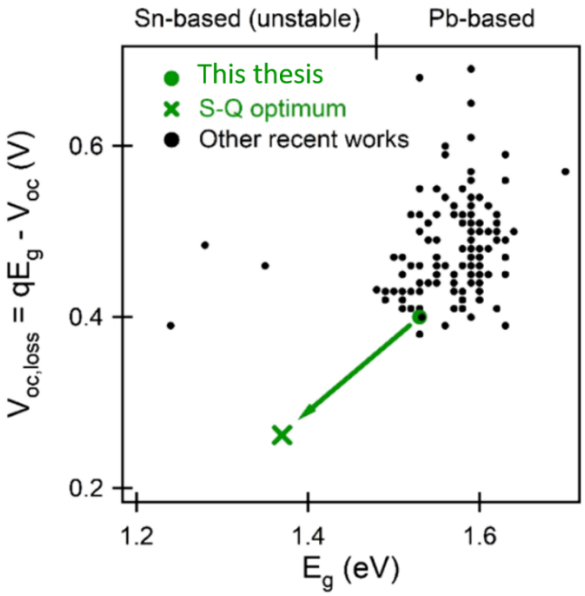

Figure 3.8 $V_{oc,loss}$ vs E_g for the best cell reported in this thesis (green circle), compared with the values of cells found in the most recent state-of-the-art literature (black dots). The Shockley−Queisser optimum (E_g = 1.35 eV and $V_{oc} = V_{oc,rad}$) is shown as a green cross.

Remarkably, such low V_{oc} loss is achieved with a perovskite with a low band gap of 1.53 eV. Therefore, the best device we fabricated is among the closest to the Shockley−Queisser optimum. In this aspect, its performance is comparable with that of the best devices fabricated by two-step approaches. Such highly fluorescent perovskite cells provide a possibility for further V_{oc} enhancement using optical strategies which will be discussed in the next two chapters.

Chapter 4

Optical management for achieving ultimate efficiencies in planar geometry perovskite solar cells

4.1 Introduction

In Chapter 2 and 3 we considered how the V_{oc} of a given perovskite solar cell is affected when the PLQY is increased by modifying material parameters or the morphology of the perovskite layer. In Chapter 3 we have seen that in certain cell configurations it is possible to approach the V_{oc} radiative limit by increasing the PLQY but, we have also seen in Chapter 2 that such material or cell configuration changes may also have a detrimental effect that may counterbalance the V_{oc} increase obtained by increasing the PLQY. In this chapter and Chapter 5 we will take a completely different approach to increase V_{oc} based on taking advantage of an already existing PLQY which we will not alter by any change in the materials or morphology of the different solar cell layers. As noted in Chapter 1, the radiative limit for the V_{oc} set by S-Q can be surpassed if one finds a path to reduce, what have been described in Chapter 1 as Boltzmann losses. In this chapter, we will use the modified S-Q model developed in Chapter 2 to find a multilayer structure that, given a PLQY, may enhance reflectivity for the emitted photons without dramatically affecting the transmission of incident solar photons. The model from Chapter 2 is modified by implementing a genetic algorithm-assisted inverse integration approach, which optimises all photovoltaic parameters to maximise the PCE of a perovskite solar cell when a dielectric multilayer (DM) is placed on top of the perovskite cells to properly manage the incident and the emitted photons. The approach we followed takes into account realistic solar cell configurations and optical properties of materials.

4.2 Concept and model

In this chapter, we study inverted (p-i-n) perovskite solar cells with a structure as the one depicted in **Figure 4.1** (a). Such a configuration allows the use of thin with low absorption hole and electron transporting layers, HTL and ETL, respectively. In this thesis such layers are named as parasitic as they do not contribute to the current produced by the solar cell, as discussed in Chapter 2.

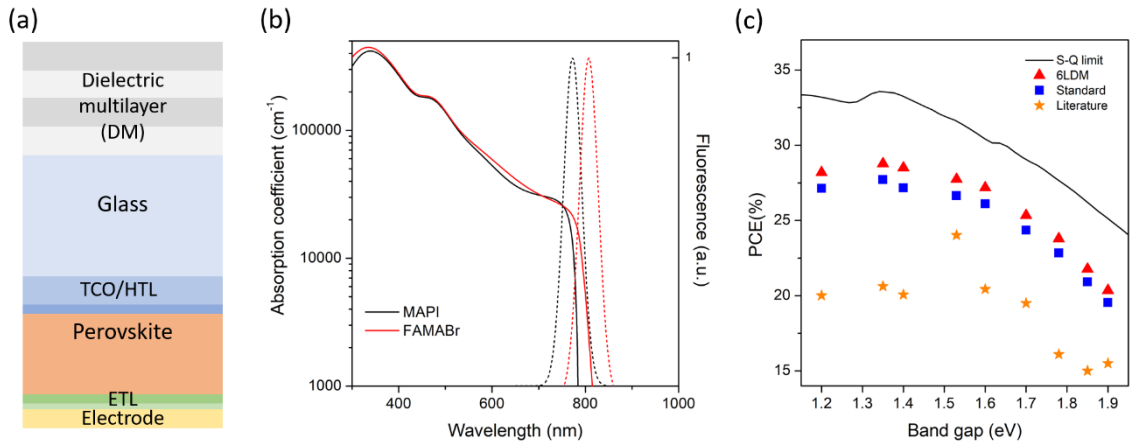

Figure 4.1. (a) Solar cell configuration,. (b) Experimental absorption coefficient and fluorescence of $FA_{0.8}MA_{0.2}PbI_{3-x}Br_x$ and $MAPbI_3$ perovskite films fabricated in our lab. (c) Power conversion efficiency as a function of the band gap. Shockley-Queisser limit discussed in Chapter 1 is represented by a black solid line, standard solar cells without a DM - blue squares, and with a 6-layer DM (6LDM) - red triangles. Experimental maximum efficiency reported for state-of-the-art perovskite solar cells is represented by orange stars taken from **Ref. 126 -130.**

As indicated in Chapter 1, the PCE of a single junction solar cell is a product of the short-circuit current J_{sc}, the open circuit voltage V_{oc}, and the fill factor FF. From the S-Q model outlined in Chapter 1, J_{sc} can be computed as the photogenerated current at open circuit conditions. The expression for it is given in **Eq. (1.2)**. The $V_{oc,rad}$ is proportional to the ratio of J_{ph} and J_0, which is the "dark saturation current" or the diode leakage current density in the absence of light, as shown in **Eq. (1.10)**.

Unlike in the S-Q model, in this thesis we consider an angular-dependent absorption, so the expression for V_{oc} in the radiative limit given in **Eq. (1.10)** becomes:

$$V_{oc,rad} = \frac{kT}{q}\ln\left(\frac{\Omega\int_0^{Eg} A(E,0)S(E)dE}{\int_0^{\pi/2}\int_0^{Eg} A(E,\theta)B(E)d\theta dE}\right), \quad (4.1)$$

From **Eq. (4.1)** it follows that achieving the maximum PCE requires a high J_{sc} and a low J_0.

To obtain a low J_0 without sacrificing J_{sc}, light reflectivity should be very small at or close to normal incidence while away from normal incidence, to enhance photon recycling or reduce Boltzmann losses, such reflectivity should be increased for wavelengths within the emission bandwidth of the perovskite material. For this purpose, as can be seen in **Figure 4.1** (a) we consider the use of a dielectric multilayer which may modify the reflectance of our solar cell in a way that J_{sc} is enhanced while J_0 is reduced.

To determine the structure of the DM that yields an optimal performance, we implemented an inverse integration approach based on a genetic algorithm targeting a maximum absorptance $A(E, \theta)$ of incoming light combined with a reduction of the emitted radiation coupling to the available modes. As seen from **Figure 4.1** (b) the absorption coefficient overlaps with the fluorescence peak, indicating a partial reabsorption of the emitted light, which enables the emitted photons to be trapped by a DM and contribute to the J_{sc}.

The solar cell parameters were calculated using the full wave generalised detailed balance model based on the transfer matrix method for s and p polarisations for normal and oblique light incidence outlined in Chapter 2. Details on the genetic algorithm and the optimisation routine followed in the current chapter are provided in Appendix C.1. The expressions obtained for the integrated electric field components are given in Appendix C.2. The optical constants used in this thesis were either obtained by ellipsometry measurements or from the literature (Appendix C.3). Optimisation was performed in terms of the refractive index (n), the thickness, and the number of layers in the dielectric multilayer while the studied solar cell configuration remained unchanged. The solar cells consist of a thick glass substrate, ITO as TCO, PTAA as HTL, perovskite active layer, Buckminsterfullerene (C60) and Bathocuproine (BCP) as ETLs and Au as electrode with thicknesses of 1mm/100nm/30nm/1000nm/100nm/2nm/80nm. Several rounds of optimisation were performed for all studied DM configurations, while DMs with a few layers required fewer rounds to converge, optimisation of DM with more layers required up to 15 rounds as depicted in **Figure 4.2**.

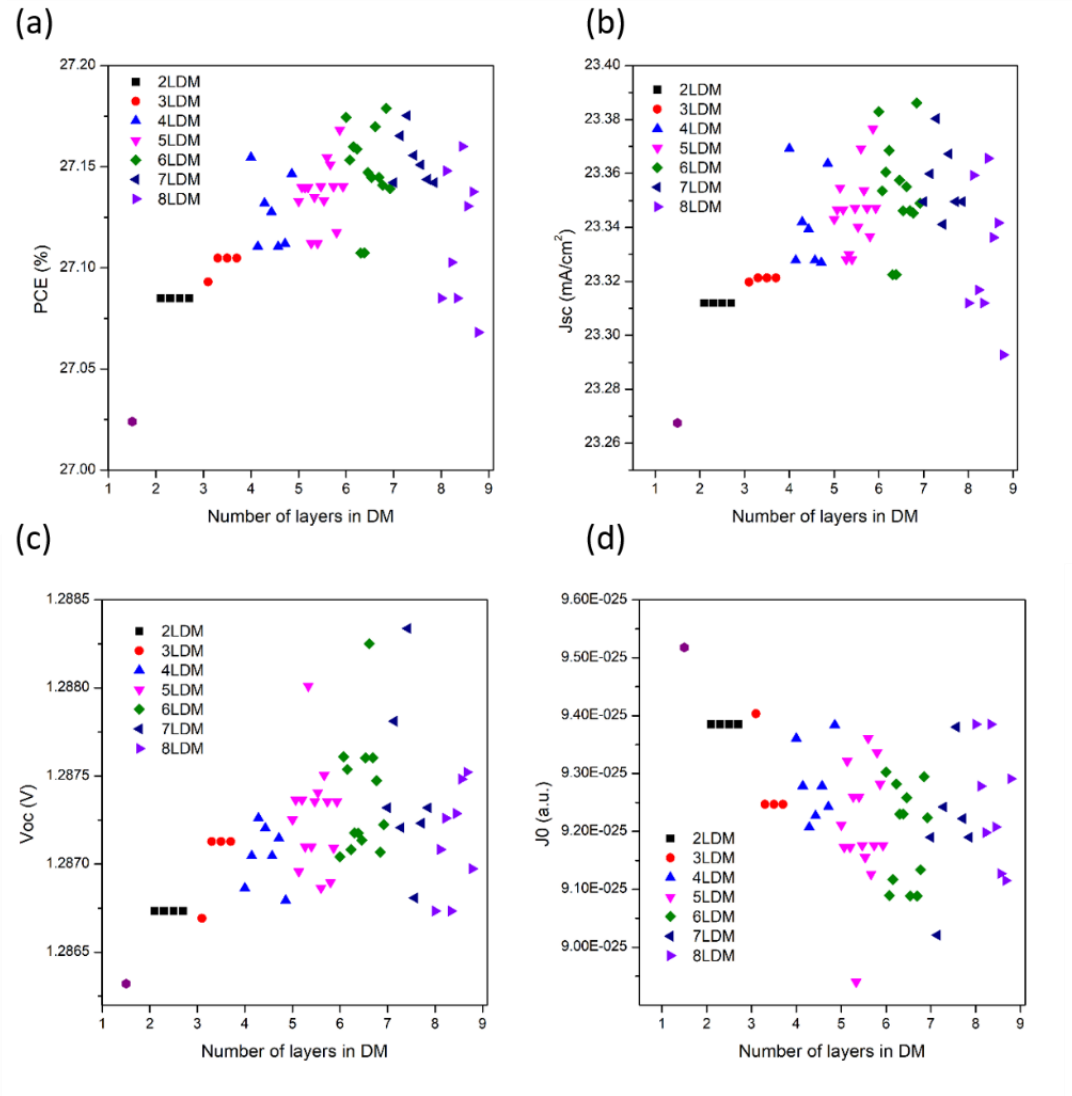

Figure 4.2 The set of simulated photovoltaic parameters for 1.6 eV perovskite based solar cells obtained during the optimisation process of DMs with different number of layers: (a) PCE, (b) J_{sc}, (c) V_{oc}, (d) J_0.

The performance resulting from the incorporation of the DM structure for several cells with a bandgap in the 1.2-1.9 eV range is compared in **Figure 4.1** (c) to cells without such a structure and to the S-Q limit efficiency. Standard cells that do not include any kind of optical structure in front exhibit an average of a 17.7% drop in performance relative to the S-Q limit efficiency. Note that such a drop can be partially mitigated to 14.4% on average with the incorporation of the DM structure.

4.3 The results of numerical simulations and optimisation for 1.53 eV and 1.6 eV perovskite-based solar cells

To further elucidate the competing role among sun photon absorption by the perovskite layer and the capacity for the cell structure to prevent emission in a broad angular range when different DM structures are being considered, we analyse in detail the performance of the 1.53 eV and 1.6 eV bandgap perovskite cells.

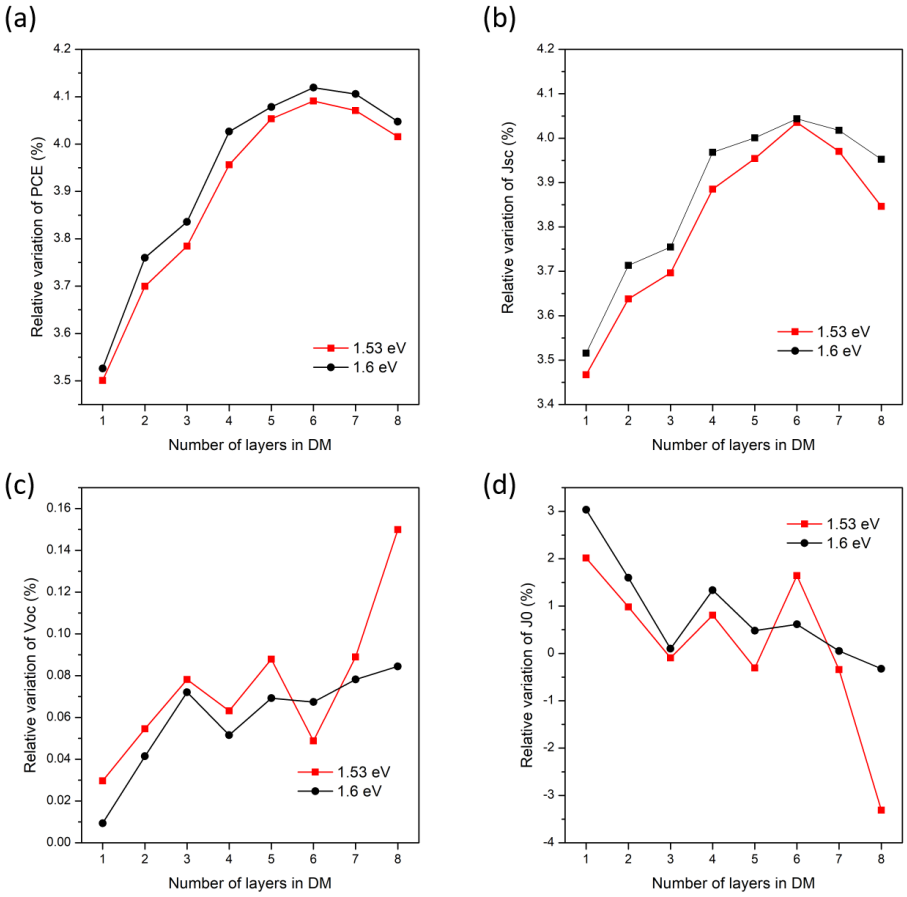

Figure 4.3. Relative variation of (a) Power conversion efficiency, (b) short circuit current, (c) open-circuit voltage and (d) dark saturation current as a function of number of layers in the DM for $FA_{0.8}MA_{0.2}PbI_{3-x}Br_x$ (red) and $MAPbI_3$ (black) based solar cells.

We focused the study on these two perovskites because the solar cells based on perovskites with similar band gaps exhibited the highest experimentally reported PCE, and their optical constants were accurately determined by ellipsometry measurements in our laboratory. Assuming a purely radiative perovskite layer with a PLQY equal to 1, and applying the inverse integration approach targeting a maximum PCE described above, we computed the PV parameters and PCE for cells incorporating from one up to eight-layer DMs. The absolute gain

in PCE achieved for 1.53 eV perovskite solar cell varies from 0.93% to 1.14% depending on the number of layers in the DM. The V_{oc} gain is 1.1 mV and the J_{sc} absolute gain is 1.01 mA/cm^2. For the 1.6 eV perovskite solar cells, the absolute gains are: PCE gain = 1.07 %. V_{oc} gain = 0.9 mV and J_{sc} gain = 1.2 mA/cm^2. The FF is not optically affected.

As can be seen in **Figure 4.3**, PCE and J_{sc} increase significantly for both perovskite solar cell and all DMs. For both perovskite solar cells, the gain in PCE increases with the number of layers in the DM, reaching its highest value of ~4.1% with a 6LDM. The parameters of obtained DMs and corresponding photovoltaic parameters of the solar cells are given in Appendix C.4.1 and C.4.2. For the 1.53 eV bandgap, the J_{sc} follows a similar trend, but with a more prominent increase for the 6LDM. On the other hand, the V_{oc} and J_0 exhibit a more complicated relation to the number of layers in the DM. Notably, except for the 1-layer and 8-layer DM, which escape form the general trend, when compared to its neighbour structures, the DMs with an even number of layers provide relatively lower V_{oc}, while the DMs with an odd number of layers exhibit relatively higher values. The J_0 follows a trend opposite to V_{oc}, being, when compared to its neighbour DM structures, relatively lower for an odd number of layers in the DM and relatively higher for DMs with an even number of layers. Such a correlation between V_{oc} and J_0 is in correspondence with **Eq. (4.1)** which indicates that a maximum performance of the cell would require the highest J_{sc} and lowest J_0 possible. For the 1.53 eV bandgap, when compared to its neighbour 5-layer and 7-layer DM structure cells, the 6LDM provides a J_{sc} with its maximum relative gain while the relative V_{oc} decrease is significant. However, for the 1.6 eV bandgap, when compared to its neighbour 5-layer and 7-layer DM structure cells, the 6LDM provides a relatively lower increase in J_{sc} and a relatively lower decrease in V_{oc}. This latter result indicates that the DM design must be such that, both, J_{sc} enhancement as well as J_o reduction have to be adequately balanced to achieve the ultimate cell efficiency.

4.4 The optical properties of dielectric multilayers and their effect on performance of solar cells

As indicated above, the purpose of DM is to enhance J_{sc} and reduce J_0, which can be achieved if the reflectance of the solar cell is decreased at normal incidence but increased for oblique incidence. In other words, the DM must be designed in such a way that an antireflection character is exhibited for a broad wavelength range at normal incidence and a high reflectivity is exhibited within the perovskite fluorescence band at oblique incidences. Such a fluorescence

band is centred at 802 nm and 772 for the 1.53 eV and 1.6 eV perovskite solar cells, respectively. As can be seen from **Figure 4.4** (a) and (b), the reflectivity of the 6LDM clearly fulfils such a double role provided the lowest reflectivity at normal incidence is followed by a rapid increase in reflectivity as the incidence angle increases. Such a latter increase is less apparent for the 1.53 eV perovskite solar cell than for the 1.6 eV perovskite solar cell, in agreement with the lower V_{oc} enhancement provided by the 6LDM for the 1.53 eV perovskite solar cell. For the 1.6 eV perovskite solar cell, the reflectivity at large angles is similar to the one from the neighbour DM structure cells, in agreement with the relatively low V_{oc} loss observed in **Figure 4.3** (c) for the 6LDM cells. As can be seen in **Figure 4.4** (c) and (d), within the gap and away from the fluorescence band, all DMs, except for the 1- and 8- layer, provide a very low reflectivity at normal incidence. The reflectivity of DM with number of layers from 2 to 4 are provided in Appendix C.4.3. In other words, the inverse design with variable thickness and refractive index for all layers allows for the design of DMs that provide the adequate angular reflectivity within and outside of the fluorescence band. The 1 and 8-layer DMs escape from that behaviour, provided they fail in simultaneously increasing and decreasing reflectivity, at large and small angles, respectively. The 8-layer provides the highest reflectivity at oblique incidence., but severely compromising a low reflectivity at normal incidence, resulting in the lowest J_o and the highest V_{oc} but a far from optimal J_{sc}. In summary, for both bandgaps the optimal DMs are achieved when the number of layers ranges from 5 to 7. In such cases, reflectivity at oblique incidence is maximised without sacrificing the antireflection character of the DM at normal incidence. This stresses the relevance of designing DMs that simultaneously consider J_{sc} and V_{oc} optimisation.

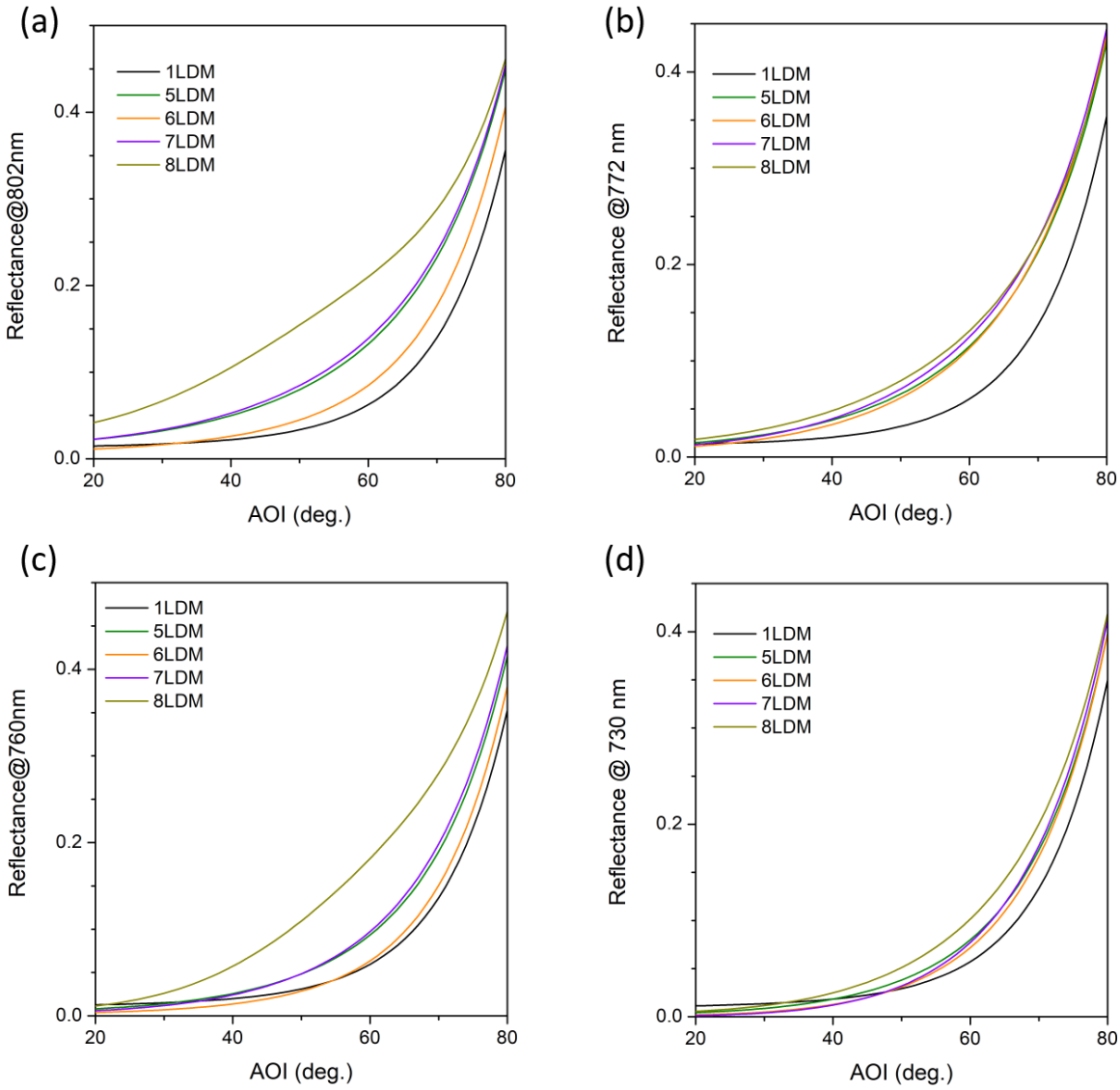

Figure 4.4. Total reflectance of DMs on glass for 1.53 eV and 1.6 eV perovskite solar cells at (a) 802 nm and (b) at 772 nm (PL peaks, respectively) and at (c) 730 nm and (d) 760 nm as a function of angle of incidence for all studied DM configurations.

To emphasise the importance of wavelength selectivity, not only angular selectivity, of the DM, we analyse its effect on different compositions of perovskites covered in this thesis. For this purpose, we optimised a 6LDM for solar cells with different perovskite active layers taken from the literature. The parameters of all optimised DMs are given in Appendix C.4.1.

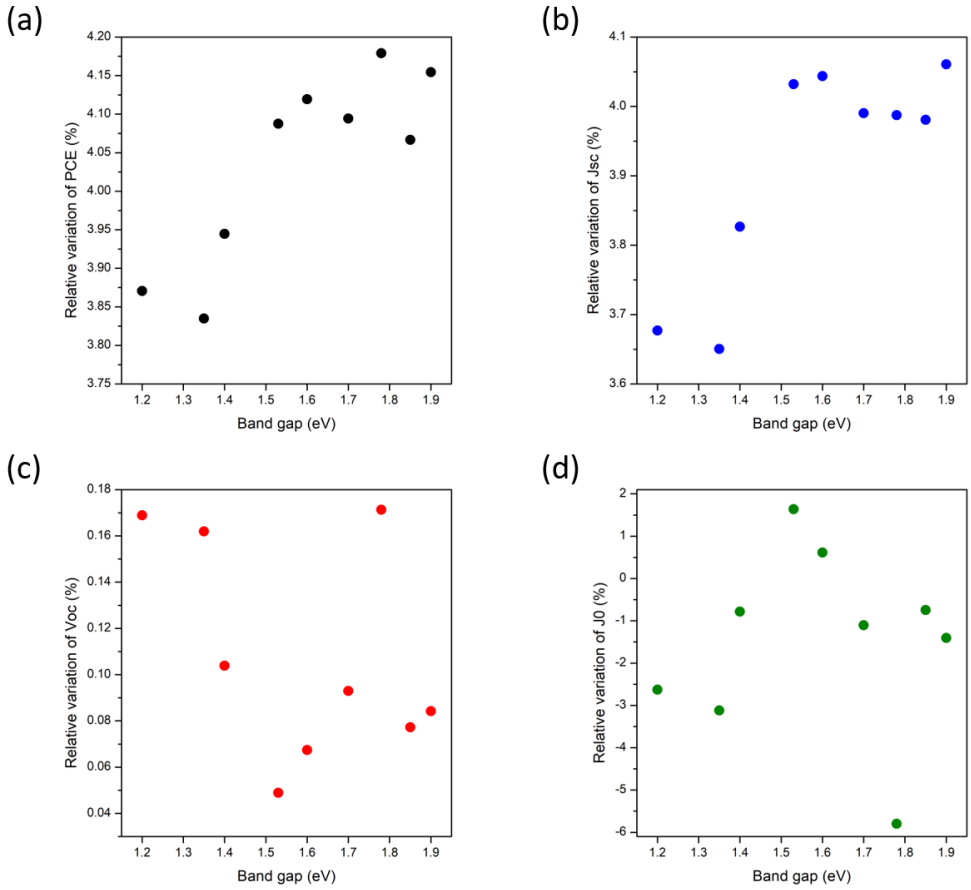

Figure 4.5 Relative gain of photovoltaic parameters of PCS based on different perovskite compositions (a) PCE, (b) J_{sc}, (c) V_{oc} , (d) J_0.

As can be seen from **Figure 4.5** (a), the relative gain in PCE increases, with the band gap of perovskite active layer, being the highest gain of 4.17% for 1.78 eV perovskite solar cell and the lowest of 3.83% for 1.35 eV perovskite solar cell. The absolute gain of PCE varies from 0.81% for 1.9 eV perovskite to 1.09% for 1.53 eV perovskite solar cells. The highest absolute V_{oc} gain is 2.6 mV corresponding to 1.78 eV and the lowest is 0.6 mV corresponding to 1.53 eV perovskite solar cell. The highest J_{sc} absolute gain is 1.18 mA/cm^2 for 1.2 eV perovskite solar cell and a lowest is obtained for 1.9 eV perovskite solar cell being 0.51 mA/cm^2. This shows an opposite trend to relative gain, as values of photovoltaic parameters significantly vary depending on the band gap of the perovskite. Putting together results from **Figure 4.5** with the reflectance patterns depicted in **Figure 4.6** is seen that the most advantageous 6LDM provides relatively low reflectance at normal incidence and high reflectance at oblique incidence. The absolute values of all photovoltaic parameters are provided in Appendix C.4.2.

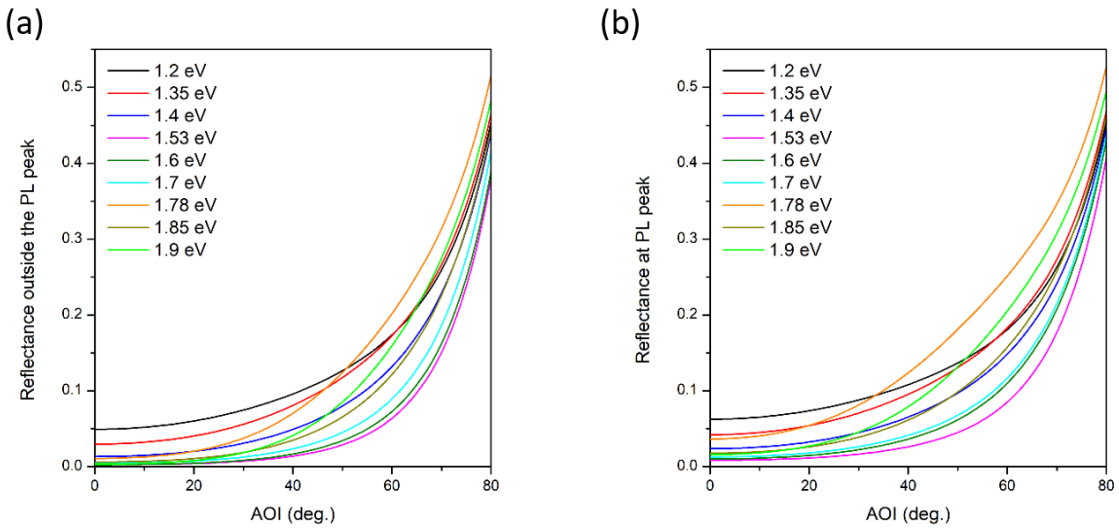

Figure 4.6 Reflectance of DMs on glass (a) outside the PL peak and (b) at PL peak as a function of angle of incidence for all studied perovskite compositions.

Non-optimal reflectance patterns are observed for narrow-bandgap perovskites, as the absorption spectra of such materials are wide and 6LDM cannot provide very low reflectance at normal incidence and strong reflectance at oblique. With the increase in band gap, the ability of 6LDMs to provide low reflectance at normal incidence improves, but the reflectance remains low at higher angles. When further increasing the band gap, the 6LDMs can provide the desired patterns with low reflectance at normal and high reflectance at oblique incidence. Looking in detail at the parameters of obtained 6LDMs, which are given in Appendix C.4.1, one notices that 6LDMs providing relatively low reflectance at the oblique incidence have a gradient-like refractive index distribution. This is clear for the 6LDMs optimised for 1.53 eV, 1.6 eV. It is known that a smooth index gradient provides low reflectance for a broad angular and wavelength region, as demonstrated by Miloud et. al. On the contrary, 6LDMs providing a rapid increase in reflectivity as the angle increases have a periodic-like structure, as seen in the case of 6LDMs optimised for 1.85 eV and 1.9 eV perovskites. The angular selectivity of such structure can be explained by fulfilment of the Bragg condition when one combines λ/4 layers of low and high index of refraction. The reflectance remains low for shorter wavelengths and increases for longer ones. Analysing the parameters of the DMs obtained, one sees that for high wavelengths there is a destructive interference for reflection, while for lower ones there is a constructive one. This applies to many of the DMs studied in this work. Moreover, all of the obtained 6LDMs have as a first layer a material with a low refractive index, acting similar to

the standard anti-reflection coating, while the remaining layers have a stronger influence on the wavelength and angle-dependent reflectivity patterns. The structure with non-optimal reflectance does not exhibit such a clear trend in the refractive index distribution and represents a mixed configuration. Even though the 6LDM optimised for 1.78 eV does not provide the lowest reflectance at normal incidence, the rapid increase in reflectance at oblique incidence provides the highest gain in PCE.

Fabrication of DM structures and perovskite cells to achieve the final goal of reducing Boltzmann losses while maintaining a high J_{sc} is discussed in the following chapter. In Chapter 5 we establish the path for such fabrication and implementation of the experimental 6LDM on 1.53 eV perovskite-based solar cells and consider its effect on the photovoltaic parameters of the fabricated devices.

Chapter 5

Fabricated multilayer structures to optically modify PV parameters in perovskite cells.

5.1 Introduction

To experimentally study the effect of the DMs considered in Chapter 4 on actual perovskite solar cells, in this chapter we carried out the optimisation of a 6LDM to be applied to $FA_{0.8}MA_{0.2}PbI_{3-x}Br_x$ cells. This material was chosen because the fabrication method and the stability of the corresponding solar cells has been extensively studied previously in our laboratory. Such perovskite solar cells exhibit a bandgap of 1.53 eV and the most fluorescent devices exhibit a PLQYs ranging from 5% to 19% depending on the illumination intensity. In this chapter we discuss the optimisation approach, the 6LDM fabrication method, as well as methods of fabrication of the perovskite cell. Experimental results including optical characterisation of the fabricated 6LDM, electro-optical characterisation of fabricated solar cells, and the effect of the 6LDM on these devices, are discussed.

5.2. Perovskite solar cells fabrication and characterisation

The solar cells used in this chapter have been fabricated by a two-step solution process which requires first the deposition of a PbI_2 layer with a subsequent deposition of an organic precursor. The details of the fabrication are described in Appendix D.1. The solar cell is composed of: glass substrate covered with ITO - transparent conductive oxide, layer of SnO_2 nanoparticles acting as an ELT, perovskite later, Spiro-OMeTAD as hole-transporting layers and an Au back contact. The photovoltaic parameters of the fabricated cells are shown in Appendix D.2. The fabricated solar cells provide an average PCE of 16.05%, and the corresponding average parameters being Jsc = 22.22 mA/cm2, Voc = 1.073 V, and FF = 67.3%. The parameters for the best solar cell in terms of power conversion efficiency were PCE = 18.22%, J_{sc} = 22.94 mA/cm^2, V_{oc} = 1.086 V and FF = 73.1%. The best solar cell in terms of open-circuit voltage exhibited a V_{oc} = 1.119 V and the best solar cell in terms of short circuit current exhibited a J_{sc} = 23.86 mA/cm^2.

The external quantum yield (PLQY) of solar cells has also been measured at different laser intensities. The PLQY was obtained as described in Chapter 2, using an integrated sphere and

continuous illumination at 532 nm. **Figure 5.1** depicts PLQY of a selection of solar cells with V_{oc} ranging from 0.84 V to 1.12 V and under laser illumination equivalent to 1 and 5 suns. Solar cells follow the behaviour similar to the cells from Chapter 2, i.e., the PLQY increases for the cells with higher open circuit voltage.

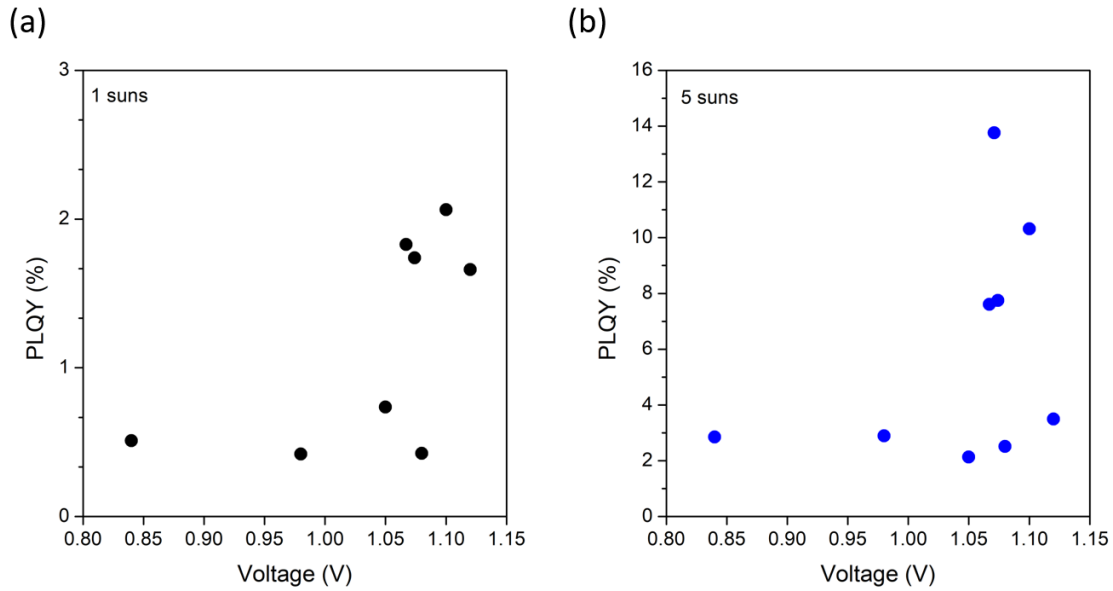

Figure 5.1 PLQY of solar cells with different V_{oc} values under (a) 1 and (b) 5 suns illumination.

In addition, the PLQY of the solar cells exhibits a saturation behaviour as the number of suns increases, as can be seen in **Figure 5.2**. The solar cells with relatively high PLQY at low illumination start to degrade under 50 suns illumination, while solar cells with relatively low PLQY at 1 sun reach a certain value which stays roughly constant when the number of suns is increased beyond 50. This indicates that there is a certain experimental error due to material inhomogeneities, which are inherent to solution processed perovskites solar cells.

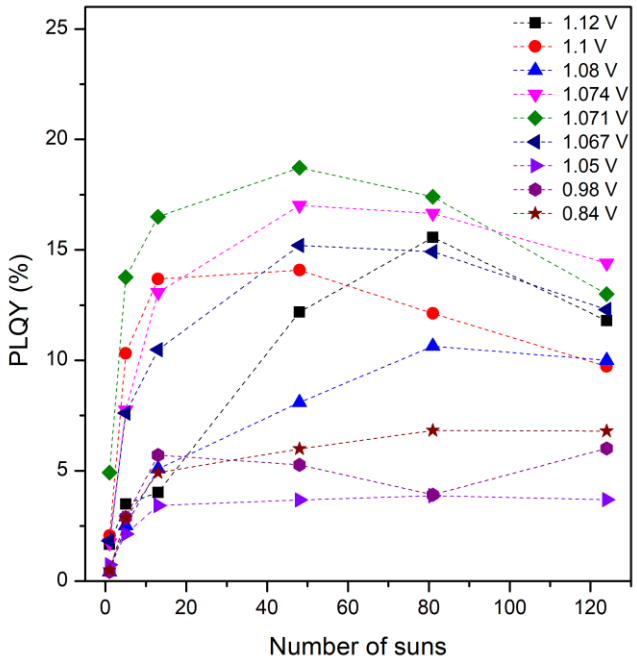

Figure 5.2 PLQY of the selection of perovskite-based solar cells as a function of illumination power, equivalent to number of suns.

5.3. Experimental 6LDM

The genetic algorithm-assisted inverse integration approach described in Chapter 4 has been used for the optimisation of the experimental 6LDM. The main difference from the approach followed in Chapter 4 is that the optical constants of the layers for the fabricated 6LDM were fixed input parameters. Herein we consider using materials which resemble those obtained from the theoretical 6LDMs considered in Chapter 4, but, that also correspond to the indexes of the actual materials we can use to fabricate such multilayers in our laboratory. Such materials are: MgF, TiO2 and ZnO. The optical constants of such materials are given in Appendix D.5. Provided the freedom in selecting the refractive index is lost when determining the optimal 6LDM structure, we considered different configurations for such 6LDMs, the alleged periodic and gradient structures as discussed in Chapter 4. The gradient structure corresponds to a gradient increase followed by a decrease in the refractive indexes of the layers composing the 6LDM, while the periodic is designed by alternating layers of low and high refractive index. As indicated in Chapter 4, several optimisation rounds have to be performed in order to find the best 6LDM structure. The optimal DM to simultaneously enhance V_{oc} and J_{sc} was found to

have a kind of periodic structure ($MgF/TiO_2/ZnO/TiO_2/ZnO/MgF$) with indexes and thicknesses given in **Figure 5.3**. When using such a 6LDM structure, the computational approach estimates that the PCE, J_{sc} and V_{oc} will simultaneously increase, exhibiting an absolute gain of 0.78 mA/cm^2 for J_{sc}, 2 mV for V_{oc} and 0.91% for PCE. The FF remains essentially unaffected by the 6LDM.

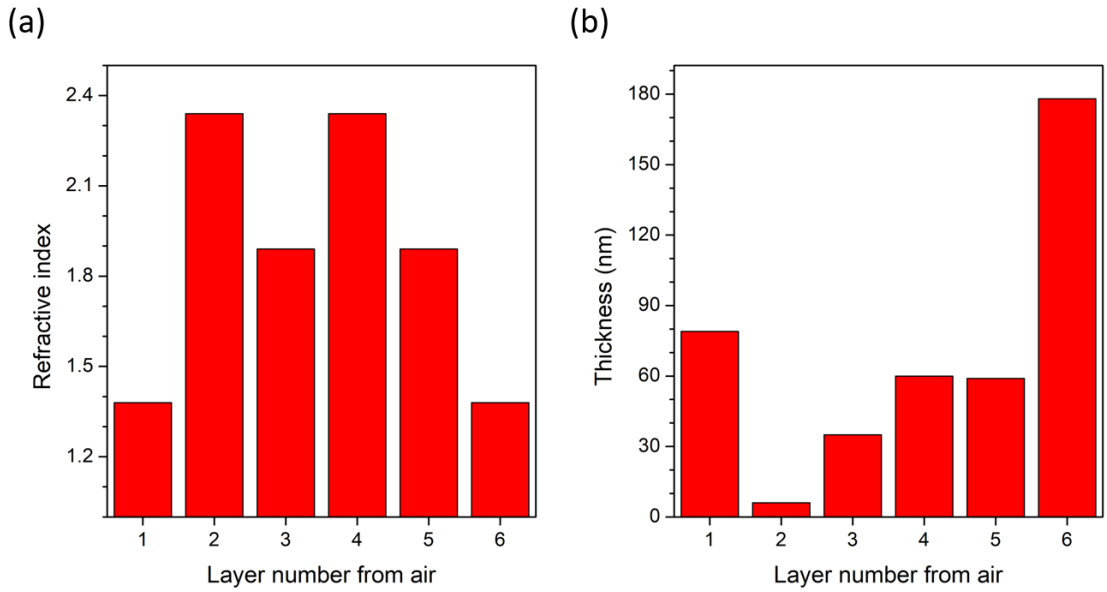

Figure 5.3 Configuration of a 6LDM multilayer (a) average refractive index of the layers, (b) corresponding thicknesses.

The MgF layers were fabricated by thermal evaporation in a high vacuum chamber, while the TiO_2 and ZnO layers were deposited employing reactive magnetron sputtering. The layers constituting the 6LDM were deposited on a thin glass substrate of 150 μm to minimise the distance from the solar cell. The transmittance of the fabricated 6LDM on glass was measured with a spectrophotometer for a broad wavelength range and at several angles of incidence, as the fabricated 6LDM is wavelength and angle selective.

In **Figure 5.4** one sees the comparison of experimental and theoretical transmittance for the fabricated 6LDM as a function of angle of incidence at 802 nm corresponding to the wavelength of the emission of the perovskite active layer and two wavelengths ± 30 nm away from the peak. The comparison of theoretical and experimental transmittance as a function of wavelength at different angles is shown in **Figure 5.5**. The transmittance is decreasing with the wavelength and the angle, but slightly differs from the theoretical curves. Such deviations could be explained by small differences in the thickness and optical constants of the deposited layers

and the substrate, which could not be controlled with sufficient precision during the fabrication processes.

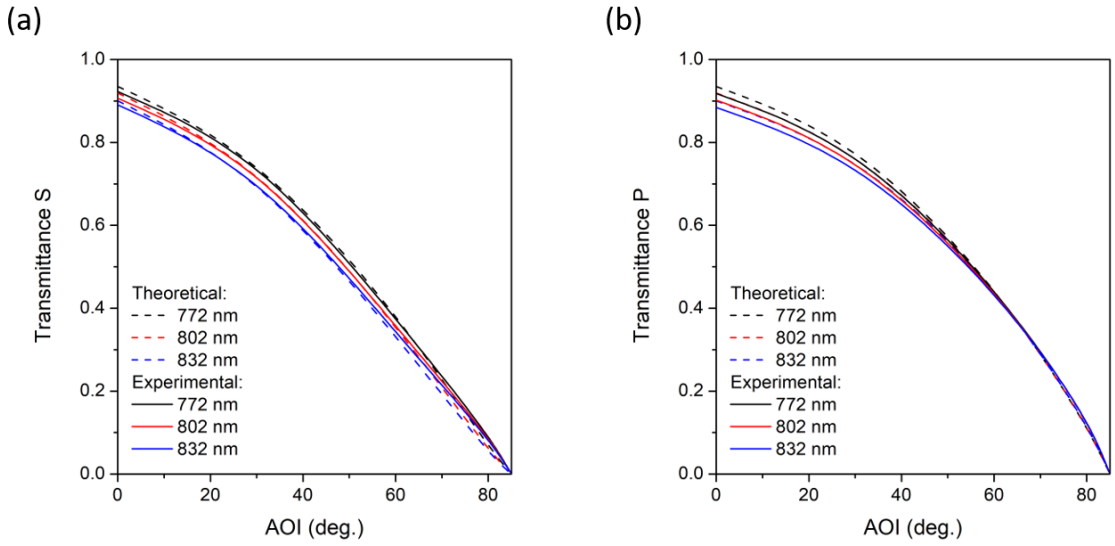

Figure 5.4 Transmittance as a function of the angle of incidence of a 6LDM on glass, theoretical and experimental values for (a) S and (b) P polarisations for wavelengths corresponding to emission peak of perovskite material (802 nm) and ± 30 nm.

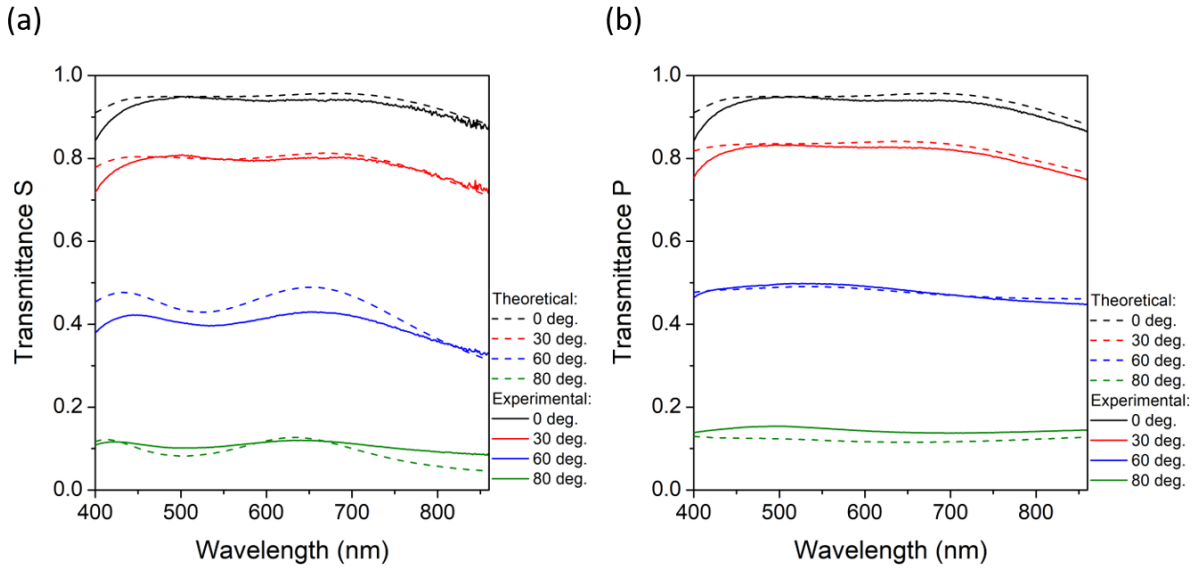

Figure 5.5 Transmittance as a function of wavelength of a 6LDM on glass, theoretical and experimental values for (a) S and (b) P polarisations for selected angles of incidence from 0 to 80 degrees.

As noted, the main goal of the 6LDM is to improve transmittance at normal incidence for a broad wavelength range while limiting the transmittance at the emission wavelength of the

perovskite. In comparison to the glass substrate, the transmittance is increased for the wavelength range from 450 nm to around 720 nm. Low transmittance in the UV range does not affect the performance of the device as the ITO layer has a strong absorption in UV region, hence those photons do not reach the active layer in a standard solar cell. It is clear from **Figure 5.5** that for longer wavelengths, 720 nm and above, the transmittance is decreased and decreases even further when the angle is increased. In both cases, for S and P polarisations, the behaviour of 6LDM is similar.

5.4 The results of the implementation of the 6LDM onto the solar cells

The several batches of the fabricated solar cells have been measured to study the effect of the 6LDM on the solar cells photovoltaic parameters. The 6LDM was attached to the solar cell from the glass substrate side using an index matching liquid. The measurement procedure was to first measure the solar cells without the 6LDM and then the 6LDM was attached and the cells were measured again. In between measurements, the cells were kept in the dark and remeasured again. To eliminate any change in performance arising from the PLQY saturation effects, such a measurement was repeated, by first measuring the cell performance with the 6LDM and after without the 6LDM. The results from such measurements are shown in Appendix D.6. The gain in the V_{oc} is nearly constant for each measurement and the corresponding device, the J_{sc} gain exhibits more variation as the method of attaching the 6LDM introduces some experimental errors and J_{sc} is more sensitive to it.

The measurements were performed under solar illumination and under laser illumination equivalent to 3 suns. As has been demonstrated before, the PLQY increases with the increase of illumination power, which suggests the light-induced trap passivation, hence, less non-radiative recombination. The wavelength of the laser was chosen to be 663 nm provided at this wavelength we see the highest increase in EQE, which is shown in **Figure 5.6**. From **Figure 5.6** one sees that the 6LDM prevents a part of the UV light from reaching the active material but improves absorption in the visible range and a changes the absorbance pattern for wavelengths longer than 720 nm. It is important to note that the absorption is slightly extended to near IR when the 6LDM is applied, suggesting the contribution of emitted photons to the EQE, in other words, slightly shifting the effective band gap of our devices.

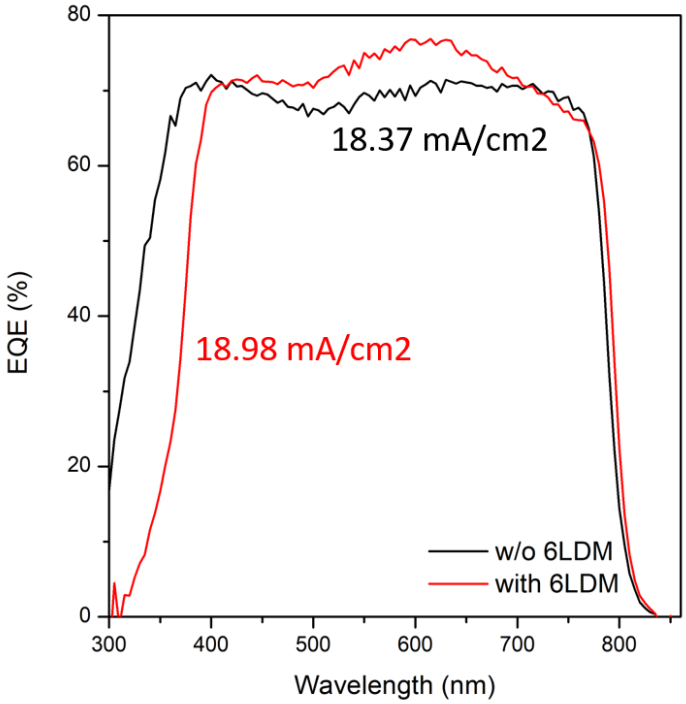

Figure 5.6 External quantum efficiency (EQE) of a perovskite-based solar cell without (black) and with (red) 6LDM.

Absolute variations of the measured photovoltaic parameters of a large batch of solar cells under solar illumination are shown in **Figure 5.7**. As was mentioned before, the J_{sc} is not increased for all the studied devices as an implementation of 6LDM requires putting an index matching liquid and depending on the amount of this liquid it introduces some absorption in the visible wavelength range. Despite these issues, most of the cells show an increase in the J_{sc}. In most cases the experimental gain appears to be lower than the theoretically predicted one, and partially can be explained by a slightly lower transmittance of the fabricated 6LDM. On the contrary, the V_{oc} increased for all the cells and such a gain is higher than the theoretically predicted one. Such a strong effect on V_{oc} cannot be explained alone by a lower transmittance of the fabricated 6LDM at the wavelengths of the emission of the perovskite.

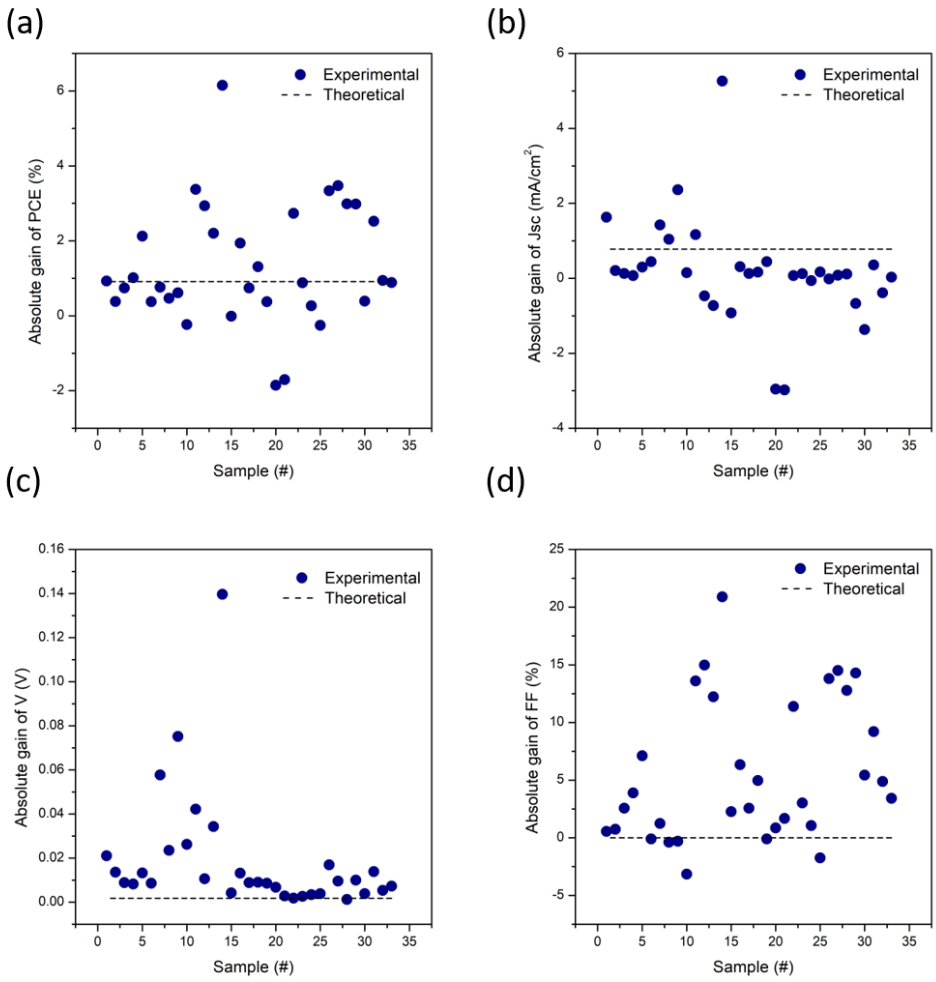

Figure 5.7 Absolute gain of photovoltaic parameters of perovskite based solar cells with 6LDM measured under solar simulator: (a) PCE, (b) J_{sc}, (c) V_{oc} and (d) FF. Theoretically predicted gain is depicted as a dashed line.

The results of photovoltaic measurements under laser illumination equivalent to 3 suns are shown in **Figure 5.8**. In comparison with parameters obtained under a solar simulator, which has a power of 1 sun, both, the J_{sc} and V_{oc} gains are higher under laser illumination. The increased gain in J_{sc} can be explained by illumination with a monochromatic light corresponding to a wavelength, which is the most affected by the 6LDM as depicted in **Figure 5.6.** The average V_{oc} gain is one order of magnitude higher in the case of laser 3-sun-equivalent illumination than under solar simulator illumination. This can be explained by lower defect density, hence lower non-radiative recombination, as was shown in PLQY measurements in **Figure 5.2**. In this case more photons can be reabsorbed and contribute to currents, which consequently affects the V_{oc} of the device. The experimental FF also appears to be affected by implementation of 6LDM. The decrease in FF can be partially explained by the experimental

set-up for the measurement under laser illumination, which has a damaging effect on the contacts. Hence, the resulting PCE gain is slightly lower than one obtained with the solar simulator.

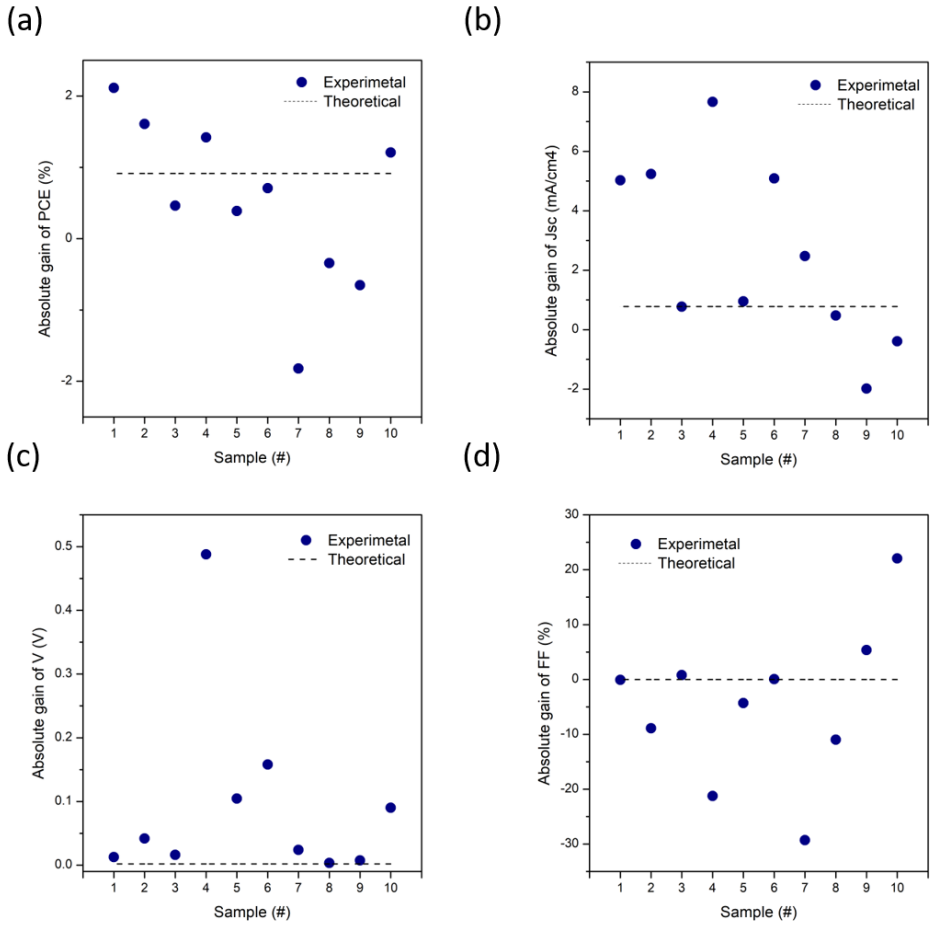

Figure 5.8 Absolute variation of photovoltaic parameters of perovskite based solar cells with 6LDM measured under continuous laser illumination corresponding to 3 suns: (a) PCE, (b) J_{sc}, (c) V_{oc} and (d) FF. Theoretically predicted gain is depicted as a dashed line.

5.5 Discussion and outlook

The 6LDM was fabricated and implemented onto perovskite solar cells and their photovoltaic parameters were measured under 1-sun equivalent solar simulator and 3-sun equivalent 633 nm laser radiation. Both experiments show the effect of 6LDM on J_{sc} and V_{oc}, but we cannot attribute it to the optical effect alone, predicted theoretically. On one hand, the lateral dimensions of the experimental solar cells are limited in comparison to the infinite lateral dimensions assumed in the theoretical calculations, which affect the light trapping capabilities, hence the J_{sc}. Most of the solar cells suffer from the J_{sc} reduction under 1 sun

illumination, but the better results are obtained under monochromatic illumination. Taking into account that the ratio of lateral to horizontal dimensions of experimental solar cells is different from simulations, some other optical effect may occur. Further experiments are required to bring the experimental solar cell closer to the theoretical configuration, including thinning down the substrate, merging the substrate with the 6LDM, and increasing the size of the solar cell itself. On the other hand, the obtained V_{oc} gain far exceeds the theoretical findings. The increased V_{oc} gain obtained during measurements under 3 sun illumination suggests that the optical effect is not the only one affecting the V_{oc}. As our optical structure changes the coupling and outcoupling of the light, this may lead to a photogenerated charges build-up at the interfaces, affecting the V_{oc}. Moreover, the increase in FF was also observed for the measured devices. While from the optical point of view the 6LDM should not affect the FF, the FF is known to be affected by charge accumulation and extraction processes. Hence, more experiments must be conducted to find the reason for such an increased gain in V_{oc} and the effect on FF. But that will require a comprehensive study of opto-electronic processes in the active material to decouple optical effect from intrinsic material processes.

There is yet not sufficient evidence supporting a reduction of the Boltzmann loss. However, the results obtained suggest that the initiated path should be followed to further shine light into the physics behind such an increase in the PV parameters obtained solely from an optical effect. Indeed, we have demonstrated that by changing the optical properties of the perovskite solar cell substrate, not only the J_{sc} can be enhanced but also the V_{oc}, which paves the path for further research on this topic.

Conclusions

With the current thesis we have provided a comprehensive study on the close links that exist between the V_{oc} of perovskite solar cells and the propagation, absorption and emission of photons within such devices. Departing from the S-Q detailed balance model in a framework that fully considers the layered configuration from perovskite solar cells, we determined how the V_{oc} depends on PLQY and established to what extent such V_{oc} can be limited by non-radiative recombination and fundamental losses, such as the Boltzmann one. To set the path to overcome such limitations on the V_{oc}, we have demonstrated, for the first time, the experimental relation between V_{oc} and PLQY in perovskite solar cells. Next, we developed a fabrication method for the perovskite layer in a solar cell where the reduced non-radiative recombination can be clearly linked to an increased PLQY and higher V_{oc} of the corresponding devices. To tackle the Boltzmann loss, we have proposed an optical structure which enhances the absorption of incoming photons while, at the same time, limits the escape cone for the emitted photons. Experimental implementation of such a structure resulted in V_{oc} increases, which for the first time proved that the V_{oc} of perovskite solar cells can be optically enhanced. In summary, the current thesis opens a path to a new generation of perovskite solar cells that may exhibit V_{oc}s approaching the radiative limit or even surpassing it, if the reduction of the Boltzmann loss can be experimentally confirmed.

In Chapter 2, we study the PLQYs of the perovskite solar cells and demonstrate the relation between PLQYs and V_{oc}s of perovskite-based devices. With some explainable deviation from the behaviour predicted by full-wave generalised detailed balance model, the V_{oc} increases with an increase of PLQYs. The factors limiting the V_{oc} were found to be parasitic absorption and energy barriers at the interfaces of buffer layers with the active material. Still, the PLQYs of the perovskite solar cells were rather low, which suggested that the perovskite material must be optimised, which was resolved in the next chapter.

The two-step "compact PbI_2-templated perovskite growth" method was developed to fabricate the thin perovskite films with large crystal sizes is described in Chapter 3. It is demonstrated that increase in the grain size, larger than 1 μm, increases the PLQYs of the films, indicating that reduction of number of boundaries in the film leads to the reduction of non-radiative recombination sites. The solar cell based on large crystal perovskite exhibits the improved stability of light illumination is observed and the V_{oc} reaching 93% of the radiative value, which is one of the lowest reported for hybrid lead-halide perovskites.

Chapter 4 is dedicated to the theoretical study of optical improvement of V_{oc} of the perovskite solar cells. The full-wave generalised detailed balance model is further developed to include an angle and wavelength selective dielectric multilayer on top of the substrate. The genetic algorithm was used to find the optimum configuration of the DM and a range of solar cells based on perovskite with different band gaps were studied. It is found that a simple 6-layer structure can simultaneously increase J_{sc}, V_{oc} and PCE of the device, by improving transmittance of the substrate for the wide spectrum of incoming light, at normal incidence, and limiting an escape cone of the emitted photons.

Finally, in Chapter 5 the DM was fabricated and optical enhancement of photovoltaic parameters has been demonstrated experimentally. The measured J_{sc} and V_{oc} gains exceeded the values predicted with the full-wave generalised detailed balance model, so we cannot attribute it only to an optical effect, but to more complicated processes in the perovskite solar cells induced by optical management. It will require a comprehensive study of opto-electronic processes in the active material to decouple optical effect from intrinsic material processes. Despite this, our findings suggest that optical optimisation of the perovskite solar cells is a valid strategy to bring them closer to the S-Q limiting efficiency. Our model is applicable for other solar cell types as well, and shows that accurate optical tuning of incoming and outcoming light is a crucial requirement for high efficiency solar cells.

Appendix A

A.1. Full-wave generalised detailed balance model

A.1.1. Optical constants used for calculations

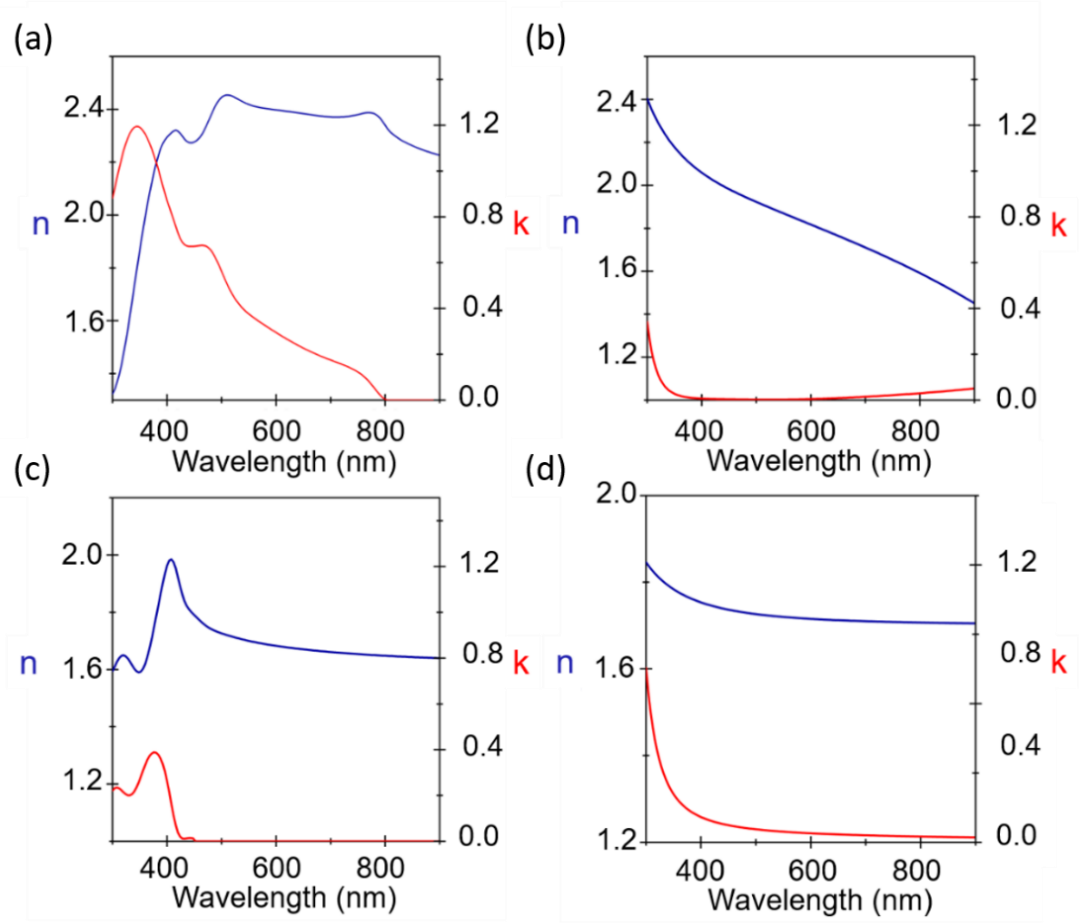

Figure A.1. Refractive index n and extinction coefficient k of materials used in our perovskite solar cells: (a) $FA_{0.8}MA_{0.2}PbI_{3-y}Br_y$, (b) ITO, (c) Spiro-OMeTAD and (d) SnO_2. Au dielectric function has been taken from Palik.

The refractive index n and extinction coefficient k of the perovskite material (as well as other materials constituting the solar cell) were determined in the 300-900 nm spectral region following an approach that combines the fitting of spectroscopic ellipsometry spectra (SOPRA GES-5E ellipsometer) and transmittance. The reflectance spectra were measured with a spectrophotometer (PerkinElmer UV/Vis/NIR). Ellipsometry spectra are highly sensitive to the perovskite n and k from 300 nm to the bandgap wavelength (approximately 805 nm). Above this wavelength, transmittance is the most sensitive to k. Therefore the combined analysis of both kinds of measurements is required for an accurate determination of the perovskite n and

k in the whole spectral region. Both the ellipsometry and spectrophotometer data fitting were done simultaneously in the coherent transfer matrix formalism.

A.1.2. Perovskite absorption coefficient in the band edge region

The absorption coefficient has been calculated using the following relation: $\alpha(\lambda) = 4\pi k(\lambda)/\lambda$, where k is the extinction coefficient of perovskite material and λ is the wavelength.

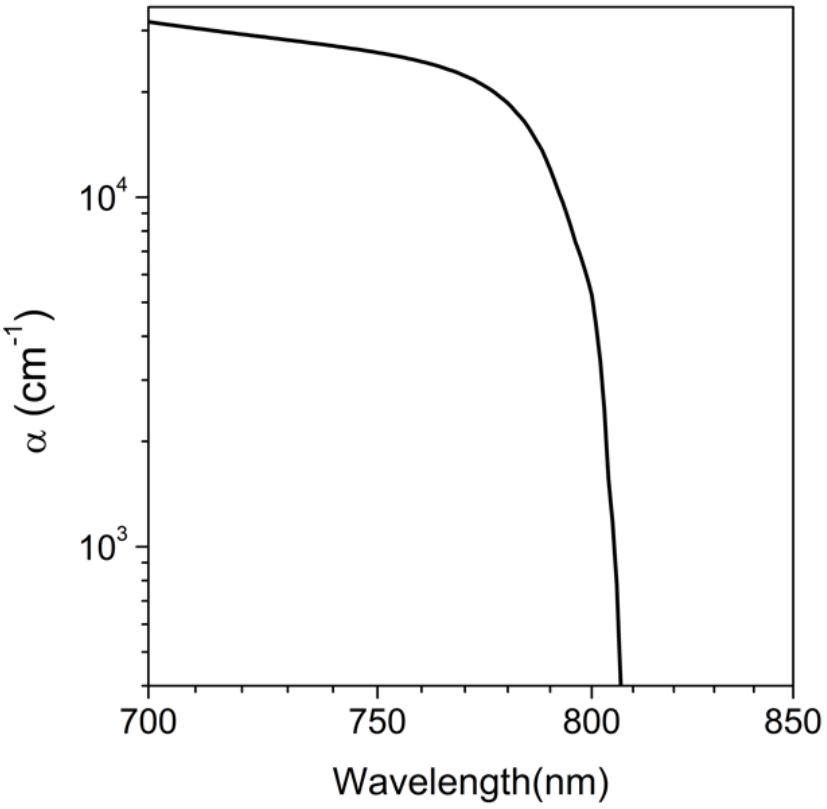

Figure A.2. Absorption coefficient α of $FA_{0.8}MA_{0.2}PbI_{3-y}Br_y$ perovskite material as a function of wavelength in a band edge region.

A.1.3 Consistency check.

To make sure that our model and simulations are correct we have performed a consistency check. According to power conservation, the sum of reflected and absorbed optical powers must be equal to 1 ($R_{tot} + \Sigma_i A_j = 1$), our solar cell being opaque (T_{tot}=0).

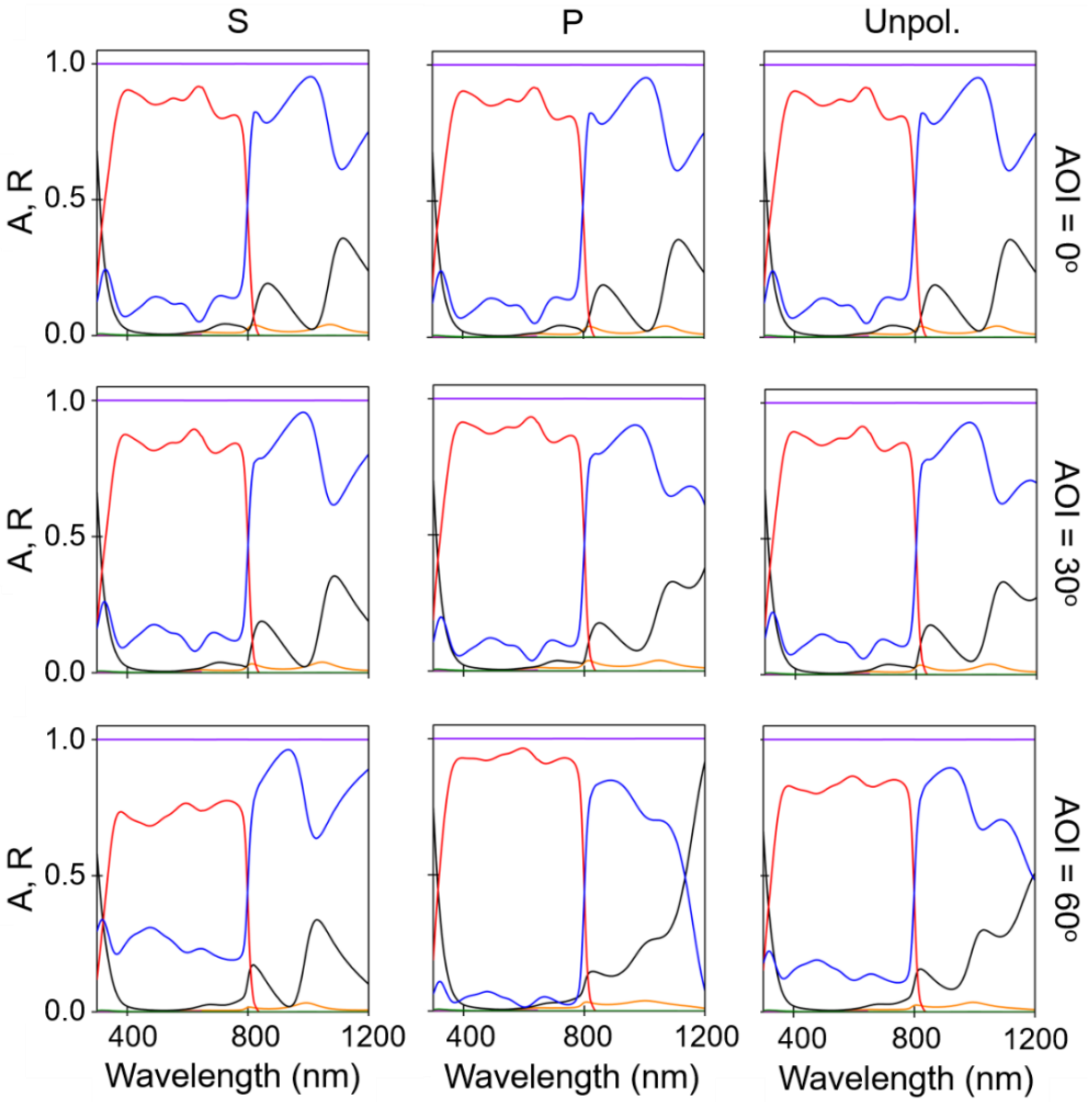

Figure A.3 Consistency check for S, P polarisation and unpolarised case (columns S, P and Unpol.) for several angles of incidence (AOI = 0°, 30°, 60°) over a range of wavelengths for our solar cell structure. Note that light is not transmitted through the back metal contact as it acts like a mirror, so the light escapes only from one side (reflected). Colour code: Au – orange, Spiro-OMeTAD – green, PVK – red, SnO_2 – magenta, ITO – black, reflectance of the whole structure R_{tot} – blue and the sum of contributions – purple. To get convergence, the discretisation of the depth should be as small as 0.01 nm for absorbance calculations.

A.1.4. Wavelength and angle dependent absorbance maps

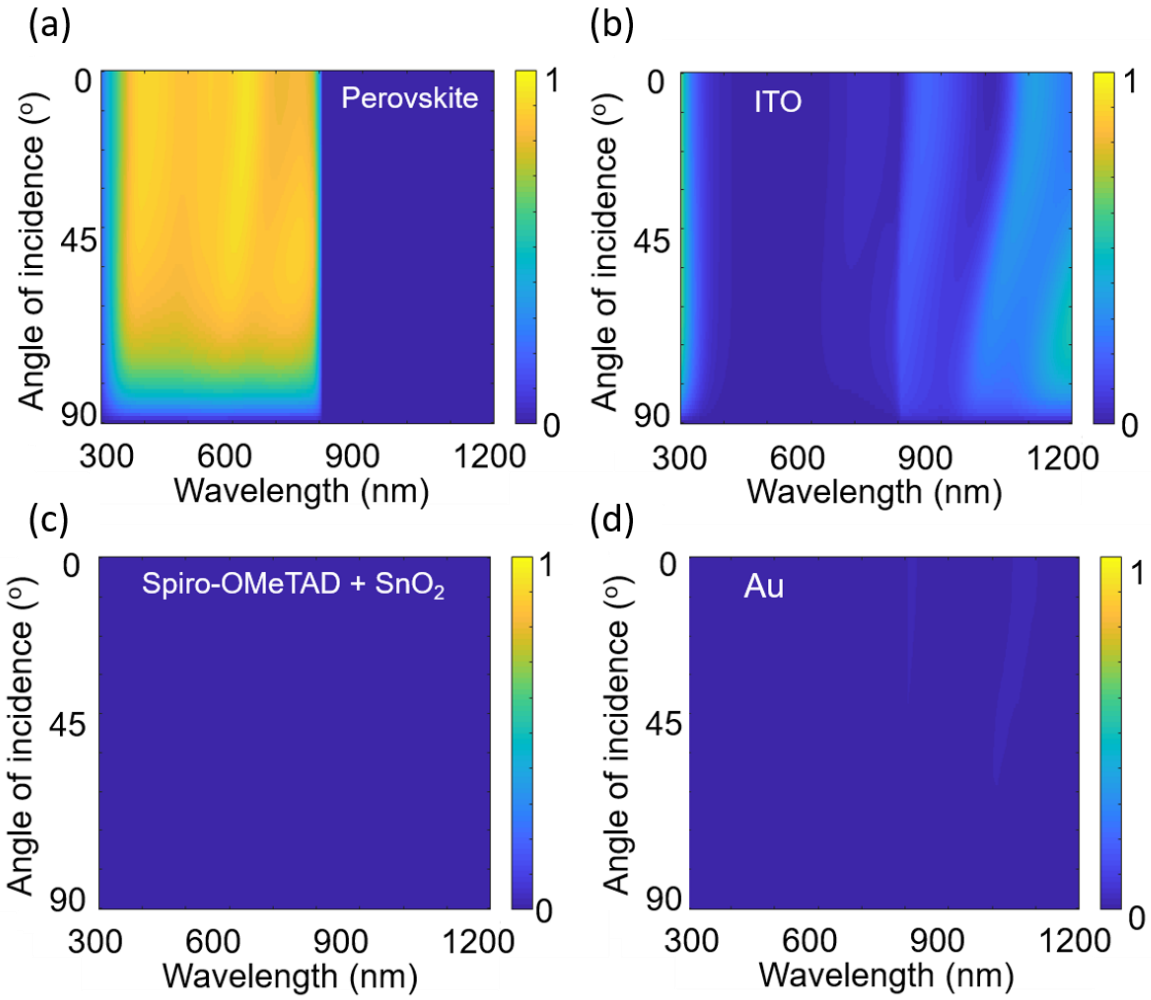

Figure A.4 Absorbance as a function of wavelength and angle of incidence for each layer of our perovskite solar cell structure: (a) $FA_{0.8}MA_{0.2}PbI_{3-y}Br_y$ perovskite layer, (b) ITO, (c) Spiro-OMeTAD and SnO_2, (d) Au.

A.2. Methods for fabrication of perovskite – base solar cells

Commercial full-covered indium tin oxide (ITO) glasses (100 nm, 15 Ωsq^{-1}, Stuttgart) were cleaned in soap, deionised water, acetone, and isopropanol under sonication for 10 min in sequence and then treated by UV−ozone plasma for 10 min. To get the SnO_2 nanoparticle precursor for electron transport layer (ETL), SnO_2 nanoparticle suspension (Alfa Aesar (tin(IV) oxide (134 µL), 15% in H_2O colloidal dispersion) were mixed with methanol Scharlau, 99.5% (866 µL). SnO_2 nanoparticle solution was spin-coated onto the cleaned ITO substrates at 4000 rpm, followed by a thermal annealing at 150 ºC during 30 minutes in air. The thickness of the

ETL is around 20 nm. The perovskite layer was then deposited by a sequential two-step spin-coating method. The lead precursor was prepared by dissolving 1.1 M PbI_2 (Sigma Aldrich, 99%) solution in dimethylformamide (Sigma-Aldrich, 99.8%) and dimethylsulfoxide (VWR, 99.5%) with a 4:1 volume ratio and adding 3 M % of $PbBr_2$ (Sigma Aldrich, 99.999%). The organic precursor was prepared by mixing of $CH(NH_2)_2I$ Sigma Aldrich, 98% (70 mg) and CH_3NH_3Br Sigma Aldrich, 98% (9 mg) in of isopropanol Scharlau, 99.5% (1 ml). The lead solution was spin-coated at 60 ºC on top of the electron transport layer at 1600 rpm in the N_2 environment, then taken outside the glovebox. The organic precursor was spin-coated at 1500 rpm in ambient conditions with a controlled relative humidity below 40%. The coated samples were annealed during 30 minutes at 100ºC and another 30 minutes at 150ºC. The hole transporting layer (HTL) solution was prepared by dissolving Spiro-OMeTAD (2,2′,7,7′-tetrakis(N,N-dimethoxyphenylamine)-9,9′-spirobifluorene), Merck (72.3 mg), 4-tert-butylpyridine 99.9%, Sigma-Aldrich (28.9 mL) and a stock solution (17.5 mL) of lithium bis(trifluoromethylsulphonyl)imide in acetonitrile Sigma-Aldrich, 99.9% (520 mg) in chlorobenzene Sigma-Aldrich, 99.9% (1 mL). A 140 nm thick HTL was deposited by spin-coating the solution at 4000 rpm for 45 s. Finally, the Au (80 nm, 1 $Å \cdot s^{-1}$) was deposited by thermal evaporation in a high vacuum chamber (Lesker) under a pressure of $<5 \times 10^{-6}$ mBar.

A.3. Optical measurements

A.3.1. Fluorescence quantum yield.

The sample was placed inside a four-port integrating sphere, with the perovskite layer being in contact with the Spectralon sample holder located at the port facing the input one. The incident light emitted by a continuous wave (cw) Nd:YAG laser (532 nm), incoming from the input port, was therefore impinging onto the sample from the side of the glass substrate so that it pumped the perovskite layer after crossing the glass and TiO_2 layer. The sample was tilted of a few degrees from the incident beam to ensure that the light reflected by it could not escape directly through the input port. A fibered spectrometer connected to the third port of the integrated sphere was used to record the perovskite fluorescence spectrum. A calibrated Si detector connected to the fourth port of the integrating sphere was used to perform the external fluorescence quantum yield measurements. To achieve such measurements, suitable optical filters were placed alternatively between the port of the integrating sphere and detector to separate the contributions of the scattered/reflected light (λ_{scatt} = 532 nm) and of the perovskite fluorescence (λ_{fluo} = 810 nm). After correcting for the filter transmittance, one obtains the

scattered power P_{scatt} and the fluorescence power P_{fluo} for the measured sample. After measuring the reference signals $P_{scatt,ref}$ and $P_{fluo,ref}$ (Spectralon sample holder without sample), the external fluorescence quantum yield *f* (in %) was obtained from the relation:

$$QY = \frac{(P_{fluo} - P_{fluo\ ref}) \cdot \lambda_{fluo}}{(P_{scatt\ ref} - P_{scatt}) \cdot \lambda_{scatt}} \cdot 100\% \qquad (A.1)$$

The fluorescence quantum yield was measured for different values of incident photon flux, controlled by using combinations of optical density filters mounted on filter wheels placed along the optical path. The measurements were done with a gradually increasing photon flux, and the beam was blocked by a shutter between each measurement. At the lowest photon fluxes (a few sun-equivalent), an increasing transient of the fluorescence signal was observed on the time scale of seconds. The power values were recorded after stabilisation. At the highest photon fluxes (several tens of sun equivalent), no increasing transient was observed but a decrease in the fluorescence signal was observed after near 10 s. In this case, the power values were recorded immediately after opening the shutter. Note that to ensure that steady-state conditions could be reached, the measurements were done in purely continuous conditions, that is, without any modulation nor lock-in amplification of the incident cw light.

A.3.2. Open circuit voltage under monochromatic light illumination.

The V_{oc} of selected solar cells was measured under monochromatic continuous wave laser excitation (Verdi V6, wavelength: 532 nm), for comparison with measurements under polychromatic light in the solar simulator. The samples were illuminated with an expanded and collimated beam to illuminate completely their surface as in the solar simulator. In **Figure A.5** is shown the measured V_{oc} for a selected solar cell. It presents a V_{oc} of 1.08 V under one sun illumination, which is in good agreement with V_{oc} = 1.1 V measured with the solar simulator.

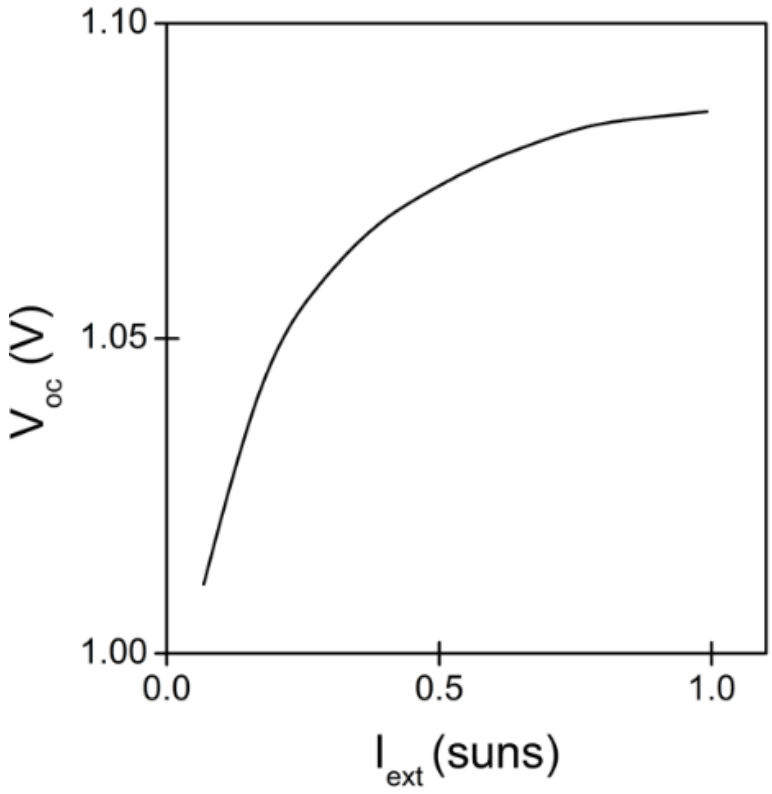

Figure A.5 V_{oc} measured under laser excitation with a wavelength of 532 nm for a selected cell.

A.4. Comparison: current model with Green functions model

For the sake of completeness, the QY calculated with the current model was compared with the one reported in Abebe et. al., based on calculations with a model involving Green functions and thus including coherent effects to rigorously determine the spatial power distribution of dipole emission. In our calculations, the same cell structure as the one provided in Abebe et was used. When assuming η_{int} = 100%, with our model a QY of 50% was obtained. This value is slightly higher than the one obtained in Abebe et for the same η_{int} = 100%, QY = 40%. With our model, it is predicted that most of the parasitic absorption occurs in the ITO, in a similar way as in Abebe et.

A.5 Champion cell

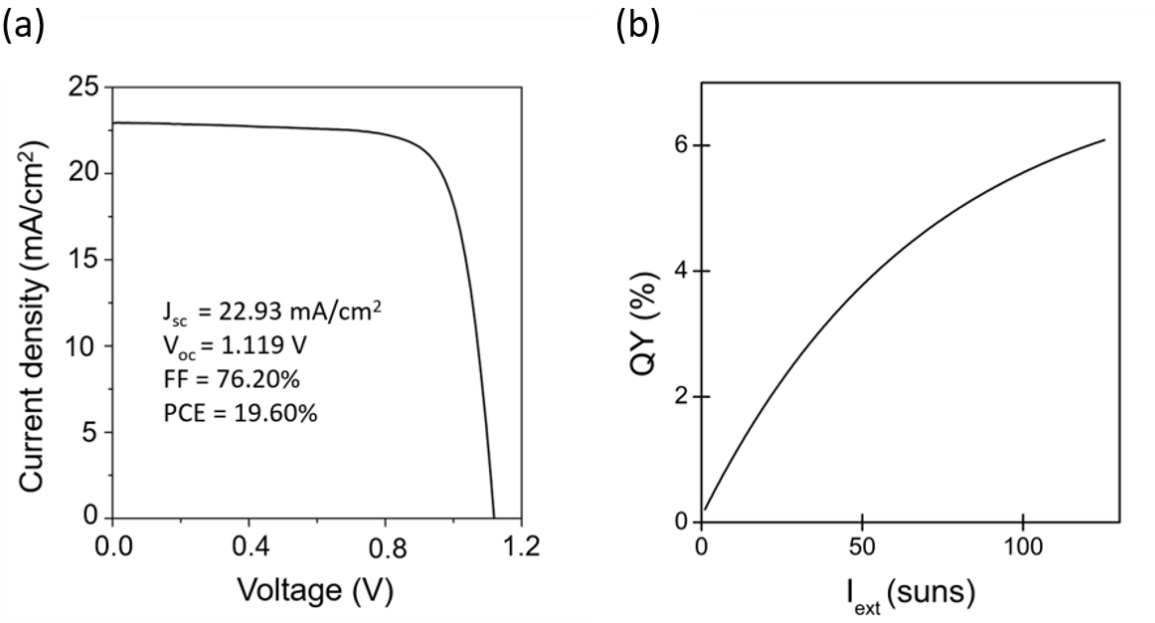

Figure A.6 (a) J-V characteristic curves of our champion solar cell in reverse scan. (b) QY as a function of excitation intensity for this solar cell. The QY at 1 sun is 0.2%.

A.6. Photovoltaic properties of the cells

To estimate the role of R_{sh} on V_{oc} of our cells, its effect on V_{oc} has been calculated using the following equation:

$$J_{sc} - J_0 e^{qV_{oc}/kT_c} - \frac{V_{oc}}{R_{sh}} = 0 \qquad (A.2)$$

Short circuit current J_{sc} and dark saturation current J_0 have been obtained from **Eq. (1.2)** and **Eq. (1.3)** respectively applying the TMM calculations. Simulated V_{oc}'s are shown versus R_{sh} in **Figure A.7.** For the R_{sh} values measured for our cells (located in the blue shadowed region in **Figure A.7.** R_{sh} does not affect V_{oc}.

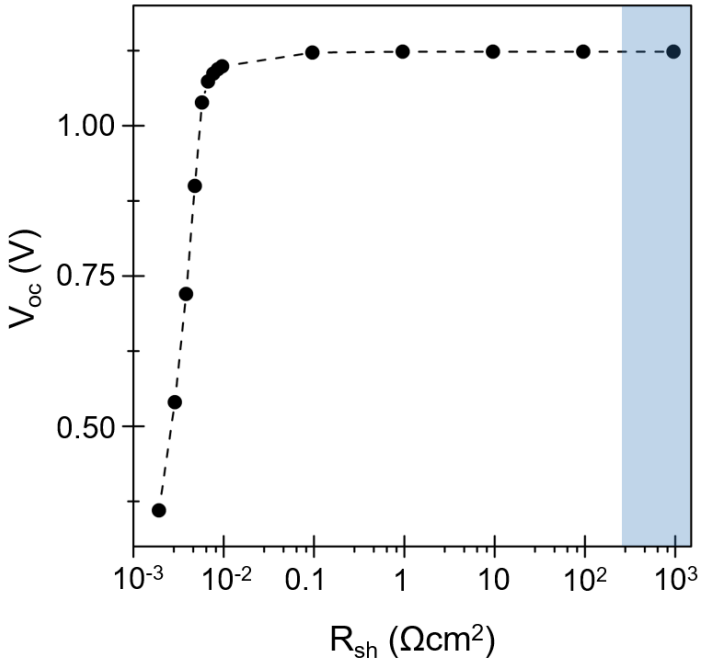

Figure A.7 Simulations of the effect of shunt resistance on V_{oc} for our solar cell configuration. The region of experimental R_{sh} values is depicted in blue.

Appendix B

B.1. Perovskite growth and solar cell fabrication.

B.1.1. Process flow and perovskite formation mechanism with the compact PbI_2 – templated and porous PbI_2 – templated growth approaches

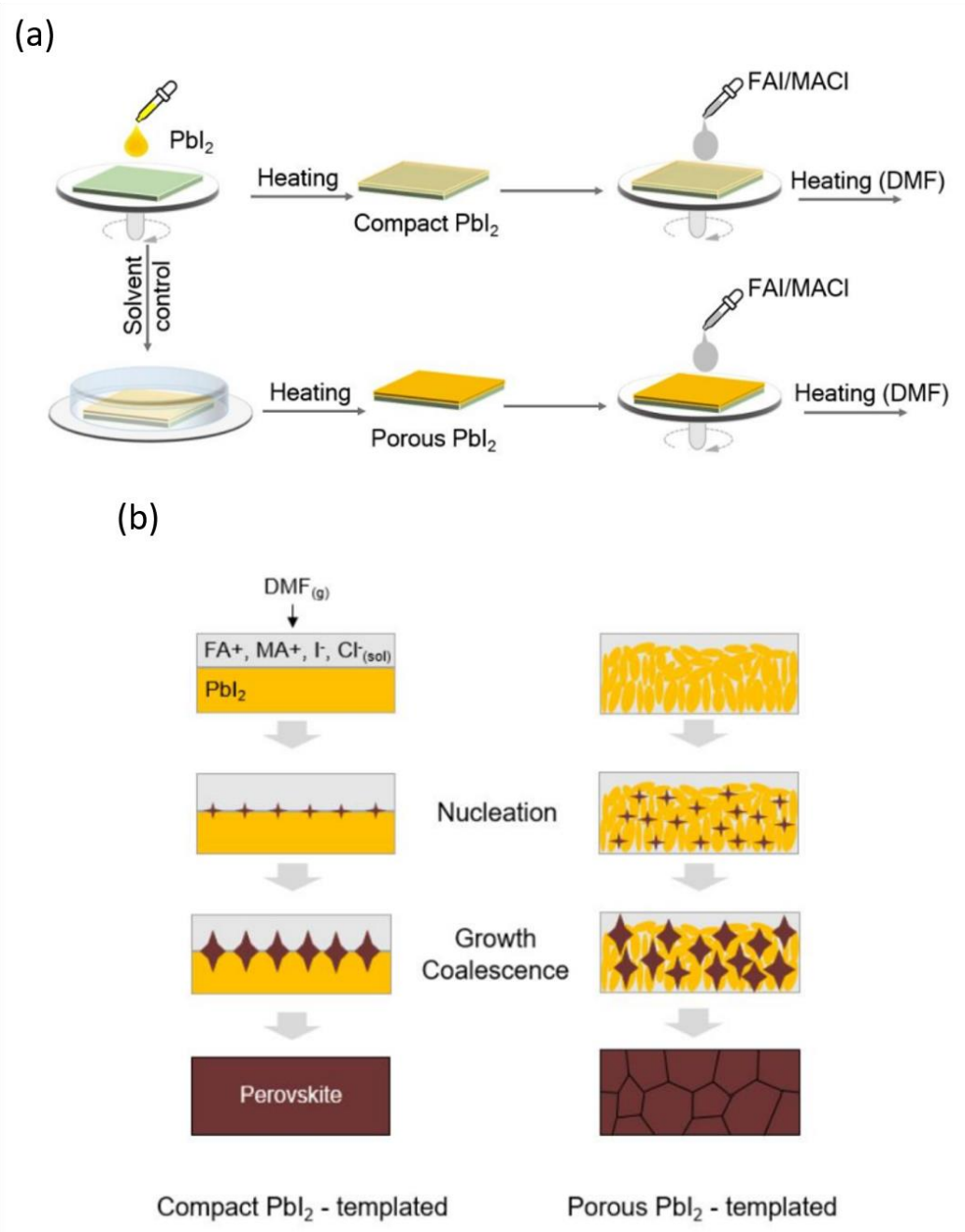

Figure B.1. (a) Process flow of the two preparation methods (compact PbI_2 – templated and porous PbI_2 – templated). (b) Mechanism of the second step for the two methods. When using a compact PbI_2 template (yellow), much larger perovskite crystals (brown) can be formed than when using a porous PbI_2 template, the porosity of which facilitates the organic precursor infiltration and thus the full PbI_2 – to – perovskite conversion but sets a limit on the final

perovskite crystal size. Achieving the full PbI_2 – to – perovskite conversion with a compact PbI_2 template becomes a challenge when using an organic precursor containing FA^+ cations, because such large ions hardly get incorporated into the PbI_2 template in the absence of porosity. This is made possible by the combined action of Cl^- ions and a solvent annealing in DMF.

B.1.2 Solar cell fabrication

The commercial indium tin oxide (ITO) glasses (15 Ω/sq) were cleaned in cleaning agent, deionised water, acetone, and isopropanol under sonication for 10 min in sequence and then treated by UV−ozone plasma for 10 min. The electron transport layer (ETL) of titanium diisopropoxide bis- (acetylacetonate) (Sigma-Aldrich) stabilised TiO_2 nanoparticle solution (4−8 nm diameter, 20 wt % in water, PlasmaChem GmbH) was coated on the ITO substrate at 6000 rpm and annealed at 150 °C for 30 min in air. The thickness of the ETL is around 50 nm. The perovskite layer was then deposited by a sequential two-step spin-coating method; first, 1.0 M of PbI_2 (99%, Sigma-Aldrich) in anhydrous N,N-dimethylformamide (DMF) (99.8%, Sigma-Aldrich) was spin-coated onto the ETL at 2500 rpm for 30 s. To prepare a compact PbI_2 film, the substrate was moved to a hotplate immediately after the spin-coating and annealed at 100 °C for 10 min to remove the remaining solvent; in contrast, to prepare a porous PbI_2 film, the as spun film was kept at a closed environment (covered by a Petri dish) to retard the solvent evaporation for 10 min and then annealed at 100 °C for 10 min. Second, after the PbI_2-coated substrates cooling to room temperature (25 °C), 0.3 M of $CH(NH_2)_2I$ (98%, SigmaAldrich) in 1 mL isopropanol with 10 mol % of CH_3NH_3Cl (Sigma Aldrich) was spin-coated onto the PbI_2 at 2500 rpm for 45 s and then annealed at 150 °C for 20 min without (thermal annealing) or with (solvent annealing) the presence of small amount (5 μL) DMF in a closed environment. The HTL solution was prepared by dissolving 72.3 mg (2,2′,7,7′-tetrakis(N,N-dimethoxyphenylamine)-9,9′-spirobifluorene) (Spiro-OMeTAD, Merck), 28.9 mL 4-tert-butylpyridine (99.9%, Sigma-Aldrich) and 17.5 mL of a stock solution of 520 mg/ mL lithium bis(trifluoromethylsulphonyl)imide in acetonitrile (99.9%, Sigma-Aldrich) in 1 mL chlorobenzene (99.9%, Sigma-Aldrich). The ∼200 nm thick HTL was deposited by spin-coating the solution at 3000 rpm for 45 s. Finally, the Au (80 nm, 1 Å·s −1) was deposited by thermal evaporation under a pressure of mBar.

B.2. Structural characterisation.

The XRD patterns of the perovskite films were characterised with a Bruker D8 diffractometer in the Bragg−Brentano (θ−2θ) configuration. The top-view SEM images of the perovskite films were obtained by field emission SEM (FEG-SEM, FEI Inspect F-EBL). For the cross-sectional observation of the device structure, a Zeiss Auriga setup was used. It combines a Ga-focused ion beam (FIB) for cross section preparation and SEM functionalities for specimen observation. A layer of Pt was first deposited on the surface to protect the top structure from FIB milling. Then, the materials were subsequently milled by Ga FIB at 30 kV, with currents of 1 nA for coarse milling and 50 pA for fine milling. The cross section was then observed by SEM at 54° with acceleration voltage of 5 kV and an aperture of 30 μm.

B.3. Photovoltaic characterisation of the solar cells.

The current density−voltage (J−V) characteristics were measured using a Keithley 2400 SourceMeter under the illumination of the solar simulator (ABET Sol3A) at the light intensity of 100 $mW \cdot cm^{-2}$ which was adjusted with a monocrystalline silicon reference cell (Hamamatsu) calibrated at the Fraunhofer Institute for Solar Energy Systems. The measurements were carried out in the ambient atmosphere with a scanning rate of 10 $mV \cdot s^{-1}$. Both scanning directions (forward and reverse) were measured to check the hysteresis effect of the device. The steady-state measurements were performed by setting the bias voltage to the voltage at maximum power point (VMPP, determined from the J−V curves) and then tracing the current density as function of time during 60 s. The device stability was studied by monitoring the J−V characteristics of the cells under 1 sun light illumination, the illumination was carried out in the glovebox and the J−V measurement was performed in air condition. EQE values were measured using a quantum efficiency measurement system (QEX10, PV Measurements). The spectral response of the calibrated silicon cell was used as a reference. Transient photovoltage (TPV) of the devices were measured with an in-house-built setup. The setup comprises a light-emitting diode (LED) lamp to provide steady-state white bias light, a 637 nm wavelength laser (Vortran Stradus), and an Agilent 4000X oscilloscope. The LED lamp was used to get steady V_{oc} of the device. The intensity of the laser was controlled to keep the voltage transient amplitude under 5% of the steady-state light bias. The oscilloscope records the data using 1 MΩ input impedance for the TPV measurement.

B.4. Supplementary cross-section SEM images of the compact PbI_2 – templated perovskite solar cell

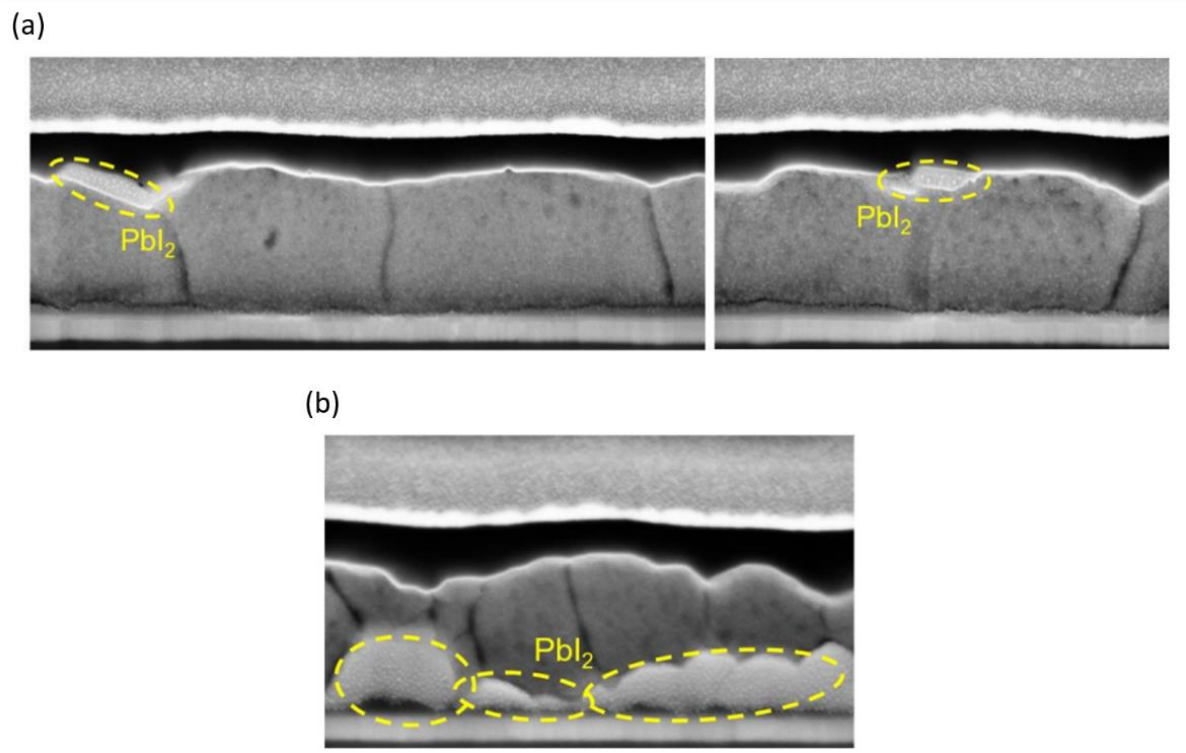

Figure B.2. (a) Supplementary cross-section SEM images of the compact PbI_2 – templated perovskite solar cell. PbI_2 can be seen only at the perovskite/spiro-OMeTAD interface (no unreacted PbI_2 at the TiO_2/perovskite interface). This demonstrates that a complete conversion of the PbI_2 template into perovskite occurred, and that the PbI_2 at the perovskite/spiro-OMeTAD interface appeared after the perovskite formation. Therefore, such PbI_2 is the result of a self-passivation of the perovskite that occurred likely during the annealing at 150ºC. This small amount of self-passivated PbI_2 is also detected by XRD and stands for the brighter contrasts. (b) Cross-section SEM image of a "failed" device with unreacted PbI_2. This image confirms that, when the conversion of the PbI_2 template into perovskite is incomplete, unreacted PbI_2 is located near the TiO_2/perovskite interface.

B.5. Relation between V_{oc} and fluorescence quantum yield in perovskite solar cells with surface trapping states

When including recombination via trap states, the detailed balance equation from Shockley and Queisser may be modified to:

$$J_{ph} - (J_{rg} + J_{dg})\left(e^{\frac{qV}{kT}} - 1\right) - J_t(V) + J_{tg} - J(V) = 0 \quad \text{(B.1)}$$

where it has been assumed that the non-radiative direct recombination fits the ideal rectifier equation, k is the Boltzmann constant, T the cell temperature, and the different current densities stand for:

Jph : electron-hole pair generation due to solar radiation

Jrg : electron-hole pair generation due to other radiation than sun photons surrounding the cell

Jdg : non-radiative electron-hole pair generation

$Jt\,(V)$: non-radiative electron-hole pair recombination via deep trap states

Jtg : electron-hole generation by deep trap states

$J(V)$: current in the cell under the voltage V

There are four processes involved in recombination by trapping: electron capture from the conduction band, electron emission toward the conduction band, hole capture from the valence band, and hole emission toward the valence band. It can be shown that out of equilibrium but in steady-state the rate of recombination is:

$$U = \frac{pn - n_i^2}{\tau_{p0}(n+n_1)+\tau_{n0}(p+p_1)} \quad \text{(B.2)}$$

where: n and p are the electron and hole concentration in the conduction and valence band, respectively. τ_{n0} and τ_{p0} are the lifetimes for electrons in the conduction band to fall in an empty trap and for holes from the valence band to be captured by a trapped electron, respectively. n_1 and p_1 are the densities of electrons in the conduction band and holes in the valence band when the Fermi level coincides with the energy of the trapped states, respectively. n and p are given by:

$$n \propto e^{-\frac{q(E_c - E_{Fn})}{kT}} \quad \text{(B.3a)}$$

$$p \propto e^{\frac{q(E_v - E_{Fp})}{kT}} \quad \text{(B.3b)}$$

The product np is proportional to:

$$np \propto e^{-\frac{Eg}{kT}} e^{\frac{q(E_{Fn}-E_{Fp})}{kT}} \quad \text{(B.4)}$$

To determine the defect state recombination current density we will assume that the majority of traps are at the crystal interfaces between two perovskite crystals. Provided that such interfaces are passivated with PbI_2 which may act as an effective electron blocker or trap, it is reasonable to assume that at such interfaces:

$\tau_{p0} n_1 > \tau_{n0} p$

and that: n

$1 \gg p_1, n$

These assumptions are consistent with the values reported in Sherkar et. al.. Then, (B.2) simplifies to:

$$U \approx \gamma \frac{pn - n_i^2}{n_1} = \frac{\gamma n_i^2}{n_1}\left(\frac{pn}{n_i^2} - 1\right) = \frac{\gamma n_i^2}{n_1}\left(e^{\frac{qV}{kT}} - 1\right) \quad \text{(B.5)}$$

where $\gamma = 1/\tau_{p0}$. Applying the continuity equation in steady state:

$$\frac{\partial \rho}{\partial t} = U - \frac{\partial J_e}{\partial x} = 0 \quad \text{(B.6)}$$

where ρ is the charge density and J_e is the current density for the electrical charges, we may obtain the trap assisted recombination current density:

$$J_t = ql\frac{\gamma n_i^2}{p_1}\left(e^{\frac{qV}{kT}} - 1\right) = J_{tg}\left(e^{\frac{qV}{kT}} - 1\right) \quad \text{(B.7)}$$

where l is the thickness at the interface region where electron trapping takes place. Now, (B.1) can be rewritten as:

$$J_{ph} - \left(J_{rg} + J_{dg} + J_{tg}\right)\left(e^{\frac{qV}{kT}} - 1\right) - J(V) = 0 \quad \text{(B.8)}$$

and the open circuit voltage as:

$$V_{oc} = \frac{kT}{q}\ln\left(\frac{J_{ph}}{J_{rg}+J_{rg}+J_{tg}} + 1\right) \quad \text{(B.9)}$$

(B.9) may be written as:

$$V_{oc} = \frac{kT}{q} \ln\left(\frac{fJ_{ph}}{J_{rg}} + 1\right) \quad \text{(B.10)}$$

Where the f is the external fluorescence quantum yield:

$$f = \frac{J_{rg}}{J_{rg}+J_{dg}+J_{tg}} \quad \text{(B.11)}$$

Appendix C

C.1 Genetic algorithm optimisation

C.1.1 Genetic algorithm

The Matlab genetic algorithm tool (GA) was employed for optimisation of DM to achieve the maximum efficiency of a solar cell. GA is a search-based optimisation technique that seeks optimal solutions to problems by applying the principles of natural selection and evolution. It is a stochastic, population-based algorithm that searches randomly by mutation and crossover among population members. Our problem required several constraints on 1) thickness and 2) refractive index of DM and on 3) PCE of solar cell to maximise it. Optimisation have been performed for 8 configurations of DMs, from 1 to 8 layers.

C.1.2 Scheme of the optimisation flow

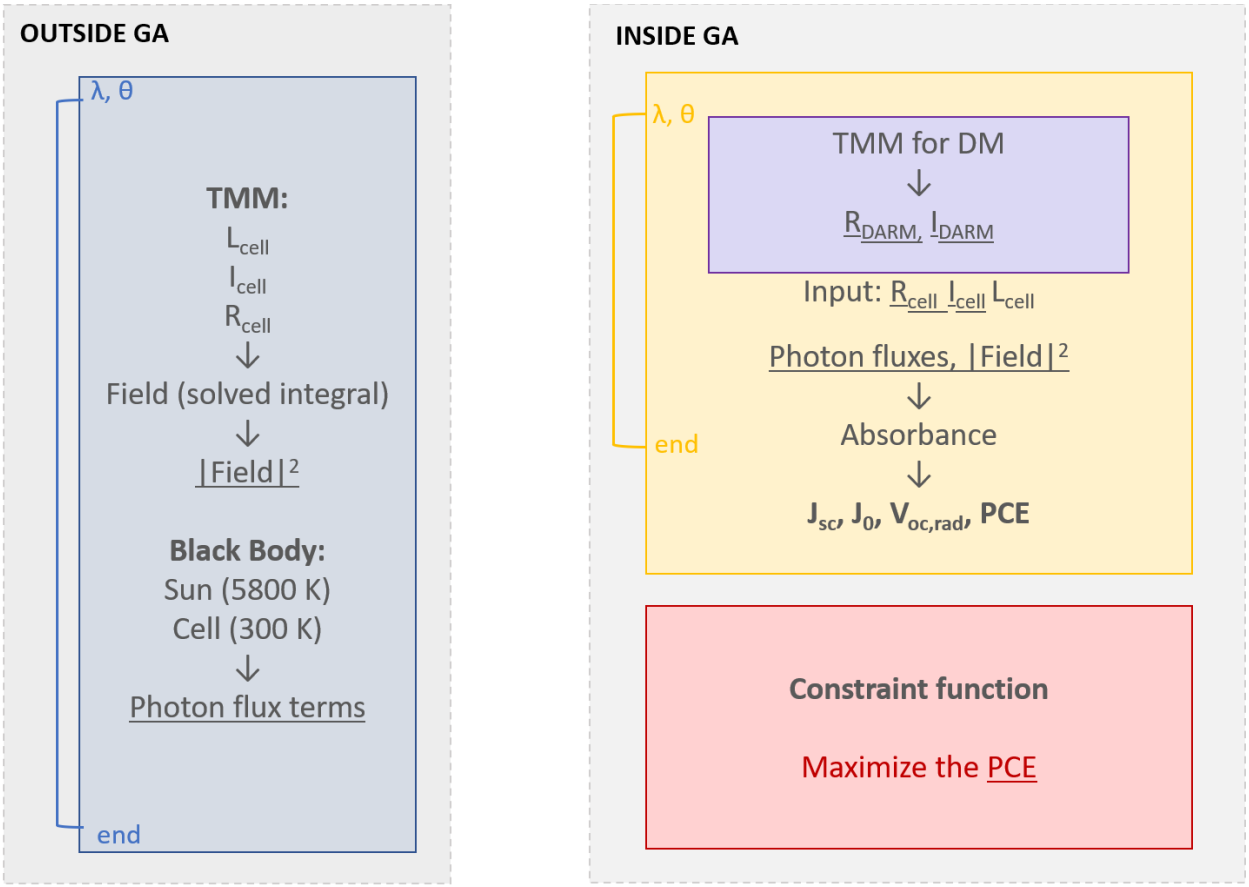

Figure C.1 Scheme of the optimisation flow.

C.2 Full – wave generalised detailed balance model

With the reflectance and transmittance of the DM-air interface being R_{DM} and T_{DM} and those of the cell being R_{cell} and T_{cell}, the total reflectance of the whole structure is:

$$R_{tot} = \frac{R_{DM}+R_{cell}-2R_{DM}R_{cell}}{1-R_{DM}\,R_{cell}}. \tag{C.1}$$

In order to take into account the effect of the incoherent glass substrate the incoming electric field is normalised by a factor $(1-R_{DM})/n_{glass}(1-R_{DM}R_{cell})$.

Components of the electric field can be derived from internal transfer coefficients, for active layer of perovskite are:

$$E_{y,pvk} = \left[t^{+}_{pvk}e^{ik_{z,pvk}z} + t^{-}_{pvk}e^{-ik_{z,pvk}z}\right]e^{ik_{x,0}x} \tag{C.2a}$$

$$E_{x,pvk} = \frac{k_{z,pvk}}{\eta_{pvk}k_0}\left[t^{+}_{pvk}e^{ik_{z,pvk}z} + t^{-}_{pvk}e^{-ik_{z,pvk}z}\right]e^{ik_{x,0}x} \tag{C.2b}$$

$$E_{z,pvk} = \frac{k_{x,0}}{\eta_{pvk}k_0}\left[t^{+}_{pvk}e^{ik_{z,pvk}z} + t^{-}_{pvk}e^{-ik_{z,pvk}z}\right]e^{ik_{x,0}x} \tag{C.2c}$$

where k_0 is the wavenumber, t^{-}_{pvk} and t^{+}_{pvk} are the internal transfer coefficients of the perovskite layer.

Analytical solutions for integrals of electric field components:

TE (S polarisation):

$$\int_0^{d_{pvk}} \left|E_{y,pvk}(z)\right|2\,dz = e^{-2Im(k_{x,0})}\,.$$
$$\cdot\left[-\frac{i\,t^{+}_{pvk}\left(t^{-}_{pvk}\right)^{*}}{2Re(k_{z,pvk})}\left(e^{2id_{pvk}Re(k_{z,pvk})}-1\right)+\frac{i\,t^{-}_{pvk}\left(t^{+}_{pvk}\right)^{*}}{2Re(k_{z,pvk})}\left(e^{-2id_{pvk}Re(k_{z,pvk})}-1\right)+\right.$$
$$\left.+\frac{d_{pvk}t^{+}_{pvk}\left(t^{+}_{pvk}\right)^{*}}{2Im(k_{z,pvk}d_{pvk})}\left(1-e^{-2Im(k_{z,pvk}d_{pvk})}\right)+\frac{d_{pvk}t^{-}_{pvk}\left(t^{-}_{pvk}\right)^{*}}{2Im(k_{z,pvk}d_{pvk})}\left(e^{2Im(k_{z,pvk}d_{pvk})}-1\right)\right] \tag{C.3}$$

TM (P polarisation):

$$\int_0^{d_{pvk}} \left|E_{x,pvk}(z)\right|2\,dz = \left|\frac{k_{z,pvk}}{(n_{pvk}+ik_{pvk})k_0}\right|^2 e^{-2Im(k_{x,0})}\,.$$
$$\cdot\left[\begin{array}{l} -\frac{i\,t^+_{pvk}\left(t^-_{pvk}\right)^*}{2Re(k_{z,pvk})}\left(e^{2id_{pvk}Re(k_{z,pvk})}-1\right)+\frac{i\,t^-_{pvk}\left(t^+_{pvk}\right)^*}{2Re(k_{z,pvk})}\left(e^{-2id_{pvk}Re(k_{z,pvk})}-1\right)+ \\ +\frac{d_{pvk}t^+_{pvk}\left(t^+_{pvk}\right)^*}{2Im(k_{z,pvk}d_{pvk})}\left(1-e^{-2Im(k_{z,pvk}d_{pvk})}\right)+\frac{d_{pvk}t^-_{pvk}\left(t^-_{pvk}\right)^*}{2Im(k_{z,pvk}d_{pvk})}\left(e^{2Im(k_{z,pvk}d_{pvk})}-1\right) \end{array}\right] \quad (C.4)$$

$$\int_0^{d_{pvk}} \left|E_{z,pvk}(z)\right|2\,dz = \left|\frac{k_{k,0}}{(n_{pvk}+ik_{pvk})k_0}\right|^2 e^{-2Im(k_{x,0})}\,.$$
$$\cdot\left[\begin{array}{l} \frac{i\,t^+_{pvk}\left(t^-_{pvk}\right)^*}{2Re(k_{z,pvk})}\left(e^{2id_{pvk}Re(k_{z,pvk})}-1\right)-\frac{i\,t^-_{pvk}\left(t^+_{pvk}\right)^*}{2Re(k_{z,pvk})}\left(e^{-2id_{pvk}Re(k_{z,pvk})}-1\right)+ \\ +\frac{d_{pvk}t^+_{pvk}\left(t^+_{pvk}\right)^*}{2Im(k_{z,pvk}d_{pvk})}\left(1-e^{-2Im(k_{z,pvk}d_{pvk})}\right)+\frac{d_{pvk}t^-_{pvk}\left(t^-_{pvk}\right)^*}{2Im(k_{z,pvk}d_{pvk})}\left(e^{2Im(k_{z,pvk}d_{pvk})}-1\right) \end{array}\right] \quad (C.5)$$

The short circuit current and open-circuit voltage are calculated as indicated in the manuscript. The fill factor (FF) is calculated by its definition:

$$FF = \frac{V_{mp}J_{mp}}{V_{oc}\,J_{sc}} \quad (C.6)$$

To obtain the V_{mp} and J_{mp} the I-V curves of solar cells have been simulated.

C.3 Optical constants

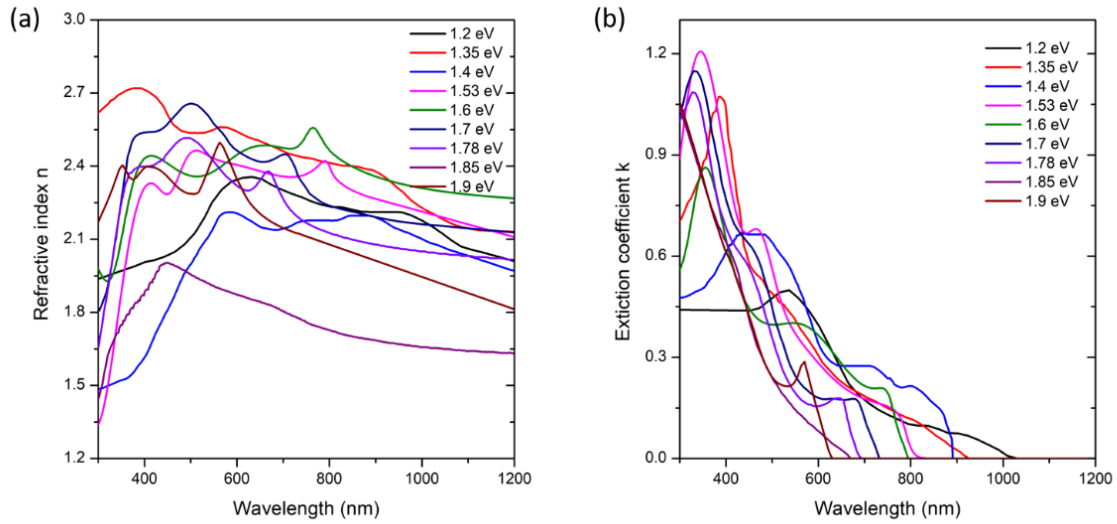

Figure C.2. (a) Refractive index and (b) extinction coefficient of perovskites studied in this work: $MASn_xPb_{1-x}I_3$ (1.2 eV), $MASn_xPb_{1-x}I_3$ (1.35 eV), $FASnI_3$ (1.4 eV), $FA_{0.8}MA_{0.2}PbI_{3-x}Br_x$ (1.53 eV), $MAPbI_3$ (1.6 eV), FACsPbIBr (1.7 eV), FACsCl (1.78 eV), $MAPbIBr_xCl_{1-x}$ (1.85 eV), $MAPbBr_3$ (1.9 eV).

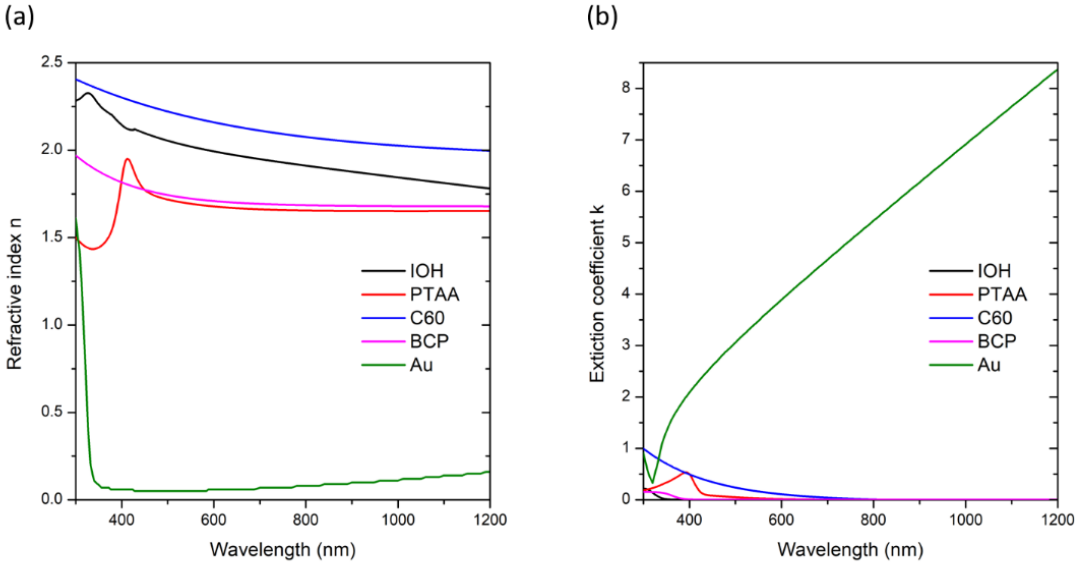

Figure C.3. (a) Refractive index and (b) extinction coefficient of IOH, PTAA, C60, BCP and Au.

C.4 Optimisation results for 1.53 eV and 1.6 eV perovskite solar cells

C.4.1 Configurations of dielectric multilayers (DMs)

Perovskite Band gap	**1.53 eV**							
Number of layers	**1**	**2**	**3**	**4**	**5**	**6**	**7**	**8**
Thickness (nm)	102	98 150	94 145 179	91 54 83 67	86 49 83 63 168	90 61 19 56 37 58	89 55 80 53 62 117 67	95 135 152 135 16 19 129 148
Refractive index	1.3	1.3 1.7	1.3 1.6 1.4	1.3 1.8 2.0 1.7	1.3 1.8 2.1 1.7 1.4	1.3 1.9 2.5 2.3 2.0 1.7	1.3 1.8 2.1 1.9 1.8 1.9 1.7	1.3 1.7 1.5 1.7 1.5 1.6 1.5 1.6

Table C.1 Parameters of DMs with 1 to 8 layers optimised for 1.53 eV perovskite -based solar cell.

Perovskite Band gap	**1.6 eV**							
Number of layers	**1**	**2**	**3**	**4**	**5**	**6**	**7**	**8**
Thickness (nm)	102	97 148	94 145 179	91 54 83 67	86 49 83 63 168	90 61 19 56 37 58	89 55 80 53 62 117 67	95 135 152 135 16 19 129 148
Refractive index	1.3	1.3 1.7	1.3 1.6 1.4	1.3 1.8 2.0 1.7	1.3 1.8 2.1 1.7 1.4	1.3 1.9 2.5 2.3 2.0 1.7	1.3 1.8 2.1 1.9 1.8 1.9 1.7	1.3 1.7 1.5 1.7 1.5 1.6 1.5 1.6

Table C.2 Parameters of DMs with 1 to 8 layers optimised for 1.6 eV perovskite -based solar cell.

C.4.2 Photovoltaic parameters of 1.53 eV and 1.6 eV

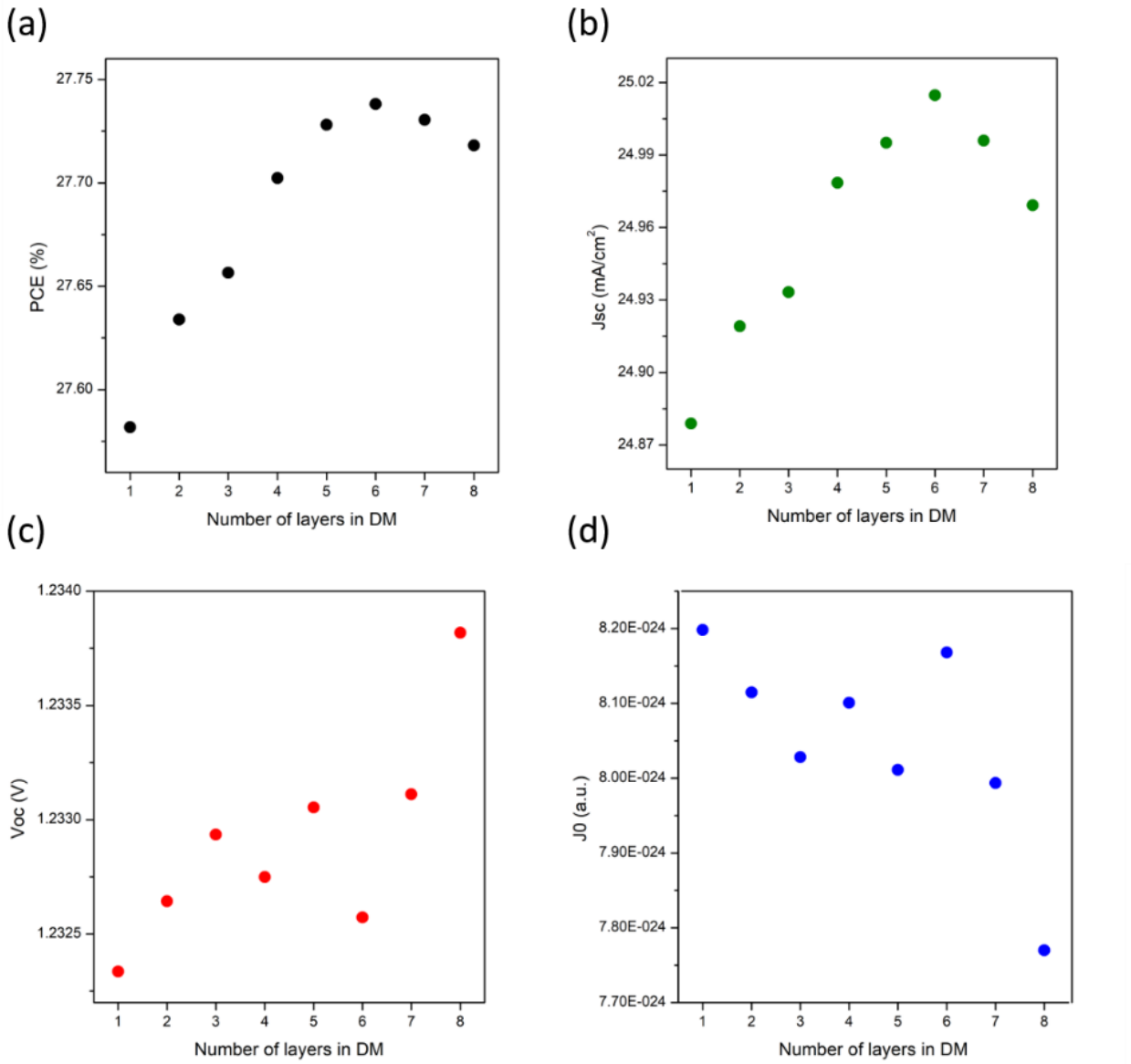

Figure C.4. Photovoltaic parameters of 1.53 eV perovskite based solar cell (a) PCE, (b) J_{sc}, (c) V_{oc} and (d) J_0 as a function of number of layers in DM.

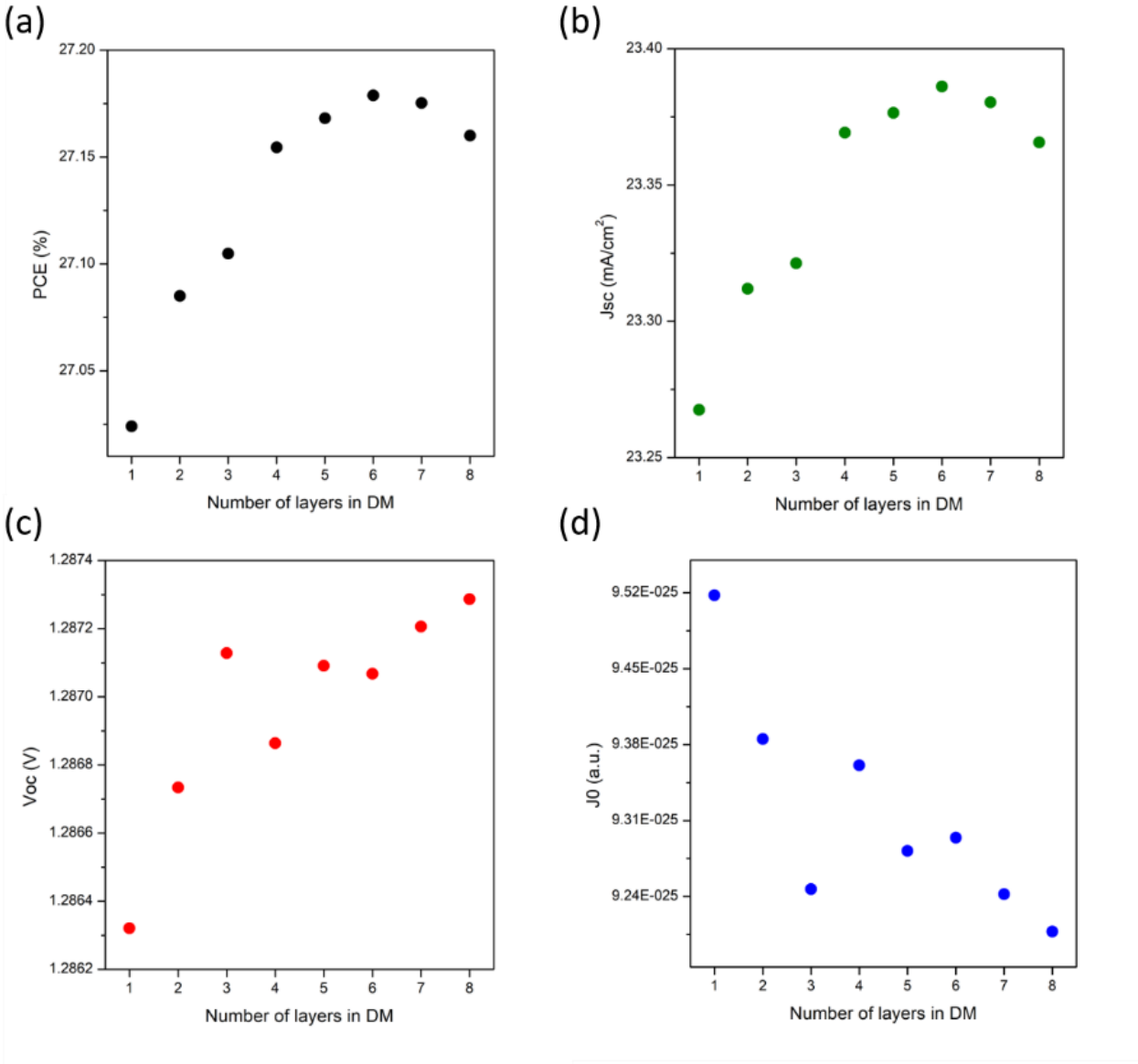

Figure C.5. Photovoltaic parameters of 1.6 eV perovskite based solar cell (a) PCE, (b) J_{sc}, (c) V_{oc} and (d) J_0 as a function of number of layers in DM.

C.4.3 Reflectance of DMs on glass

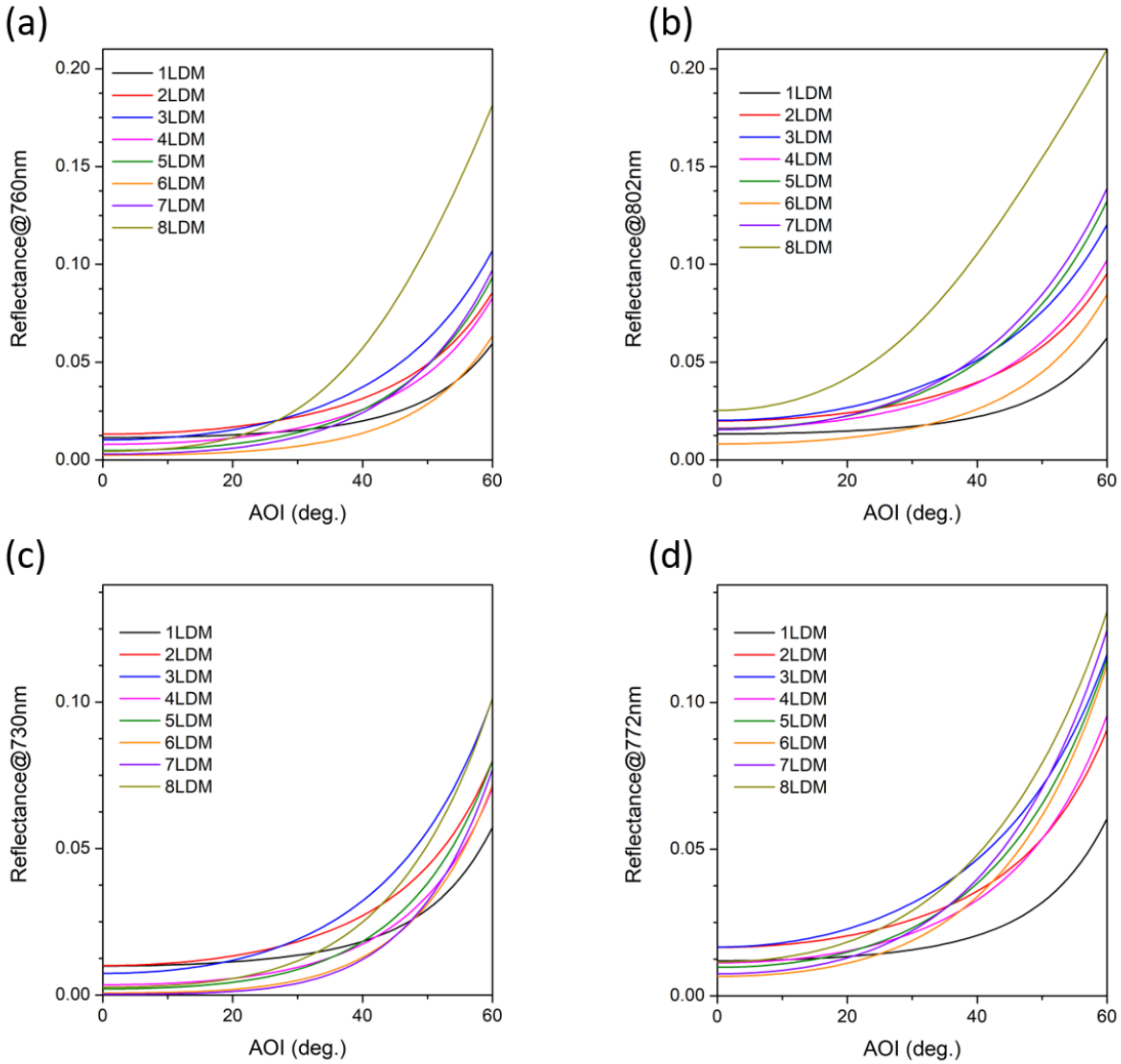

Figure C.6. Total reflectance of DMs on glass for 1.53 eV perovskite solar cell at (a) 760 nm and (b) 802 nm and 1.6 eV perovskite solar cell at (c) 730 nm and (d) 772 nm (PL peak) as a function of angle of incidence for all studied DM configurations.

Appendix D

D.1 Solar cell fabrication

The commercial indium tin oxide glasses (15 Ω/sq) were cleaned with detergent, acetone and ethanol, and then treated by UV−ozone plasma for 15 min. The electron transport layer of SnO_2 nanoparticle solution (20 wt % in water, AlfaAesar) was diluted miliQ water to 2 wt% and put in an ultrasonic bath for 2 min and stirred overnight at 350 rpm. SnO_2 solution was coated on the ITO substrate at 3200 rpm and annealed at 150 °C for 30 min in air. The thickness of the ETL is around 30 nm. The perovskite layer was then deposited by a sequential two-step spin-coating method. First, 1.2 m lead iodide (Sigma-Aldrich, 99%) solution in dimethylformamide (Sigma-Aldrich, 99.8%) and dimethylsulfoxide (VWR, 99.5%) with a 4:1 volume ratio was prepared, adding 2.5 wt% of lead bromide (Sigma-Aldrich, 99.999%) and kept stirring overnight at 200 rpm at 75º C. The second precursor was prepared by mixing 60 mg of formadinium iodide (Sigma-Aldrich, 98%), 6 mg of methylammonium bromide (Sigma-Aldrich, 98%), and 6 mg of methylammonium chlorine (Sigma-Aldrich) in 1 mL of 2-propanol (Scharlau, 99.5%) and kept stirring overnight at 200 rpm and room temperature. The HTL solution was prepared by dissolving 72.3 mg (2,2′,7,7′-tetrakis(N,N-dimethoxyphenylamine)-9,9′-spirobifluorene) (Spiro-OMeTAD, Merck), 28.9 mL 4-tert-butylpyridine (99.9%, Sigma-Aldrich) and 17.5 mL of a stock solution of 520 mg/ mL lithium bis(trifluoromethylsulphonyl)imide in acetonitrile (99.9%, Sigma-Aldrich) in 1 mL chlorobenzene (99.9%, Sigma-Aldrich). The PbI_2 solution was spin-coated onto the ETL at 2000 rpm for 30 s. The second solution was spin-coated onto the PbI_2 at 2000 rpm for 30 s and then annealed at 150 °C for 20 min in air. All layers were prepared in a nitrogen-filled glove box. The ~100 nm thick HTL was deposited by spin-coating the solution at 4000 rpm for 30 s. Samples were kept in the dry air overnight. Finally, the Au (80 nm, 1 Å·s −1) was deposited by thermal evaporation under a pressure of mBar.

D.2 Photovoltaic parameters of fabricated perovskite solar cells

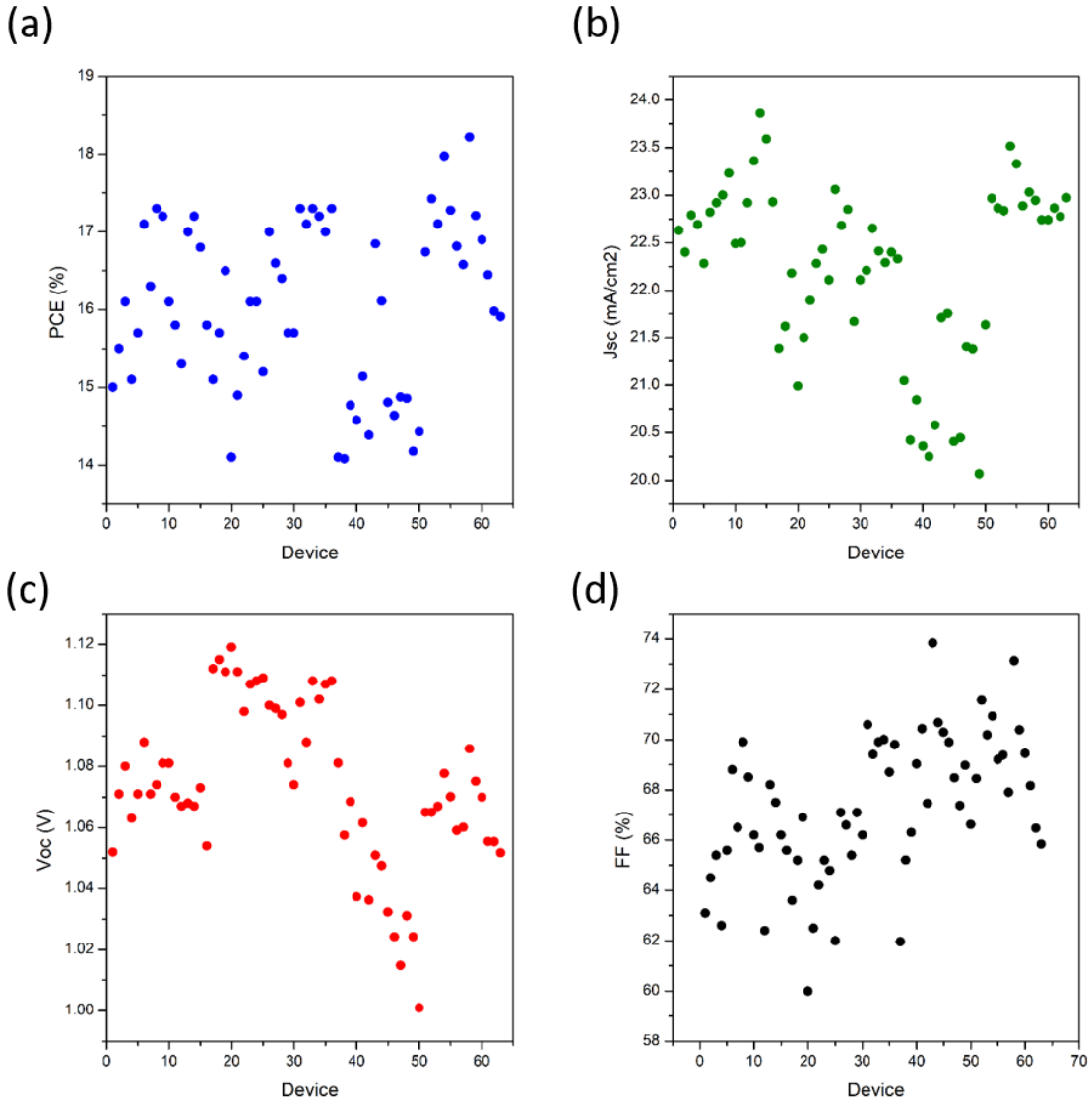

Figure D.1 Photovoltaic parameters of fabricated perovskite solar cells: (a) PCE, (b) J_{sc}, (c) V_{oc} and (d) FF.

D.3 Configurations of dielectric multilayers

Band gap (eV)	**1.2**	**1.35**	**1.4**	**1.53**	**1.6**	**1.7**	**1.78**	**1.85**	**1.9**
Thickness (nm)	94 58 89 64 162 165	98 130 66 162 72 258	97 153 177 160 186 73	90 61 19 56 37 58	86 48 82 63 161 62	81 51 89 160 55 57	81 100 85 32 148 159	81 38 79 127 112 64	80 114 147 7 120 139
Refractive index	1.3 1.7 1.9 1.7 1.5 1.6	1.3 1.7 1.5 1.3 1.4 1.5	1.3 1.6 1.4 1.5 1.4 1.5	1.3 1.9 2.5 2.3 2.0 1.7	1.3 1.8 2.1 1.7 1.4 1.5	1.3 1.8 2.2 2.0 1.8 1.6	1.4 2.2 1.6 1.3 1.6 1.4	1.3 1.8 1.9 1.6 1.8 1.6	1.3 1.8 1.4 1.6 1.7 1.5

Table D.1 Parameters of 6LDMs obtained for all studied perovskite solar cells.

D.4. Photovoltaic parameters of studied perovskite solar cells

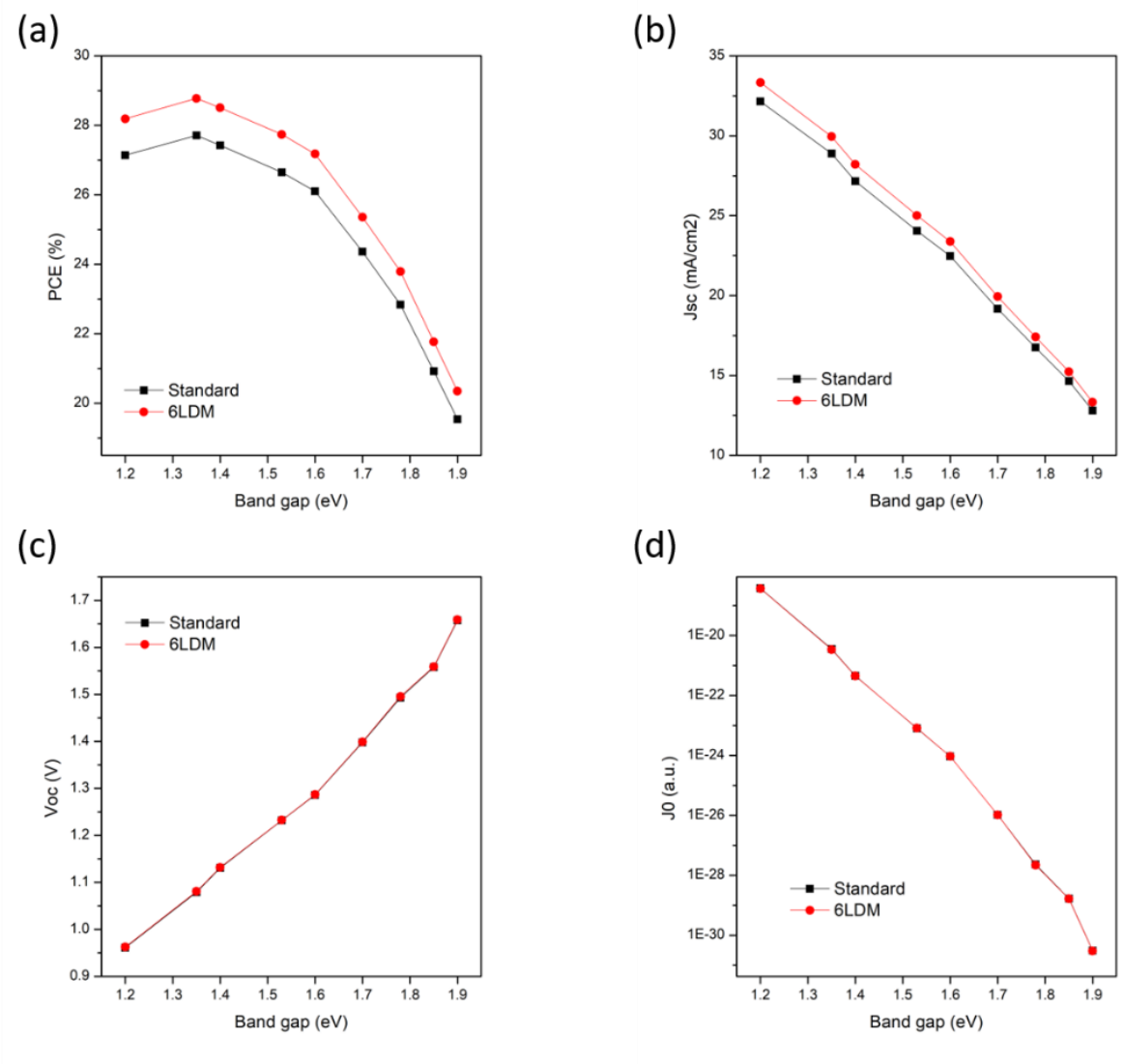

Figure D.2. (a) PCE, (b) J_{sc}, (c) V_{oc} and (d) J_0 as a function of band gap of active layer, with 6LDM (red) and without 6LDM (black).

D.5 Constants for DM

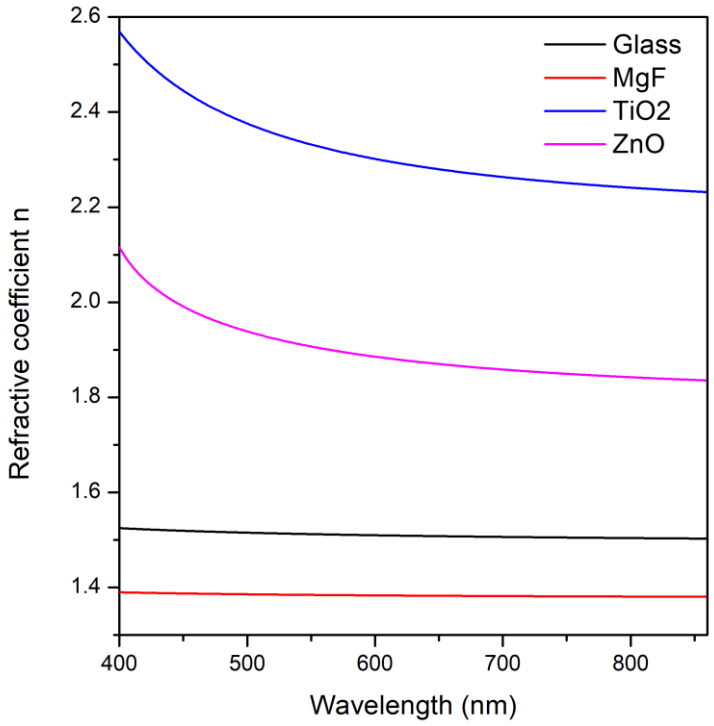

Figure D.3 Refractive index n of material used for DM optimisation. The indexes of other material have been experimentally obtained by ellipsometry.

D.6 Effect of light soaking on perovskite solar cells

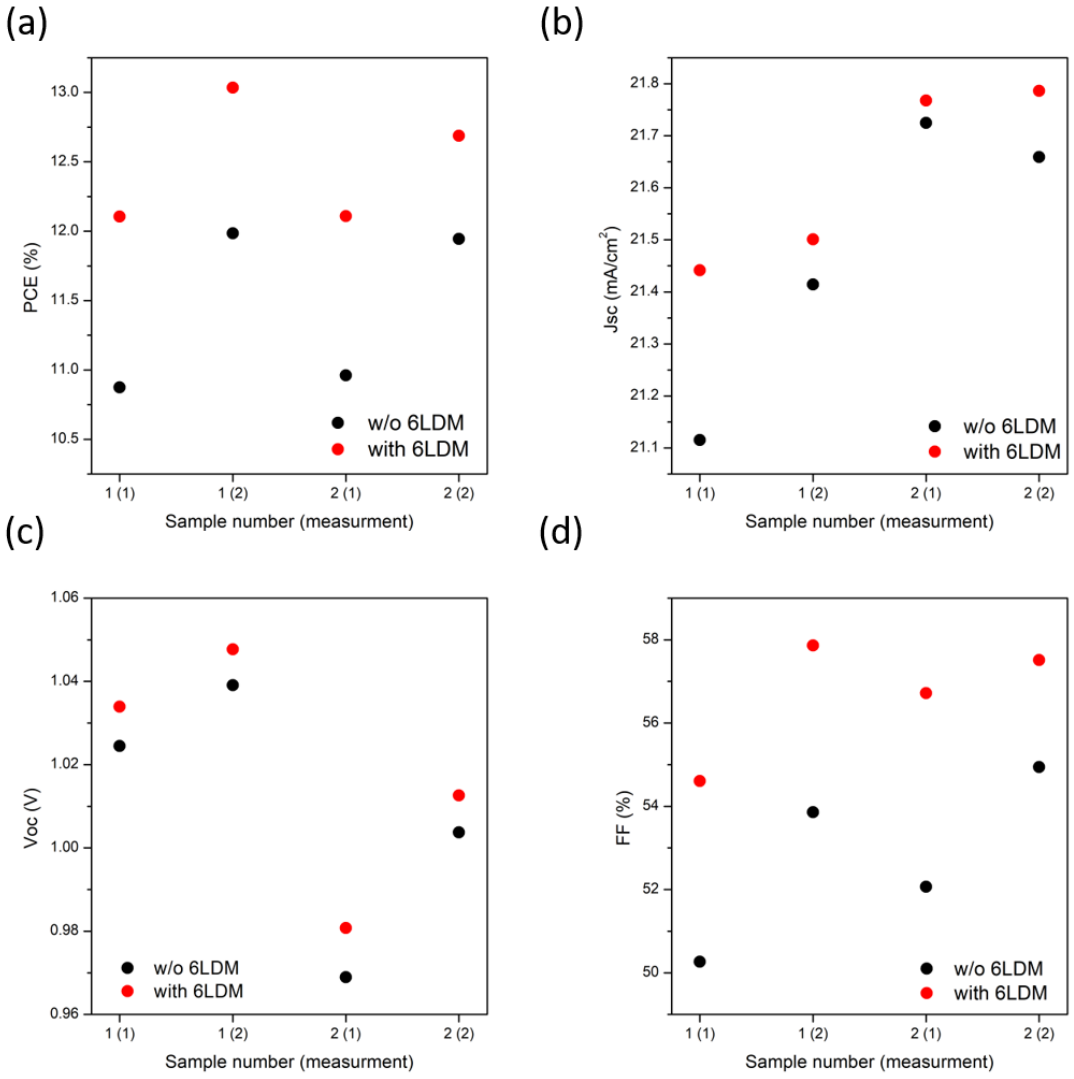

Figure D.4 Experimental (a) PCE, (b) J_{sc}, (c) V_{oc} and (d) FF of two different solar cells measured with and without 6LDM, the measurements have been performed twice as described in the paragraph.

Bibliography

1. International Energy Agency Key World Energy Statistics 2021.
2. World Economic Forum Winning the Race to Net Zero: The CEO Guide to Climate Advantage, 2022.
3. Shockley, W.; Queisser, H. J. Detailed Balance Limit of Efficiency of p-n Junction Solar Cells, J. Appl. Phys. 1961, 32, 510.
4. Green, M. A. Radiative efficiency of state-of-the-art photovoltaic cells, Prog. Photovolt. Res. Appl., 2012, 20, 472.
5. Hirst, L. C.; Ekins-Daukes, N. J. Fundamental Losses in Solar Cells Prog. Photovolt., 2011, 19, 3, 286-293.
6. Kayes, B.; Nie, H.; Twist, R.; Spruytte, S. G.; Reinhardt, F.; Kizilyalli, I.; Higashi, G. 27.6% Conversion Efficiency, a New Record for Single-Junction Solar Cells Under 1 Sun Illumination, Photovoltaic Specialists Conference (PVSC), 2011 37th IEEE.
7. At 26.81%, LONGi Sets a New World Record Efficiency for Silicon Solar Cells LONGi Green Energy Technology Co., Ltd. (LONGi), Institut für Solarenergieforschung in Hameln (ISFH), 2022.
8. Green, M. A.; Dunlop, E. D.; Hohl-Ebinger, J.; Yoshita, M.; Kopidakis, N.; Bothe, K.; Hinken, D.; Rauer, M.; Hao X. Solar Cell Efficiency Tables (Version 60), Prog Photovolt., 2022 30, 7, 687-701.
9. Dai, T.; Cao, Q.; Yang, L.; Aldamasy, M.H.; Li, M.; Liang, Q.; Lu, H.; Dong, Y.; Yang, Y. Strategies for High-Performance Large-Area Perovskite Solar Cells toward Commercialisation. Crystals, 2021, 11, 295.
10. Dkhil, S. B., A Short Overview of the Third-Generation Solar Cells: Concept, Materials, and Performance., 2020.
11. Kojima, A.; Teshima, K.; Shirai, Y.; Miyasaka, T. Organometal Halide Perovskites as Visible-Light Sensitizers for Photovoltaic Cells, J. Am. Chem. Soc., 2009, 131, 17, 6050–6051.
12. Stranks, S. D.; Burlakov, V. M.; Leitjens, T.; Ball, J. M.; Goriely, A.; Snaith, H. Recombination Kinetics in Organic-inorganic Perovskites: Excitons, Free Charges, and Subgap States. Phys. Rev. Appl., 2014, 2, 034007.
13. Braly, I. L.; Quilettes D. W.; Luis M. Pazos-Outón, L. M.; Burke, S.; Ziffer, M.E.; Ginger, D. S.; Hillhouse H. W. Hybrid Perovskite Films Approaching the Radiative Limit

With Over 90% Photoluminescence Quantum Efficiency. Nat. Photonics, 2018, 12, 355-361.

14. Fassl, P.; Lami, V.; Berger, F. J.; Falk, L. M.; Zaumseil J.; Richards, B. S.; Howard, I. A.; Vaynzof, Y.; Paetzold U. W. Revealing the Internal Luminescence Quantum Efficiency of Perovskite Films via Accurate Quantification of Photon Recycling, Matter, 2021, 4, 1391–1412.
15. Eperon, G. E.; Habisreutinger, S. N.; Leijtens, T.; Bruijnaers, B. J.; van Franeker, J. J.; deQuilettes, D. W.; Pathak, S.; Sutton, R. J.; Grancini, G.; Ginger, D. S.; Janssen, R. A. J.; Petrozza, A.; Snaith, H. J. The Importance of Moisture in Hybrid Lead Halide Perovskite Thin Film Fabrication, ACS Nano, 2015, 9, 9, 9380–9393.
16. Sakai, N.; Pathak, S.; Chen, H.-W.; Haghighirad, A. A.; Stranks, S. D.; Miyasaka, T.; Snaith H. J. The Mechanism of Toluene-Assisted Crystallisation of Organic–Inorganic Perovskites for Highly Efficient Solar Cells, J. Mater. Chem. A, 2016, 4, 4464-4471.
17. Sutter-Fella, C. M.; Li, Y.; Amani, M.; Ager, J. W., III; Toma, F. M.; Yablonovitch, E.; Sharp, I. D.; Javey, A. High Photoluminescence Quantum Yield in Band Gap Tunable Bromide Containing Mixed Halide Perovskites. Nano Lett., 2015, 16, 800−806.
18. Wang, J. T.-W.; Wang, Z.; Pathak, S.; Zhang, W.; deQuilettes, D. W.; Wisnivesky-Rocca-Rivarola, F.; Huang, J.; Nayak, P. K.; Patel, J. B.; Yusof, H. A. M.; Vaynzof, Y.; Zhu, R.; Ramirez, I.; Zhang, J.; Ducati, C.; Grovenor, C.; Johnston, M. B.; Ginger, D. S.; Nicholas, R. J.; Snaith, H. J., Efficient Perovskite Solar Cells by Metal Ion Doping, Energy Environ. Sci., 2016, 9, 2892-2901.
19. Noel, N. K.; Abate, A.; Stranks, S. D.; Parrott, E. S.; Burlakov, V. M.; Goriely, A.; Snaith, H. J. Enhanced Photoluminescence and Solar Cell Performance via Lewis Base Passivation of Organic-Inorganic Lead Halide Perovskites. ACS Nano, 2014, 8, 10, 9815 – 9821.
20. deQuilettes, D. W.; Koch, S.; Burke, S.; Paranji, R. K.; Shropshire, A. J.; Ziffer, M. E.; Ginger, D. S. Photoluminescence Lifetimes Exceeding 8 μs and Quantum Yields Exceeding 30% in Hybrid Perovskite Thin Films by Ligand Passivation. ACS Energy Lett., 2016, 1, 438−444.
21. Abdi-Jalebi, M.; Andaji-Garmaroudi, Z.; Cacovich, S.; Stavrakas, C.; Philippe, B.; Richter, J. M.; Alsari, M.; Booker, E. P.; Hutter, E. M.; Pearson, A. J.; et al. Maximising and Stabilising Luminescence from Halide Perovskites with Potassium Passivation. Nature, 2018, 555 (7697), 497−501.

22. Richter, J. M.; Abdi-Jalebi, M.; Sadhanala, A.; Tabachnyk, M.; Rivett, J. P. H.; Pazos-Outon, L. M.; Gödel, K. C.; Dechsler, F.; Friend, R., Enhancing Photoluminescence Yields in Lead Halide Perovskites by Photon Recycling and Light Out-coupling. Nat. Commun., 2016, 7, 13941.
23. Wang, Y.; Guo, S.; Luo, H.; Zhou, C.; Lin, H.; Ma, X.; Hu, Q.; Du, M.; Ma, B.; Yang, W.; Lu, X. Reaching 90% Photoluminescence Quantum Yield in One Dimensional Metal Halide $C_4N_2H_{14}PbBr_4$ by Pressure-Suppressed Nonradiative Loss, J. Am. Chem. Soc., 2020, 142, 16001−16006.
24. Khan, Y.; Ahn, Y.; Lee, H.; Jeong, J.; Shin, Y. S.; Lee, J. S.; Kwon, J. H.; Kim, J. Y.; Kim, H. S.; Seo, J. H.; Walker, Bright. Waterproof Perovskites: High Fluorescence Quantum Yield and Stability from a Methylammonium Lead Bromide/Formate Mixture in Water, J. Mater. Chem. C, 2020,8, 5873-5881.
25. Draguta, S.; Christians J. A.; Morozov Y. V.; Mucunzi, A.; Manser, J. S.; Kamat, P. V.; Luther, J. M.; Kuno, M. A Quantitative and Spatially Resolved Analysis of The Performance-Bottleneck In High Efficiency, Planar Hybrid Perovskite Solar Cells. Energy Environ. Sci., 2018, 11, 960.
26. Liu, Z.; Krückemeier, L.; Krogmeier, B.; Klingebiel, B.; Marque, J. A.; Levcenko, S.; Senol, Ö.; Mathur, S.; Rau, U.; Unold, T.; Kirchartz, T. Open-Circuit Voltages Exceeding 1.26 V in Planar Methylammonium Lead Iodide Perovskite Solar Cells. ACS Energy Lett., 2019, 4, 110−117.
27. NREL (National Renewable Energy Laboratory) Chart of Power Conversion Efficiencies of Best Research Solar Cells, 2022.
28. Steiner, M. A.; Geisz, J. F.; García, I.; Friedman, D. J .; Duda, A.; Kurtz, S. R.; Optical Enhancement of The Open-Circuit Voltage in High Quality GaAs Solar Cells, J. Appl. Phys., 2013, 113, 123109.
29. Kim, J.- H.; Jung, S.; Jeong, I. Optical Modeling for Polarisation-dependent Optical Power Dissipation of Thin-film Organic Solar Cells at Oblique Incidence. J. Opt. Soc. Korea, 2013, 16, 1, 6-12.
30. Kramarenko, M.; Ferreira, C. G.; Martínez-Denegri, G.; Sansierra, C.; Toudert, J.; Martorell, J. Relation Between Fluorescence Quantum Yield and Open-Circuit Voltage in Complete Perovskite Solar Cells, Sol. RRL, 2020, 4, 1900554.
31. Rajagopal, A.; Yang, Z.; Jo, S. B.; Braly, I. L.; Liang, P.-W., Hillhouse, H. W.; Jen, A. K.-Y. Highly Efficient Perovskite-Perovskite Tandem Solar Cells Reaching 80% of The Theoretical Limit in Photovoltage, Adv. Mater., 2017, 29, 34, 1702140.

32. Anaya, M.; Correa-Baena, J. P.; Lozano, G.; Saliba, M.; Anguita, P.; Roose, B.; Abate, A.; Steiner, U.; Grätzel, M.; Calvo, M. E.; Hagfeldtb, A.; Míguez, H. Optical Analysis of $CH_3NH_3Sn_xPb_{1-x}I_3$ Absorbers: a Roadmap for Perovskite-On-Perovskite Tandem Solar Cells, J. Mater. Chem. A, 2016, 4, 11214.

33. Werner, J.; Nogay, G.; Sahli, F.; Yang, T. C.-J.; Bräuninger, M.; Christmann, G.; Walter, A.; Kamino, B. A.; Fiala, P.; Löper, P.; Nicolay, S.; Jeangros, Q.; Niesen, B.; Ballif, C. Complex Refractive Indices of Cesium–Formamidinium-Based Mixed-Halide Perovskites With Optical Band Gaps From 1.5 to 1.8 eV, ACS Energy Lett., 2018, 3, 3, 742–747.

34. Sha, W. E. I.; Ren1 X.; Chen, L.; Choy, W. C. H. The Efficiency Limit of $CH_3NH_3PBI_3$ Perovskite Solar Cells, Appl. Phys. Lett., 2015, 106, 221104.

35. Shao, S.; Liu, J.; Portale, G.; Fang, H.-H.; Blake, G. R.; ten Brink, G. H.; Koster, L. J. A.; Loi M. A. Highly Reproducible Sn-Based Hybrid Perovskite Solar Cells with 9% Efficiency, Adv. Energy Mater., 2018, 8, 4, 1702019.

36. Mohebpour, M. A.; Saffari, M.; Soleimani, H. R.; Tagani, M. B. High Performance of Mixed Halide Perovskite Solar Cells: Role of Halogen Atom and Plasmonic Nanoparticles on the Ideal Current Density of Cell, Phys. E: Low-Dimens. Syst. Nanostructures, 2018, 97, 282-289.

37. Manzoor, S.; Häusele, J.; Bush, K. A.; Palmstrom, A. F.; Carpenter, J.; Yu, Z. J.; Bent, S. F.; Mcgehee, M. D.; Holman, Z. C. Optical Modelling of Wide-Bandgap Perovskite and Perovskite/Silicon Tandem Solar Cells Using Complex Refractive Indices for Arbitrary Bandgap Perovskite Absorbers, Opt. Express, 2018, 26, 21, 27442.

38. B. Wenger, P. K. Nayak, X. Wen, S. V. Kesava, N. K. Noel, H. J. Snaith, Consolidation of the optoelectronic properties of $CH_3NH_3PbBr_3$ perovskite single crystals Nat. Commun., 2017, 8, 590.

39. Palik, E. Handbook of Optical Constants of Solids, 1 ed.; Academic Press, 1997.

40. Huang, J.; Yu, J.; Lin, H.; Jiang, Y. Detailed Analysis of Bathocuproine Layer for Organic Solar Cells Based on Copper Phthalocyanine and C60, J. Appl. Phys., 2009, 105, 073105.

41. Hossain, M. I.; Qarony, W.; Ma, S.; Zeng, L.; Knipp, D.; Tsang, Y. H. Perovskite/Silicon Tandem Solar Cells: From Detailed Balance Limit Calculations to Photon Management, J. Mater. Chem. A, 2018, 6, 3625-3633.

42. Santbergen, R.; Mishima, R.; Meguro, T.; Hino, M.; Uzu, H.; Blanker, J.; Yamamoto, K.; Zeman, M. Minimising Optical Losses In Monolithic Perovskite/C-Si Tandem Solar Cells With A Flat Top Cell, Opt. Express, 2016, 24, A1288-A1299.
43. Miller, O. D.; Yablonovitch, E.; Kurtz, S. R. Strong Internal and External Luminescence as Solar Cells Approach the Shockley–Queisser Limit. IEEE J. Photovolt., 2012, 2, 3, 303-311.
44. Ganapati, V.; Steiner, M. A.; Yablonovitch, E. The Voltage Boost Enabled by Luminescence Extraction In Solar Cells. IEEE J. Photovolt., 2016, 6, 4, 801-809.
45. Pazos-Outón, L. M.; Xiao, T. P.; Yablonovitch, E. Fundamental Efficiency Limit of Lead Iodide Perovskite Solar Cells J. Phys. Chem. Lett., 2018, 9 (7), 1703–1711.
46. Ross, R. T. Some Thermodynamics of Photochemical Systems J. Chem. Phys., 1967, 46, 4590.
47. Rau, U.; Paetzold, U. W.; Kirchartz, T. Thermodynamics Of Light Management In Photovoltaic Devices. Phys. Rev. B, 2014, 98, 035211.
48. Kirchartz, T.; Staub, F.; Rau, U. Impact of Photon Recycling on the Open- Circuit Voltage of Metal Halide Perovskite Solar Cells. ACS Energy Lett., 2016, 1 (4), 731–739.
49. Caprioglio, P.; Stolterfoht, M.; Wolff, C. M.; Unold, T.; Rech, B.; Albrecht, S.; Neher, D. On the Relation between the Open-Circuit Voltage and Quasi-Fermi Level Splitting in Efficient Perovskite Solar Cells Adv. Energy Mater., 2019, 9, 1901631.
50. Zhang, H.; Kramarenko, M.; Martínez-Denegri, G.; Osmond, J.; Toudert, J.; Martorell, J. Formamidinium Incorporation into Compact Lead Iodide for Low Band Gap Perovskite Solar Cells with Open-Circuit Voltage Approaching the Radiative Limit. ACS Appl. Mater. Interfaces, 2019, 11 (9), 9083–9092.
51. Krückemeier, L.; Rau, U.; Stolterfoht, M.; Kirchartz, T. How to Report Record Open-Circuit Voltages in Lead-Halide Perovskite Solar Cells Adv. Energy Mater. 2020, 10, 1902573.
52. Sarritzu, V.; Sestu, N.; Marongiu, D.; Chang, X.; Masi, S.; Rizzo, A.; Colella, S.; Quochi, F.; Saba, M.; Mura A.; Bongiovanni, G. Optical Determination of Shockley-Read-Hall and Interface Recombination Currents in Hybrid Perovskites. Sci. Rep., 2017, 7, 44629.
53. Stolterfoht, M.; Caprioglio, P.; Wolff, C.M.; Marquez, J.A.; Nordmann, J.; Zhang, S.; Rothhardt, D.; Hormann, U.; Redinger, A.; Kegelmann, L.; Albrecht, S.; Kirchartz, T.; Saliba, M.; Unold, T.; Neher, D. The Perovskite/Transport Layer Interfaces Dominate

Non-Radiative Recombination in Efficient Perovskite Solar Cells, arXiv:1810.01333, 2018.

54. Wolff, C. M.; Caprioglio, P.; Stolterfoht, M.; Neher, D. Nonradiative Recombination in Perovskite Solar Cells: The Role of Interfaces Adv. Mater., 2019, 31, 1902762.

55. Zhang, H.; Kramarenko, M.; Osmond, J.; Toudert, J.; Martorell, J. Natural Random Nanotexturing of the Au Interface for Light Backscattering Enhanced Performance in Perovskite Solar Cells. ACS Photonics, 2018, 5, 6, 2243-2250.

56. Martínez-Denegri, G.; Colodrero, S.; Liu, Q.; Toudert, J.; Kozyreff, G.; Martorell, J. Ergodic Light Propagation in a Half-Cylinder Photonic Plate for Optimal Absorption in Perovskite Solar Cells. Adv. Opt. Mater., 2019, 7, 10, 1900018.

57. Yang, W. S.; Park, B. - W.; Jung, E. H.; Jeon, N. J.; Kim, Y. C.; Lee, D. U.; Shin, S. S.; Seo, J.; Kim, E. K.; Noh, J. H.; Seok, S. I. Iodide Management In Formamidinium-Lead-Halide–Based Perovskite Layers For Efficient Solar Cells. Science, 2017, 356, 6345, 1376-1379.

58. Martínez-Denegri, G.; Colodrero, S.; Kramarenko, M.; Martorell, All-Nanoparticle SnO2/TiO2 Electron-Transporting Layers Processed at Low Temperature for Efficient Thin-Film Perovskite Solar Cells J. ACS Appl. Energy Mater., 2018, 1, 10, 5548-5556

59. Leijtens, T.; Eperon, G. E.; Barker, A. J; Grancini, G.; Zhang, W.; Ball, J. M.; Kandada, A. R. S.; Snaith, H. J.; Petrozza, A. Carrier Trapping and Recombination: The Role of Defect Physics in Enhancing the Open Circuit Voltage of Metal Halide Perovskite Solar Cells. Energy Environ. Sci., 2016, 9, 3472.

60. Lee, Y. H.; Luo, J.; Humphry-Baker, R.; Gao, P.; Grätzel, M.; Nazeeruddin, M. K. Unravelling the Reasons for Efficiency Loss in Perovskite Solar Cells. Energy Mater., 2015, 25, 3925–3933.

61. Sherkar, T. S.; Momblona, C.; Gil-Escrig, L.; Ávila, J.; Sessolo, M.; Bolink, H. J.; Koster, L. J. A. Recombination in Perovskite Solar Cells: Significance of Grain Boundaries, Interface Traps, and Defect Ions. ACS Energy Lett., 2017, 2, 5, 1214-1222.

62. Abdi-Jalebi, M.; Dar, M. I.; Senanayak, S. P.; Sadhanala, A.; Andaji-Garmaroudi, Z.; Pazos-Outón, L. M.; Richter, J. M.; Pearson, A. J.; Sirringhaus, H.; Grätzel, M.; Friend, R. H. Charge Extraction Via Graded Doping of Hole Transport Layers Gives Highly Luminescent and Stable Metal Halide Perovskite Devices. Sci. Adv., 2019, 5, 2, eaav2012.

63. Jin, H.; Debroye, E.; Keshavarz, M.; Scheblykin, I. G.; Roeffaers, M. B. J.; Hofkens, J.; Steele, J. A. It's a Trap! On the Nature of Localised States and Charge Trapping in Lead Halide Perovskites Mater. Horiz., 2020, 7, 397.

64. Yablonovitch E. Statistical ray optics. J. Opt. Soc. Am. 1982, 72, 7, 899 – 907.

65. Chen, Q.; Zhou, H.; Song, T. - B.; Luo, S.; Hong, Z.; Duan, H. – S.; Dou, L.; Liu, Y.; Yang, Y. Controllable Self-Induced Passivation of Hybrid Lead Iodide Perovskites toward High Performance Solar Cells. Nano Lett., 2014, 14, 4158−4163.

66. Shi, B.; Yao, X.; Hou, F.; Guo, S.; Li, Y.; Wei, C.; Ding, Y.; Li, Y.; Zhao, Y.; Zhang, X. Unraveling the Passivation Process of PbI_2 to Enhance the Efficiency of Planar Perovskite Solar Cells. J. Phys. Chem. C, 2018, 122, 37, 21269-21276.

67. Jacobsson, T. J.; Correa-Baena, J. – P.; Anaraki, E. H.; Philippe, B.; Stranks, S. D.; Bouduban, M. E. F.; Tress, W.; Schenk, K.; Teuscher, J.; Moser, J. – E.; Rensmo, H.; Hagfeldt, A. Unreacted PbI_2 as a Double-Edged Sword for Enhancing the Performance of Perovskite Solar Cells. J. Am. Chem. Soc., 2016, 138, 32, 10331-10343.

68. Cao, D. H.; Stoumpos, C. C.; Malliakas, C. D.; Katz, M. J.; Farha, O. K.; Hupp, J. T.; Kanatzidis, M. G. Remnant PbI_2, An Unforeseen Necessity In High-Efficiency Hybrid Perovskite-Based Solar Cells? APL Mater., 2014, 2, 091101.

69. Bae, D.; Palmstrom, A.; Roelofs, K.; Mei, B.; Chorkendorff, I.; Bent, S. F.; Vesborg, P. C. K. Tailoring Mixed-Halide, Wide-Gap Perovskites via Multistep Conversion Process. ACS Appl. Mater. Interfaces, 2016, 8, 23, 14301-14306.

70. Wu, N.; Wu, Y.; Walter, D.; Shen, H.; Duong, T.; Grant, D.; Barugkin, C.; Fu, X.; Peng, J.; White, T.; Catchpole, K.; Weber, K. Identifying the Cause of Voltage and Fill Factor Losses in Perovskite Solar Cells by Using Luminescence Measurements. Energy Technol., 2017, 5, 10, 1827-1835.

71. Ren, X.; Wang, Z.; Sha, W. E. I.; Choy, W. C. H. Exploring the Way To Approach the Efficiency Limit of Perovskite Solar Cells by Drift-Diffusion Model. ACS Photonics, 2017, 4, 934−942.

72. Minemoto, T.; Murata, M. Theoretical Analysis On Effect Of Band Offsets In Perovskite Solar Cells. Sol. Energy Mater. Sol. Cells, 2015, 133, 8 – 14.

73. Cho, A. - N.; Park, N. - G. Impact of Interfacial Layers in Perovskite Solar Cells. Chem. Sus. Chem., 2017, 10 (19), 3687-3704.

74. Westbrook, R. J. E.; Sanchez-Molina , I.; Marin-Beloqui, J. M.; Bronstein, H.; Haque, S. A.; Effect of Interfacial Energetics on Charge Transfer from Lead Halide Perovskite to Organic Hole Conductors. J. Phys. Chem. C, 2018, 122, 2, 1326-1332.

75. Zhao, Y.; Li, Q.; Zhou, W.; Hou, Y.; Zhao, Y.; Fu, R.; Yu, D.; Liu, X.; Zhao, Q. Perovskite Self-Passivation with PCBM for Small Open-Circuit Voltage Loss Sol. RRL, 2019, 3, 1800296.

76. Sun, Q.; Fassl, P.; Vaynzof, Y.; Large-Scale Compositional and Electronic Inhomogeneities in $CH_3NH_3PbI_3$ Perovskites and Their Effect on Device Performance ACS Appl. Energy Mater., 2018, 1, 2410−2416.

77. Green, M. A.; Hishikawa, Y.; Dunlop, E. D.; Levi, D. H.; Hohl-Ebinger, J.; Yoshita, M.; Ho-Baillie, A. W. Y. Solar Cell Efficiency Tables (version 53). Prog. Photovoltaics Res. Appl., 2017, 26, 3−12.

78. Bi, D.; Yi, C.; Luo, J.; Decoppet, J. D.; Zhang, F.; Zakeeruddin, S.; Li, X.; Hagfeldt, A.; Grätzel, M. Polymer-templated Nucleation and Crystal Growth of Perovskite Films for Solar Cells with Efficiency Greater than 21%. Nat. Energy, 2016, 1, 16142.

79. Zheng, X.; Chen, B.; Dai, J.; Fang, Y.; Bai, Y.; Lin, Y.; Wei, H.; Zeng, X. C.; Huang, J. Defect Passivation in Hybrid Perovskite Solar Cells Using Quaternary Ammonium Halide Anions and Cations. Nat. Energy, 2017, 2, 17102.

80. Tan, H.; Jain, A.; Voznyy, O.; Lan, X.; García de Arquer, F. P.; Fan, J. Z.; Quintero-Bermudez, R.; Yuan, M.; Zhang, B.; Zhao, Y.; Fan, F.; Li, P.; Quan, L. N.; Zhao, Y.; Lu, Z.-H.; Yang, Z.; Hoogland, S.; Sargent, E. H. Efficient and Stable Solution-processed Planar Perovskite Solar Cells via Contact Passivation. Science, 2017, 355, 722−726.

81. Correa-Baena, J.-P.; Saliba, M.; Buonassisi, T.; Grätzel, M.; Abate, A.; Tress, W.; Hagfeldt, A. Promises and Challenges of Perovskite Solar Cells. Science 2017, 358, 739−744.

82. Eperon, G. E.; Stranks, S. D.; Menelaou, C.; Johnston, M. B.; Herz, L. M.; Snaith, H. J. Formamidinium Lead Trihalide: a Broadly Tunable Perovskite for Efficient Planar Heterojunction Solar Cells. Energy Environ. Sci., 2014, 7, 982−988.

83. Yang, W. S.; Noh, J. H.; Jeon, N. J.; Kim, Y. C.; Ryu, S.; Seo, J.; Seok, S. I. High-Performance Photovoltaic Perovskite Layers Fabricated through Intramolecular Exchange. Science, 2015, 348, 1234−1237.

84. Binek, A.; Hanusch, F. C.; Docampo, P.; Bein, T. Stabilisation of the Trigonal High-temperature Phase of Formamidinium Lead Iodide. J. Phys. Chem. Lett. 2015, 6, 1249−1253.

85. Bi, D.; Tress, W.; Dar, M. I.; Gao, P.; Luo, J.; Renevier, C.; Schenk, K.; Abate, A.; Giordano, F.; Correa Baena, J.-P.; Decoppet, J.- D.; Zakeeruddin, S. M.; Nazeeruddin, M. K.; Grätzel, M.; Hagfeldt, A. Efficient Luminescent Solar Cells Based on Tailored Mixed-Cation Perovskites. Sci. Adv., 2016, 2, e1501170.

86. Saliba, M.; Matsui, T.; Domanski, K.; Seo, J.-Y.; Ummadisingu, A.; Zakeeruddin, S. M.; Correa-Baena, J.-P.; Tress, W. R.; Abate, A.; Hagfeldt, A.; Grätzel, M. Incorporation

of Rubidium Cations into Perovskite Solar Cells Improves the Photovoltaic Performance. Science, 2016, 354, 206−209.

87. Conings, B.; Babayigit, A.; Klug, M. T.; Bai, S.; Gauquelin, N.; Sakai, N.; Wang, J. T.-W.; Verbeeck, J.; Boyen, H.-G.; Snaith, H. J. Universal Deposition Protocol for Planar Heterojunction Solar Cells with High Efficiency Based on Hybrid Lead Halide Perovskite Families. Adv. Mater., 2016, 28, 10701−10709.

88. Zhang, M.; Yun, J. S.; Ma, Q.; Zheng, J.; Lau, C. F. J.; Deng, X.; Kim, J.; Kim, D.; Seidel, J.; Green, M. A.; Huang, S.; Ho-Baillie, A. W. Y. High-efficiency Rubidium-incorporated Perovskite Solar Cells by Gas Quenching. ACS Energy Lett., 2017, 2, 438−444.

89. Weber, O. J.; Charles, B.; Weller, M. T. Phase Behaviour and Composition in the Formamidinium-methylammonium Hybrid Lead Iodide Perovskite Solid Solution. J. Mater. Chem., 2016, 4, 15375− 15382.

90. Ha, S.-T.; Shen, C.; Zhang, J.; Xiong, Q. Laser Cooling of Organic-inorganic Lead Halide Perovskites. Nat. Photonics, 2015, 10, 115−121.

91. Yang, Y.; Yan, Y.; Yang, M.; Choi, S.; Zhu, K.; Luther, J. M.; Beard, M. C. Low Surface Recombination Velocity in Solution-grown $CH_3NH_3PbBr_3$ Perovskite Single Crystal. Nat. Commun., 2015, 6, 7961.

92. Burschka, J.; Pellet, N.; Moon, S.-J.; Humphry-Baker, R.; Gao, P.; Nazeeruddin, M. K.; Grätzel, M. Sequential Deposition as a Route¨to High-performance Perovskite-sensitized Solar Cells. Nature, 2013, 499, 316−319.

93. Chen, H. Two-step Sequential Deposition of Organometal Halide Perovskite for Photovoltaic Application. Adv. Funct. Mater., 2017, 27, 1605654.

94. Liu, T.; Hu, Q.; Wu, J.; Chen, K.; Zhao, L.; Liu, F.; Wang, C.; Lu, H.; Jia, S.; Russell, T.; Zhu, R.; Gong, Q. Mesoporous PbI_2 Scaffold for High-performance Planar Heterojunction Perovskite Solar Cells. Adv. Energy Mater., 2015, 6, 1501890.

95. Xiao, Z.; Dong, Q.; Bi, C.; Shao, Y.; Yuan, Y.; Huang, J. Solvent Annealing of Perovskite-induced Crystal Growth for Photovoltaic device Efficiency Enhancement. Adv. Mater., 2014, 26, 6503−6509.

96. Zheng, H.; Wang, W.; Yang, S.; Liu, Y.; Sun, J. A Facile Way to Prepare Nanoporous PbI_2 Films and their Application in Fast Conversion to $CH_3NH_3PbI_3$. RSC Adv., 2016, 6, 1611−1617.

97. Xiong, H.; DeLuca, G.; Rui, Y.; Li, Y.; Reichmanis, E.; Zhang, Q.; Wang, H. Solvent Vapor Annealing of Oriented PbI_2 Films for Improved Crystallisation of Perovskite Films in the Air. Sol. Energy Mater. Sol. Cells, 2017, 166, 167−175.

98. Ono, L. K.; Juarez-Perez, E. J.; Qi, Y. Progress on Perovskite Materials and Solar Cells with Mixed Cations and Halide Anions. ACS Appl. Mater. Interfaces 2017, 9, 30197−30246.

99. Li, L.; Liu, N.; Xu, Z.; Chen, Q.; Wang, X.; Zhou, H. Precise Composition Tailoring of Mixed-cation Hybrid Perovskites for Efficient Solar Cells by Mixture Design Methods. ACS Nano, 2017, 11, 8804−8813.

100. Zheng, X.; Wu, C.; Jha, S. K.; Li, Z.; Zhu, K.; Priya, S. Improved Phase Stability of Formamidinium Lead Triiodide Perovskite by Strain Relaxation. ACS Energy Lett., 2016, 1, 1014−1020.

101. Pellet, N.; Gao, P.; Gregori, G.; Yang, T.-Y.; Nazeeruddin, M. K.; Maier, J.; Grätzel, M. Mixed-organic-cation Perovskite Photovoltaics For Enhanced Solar-light Harvesting. Angew. Chem., Int. Ed., 2014, 53, 3151−3157.

102. Li, C.; Guo, Q.; Zhang, H.; Bai, Y.; Wang, F.; Liu, L.; Hayat, T.; Alsaedi, A.; Tan, Z. a. Enhancing the Crystallinity of $HC(NH_2)_2PbI_3$ Film by Incorporating Methylammonium Halide Intermediate for Efficient and Stable Perovskite Solar Cells. Nano Energy, 2017, 40, 248−257.

103. Zhou, N.; Shen, Y.; Zhang, Y.; Xu, Z.; Zheng, G.; Li, L.; Chen, Q.; Zhou, H. CsI Pre-intercalation in the Inorganic Framework for Efficient and Stable $FA_{1-x}Cs_xPbI_3(Cl)$ Perovskite Solar Cells. Small, 2017, 13, 1700484.

104. Dong, Q.; Yuan, Y.; Shao, Y.; Fang, Y.; Wang, Q.; Huang, J. Abnormal Crystal Growth in $CH_3NH_3PbI_{3-x}Cl_x$ using a Multi-cycle Solution Coating Process. Energy Environ. Sci., 2015, 8, 2464−2470.

105. Wu, C.-G.; Chiang, C.-H.; Tseng, Z.-L.; Nazeeruddin, M. K.; Hagfeldt, A.; Grätzel, M. High Efficiency Stable Inverted Perovskite Solar Cells without Current Hysteresis. Energy Environ. Sci., 2015, 8, 2725−2733.

106. Fu, Y.; Meng, F.; Rowley, M. B.; Thompson, B. J.; Shearer, M. J.; Ma, D.; Hamers, R. J.; Wright, J. C.; Jin, S. Solution Growth of Single Crystal Methylammonium Lead Halide Perovskite Nanostructures for Optoelectronic and Photovoltaic Applications. J. Am. Chem. Soc., 2015, 137, 5810−5818.

107. Xu, Y.; Zhu, L.; Shi, J.; Lv, S.; Xu, X.; Xiao, J.; Dong, J.; Wu, H.; Luo, Y.; Li, D. Efficient Hybrid Mesoscopic Solar Cells with Morphology-Controlled $CH_3NH_3PbI_{3-x}Cl_x$

Derived from TwoStep Spin Coating Method. ACS Appl. Mater. Interfaces, 2015, 7, 2242−2248.

108. Jiang, F.; Rong, Y.; Liu, H.; Liu, T.; Mao, L.; Meng, W.; Qin, F.; Jiang, Y.; Luo, B.; Xiong, S.; Tong, J.; Liu, Y.; Li, Z.; Han, H.; Zhou, Y. Synergistic Effect of PbI_2 Passivation and Chlorine Inclusion Yielding Open-circuit Voltage Exceeding 1.15V in both Mesoscopic and Inverted Planar $CH_3NH_3PbI_3(Cl)$-based Perovskite Solar Cells. Adv. Funct. Mater., 2016, 26, 8119−8127.

109. Liu, C.; Wang, K.; Yi, C.; Shi, X.; Smith, A. W.; Gong, X.; Heeger, A. J. Efficient Perovskite Hybrid Photovoltaics via Alcoholvapor Annealing Treatment. Adv. Funct. Mater., 2015, 26, 101−110.

110. Tress, W. Perovskite Solar Cells on the Way to their Radiative Efficiency Limit − Insights into a Success Story of High Open-circuit Voltage and Low Recombination. Adv. Energy Mater., 2017, 7, 1602358.

111. Luo, D.; Yang, W.; Wang, Z.; Sadhanala, A.; Hu, Q.; Su, R.; Shivanna, R.; Trindade, G. F.; Watts, J. F.; Xu, Z.; Liu, T.; Chen, K.; Ye, F.; Wu, P.; Zhao, L.; Wu, J.; Tu, Y.; Zhang, Y.; Yang, X.; Zhang, W.; Friend, R. H.; Gong, Q.; Snaith, H. J.; Zhu, R. Enhanced Photovoltage for Inverted Planar Heterojunction Perovskite Solar Cells. Science, 2018, 360, 1442−1446.

112. Jiang, Q.; Chu, Z.; Wang, P.; Yang, X.; Liu, H.; Wang, Y.; Yin, Z.; Wu, J.; Zhang, X.; You, J. Planar-structure Perovskite Solar Cells with Efficiency Beyond 21%. Adv. Mater., 2017, 29, 1703852.

113. Zhao, Y.; Tan, H.; Yuan, H.; Yang, Z.; Fan, J. Z.; Kim, J.; Voznyy, O.; Gong, X.; Quan, L. N.; Tan, C. S.; Hofkens, J.; Yu, D.; Zhao, Q.; Sargent, E. H. Perovskite Seeding Growth of Formamidinium-lead-iodide-based Perovskites for Efficient and Stable Solar Cells. Nat. Commun., 2018, 9, 1607.

114. Jeong, J.; Kim, M.; Seo, J.; Lu, H.; Ahlawat, P.; Mishra, A.; Yang, Y.; Hope, M. A.; Eickemeyer, F. T.; Kim, M.; Yoon, Y. J.; Choi, I. W.; Primera Darwich, B.; Choi, S. J.; Jo, Y.; Le, J. H.; Walker, B.; Zakeeruddin, S. M.; Emsley, L.; Rothlisberger, U.; Hagfeldt, A.; Kim, D. S.; Grätzel, M.; Kim, J. Y. Pseudo-halide Anion Engineering for α-$FAPbI_3$ Perovskite Solar Cells, Nature, 2021, 592, 381–385.

115. Wang, X.; Rakstys, K.; Jack, K.; Jin, H.; Lai, J.; Li, H.; Kumara Ranasinghe, C. S.; Saghaei, J.; Zhang, G.; Burn, P. L.; Gentle, I. R.; Shaw, P. E. Engineering Fluorinated-cation Containing Inverted Perovskite Solar Cells with an Efficiency of >21% and Improved Stability Towards Humidity, Nat. Commun., 2021,12, 52.

116. Patel, J. B.; Wright, A. D.; Lohmann, K. B.; Peng, K.; Xia, C. Q.; Ball, J. M.; Noel, N. K.; Crothers, T. W.; Wong-Leung, J.; Snaith, H. J.; Herz, L. M.; Johnston, M. B. Light Absorption and Recycling in Hybrid Metal Halide Perovskite Photovoltaic Devices, Adv. Energy Mater., 2020, 10, 1903653.

117. Zhou, Q.; Karani, A.; Lian, Y.; Zhao, B.; Friend, R. H.; Di, D. Photonically-Confined Solar Cells: Prospects for Exceeding The Shockley-Queisser Limit, Arxiv: 2106.04391, 2021.

118. Zhao, Y.; Li, Q.; Zhou, W.; Hou, Y.; Zhao, Y.; Fu, R.; Yu, D.; Liu, X.; Zhao, Q. Double-side-passivated Perovskite Solar Cells with Ultra-low Potential Loss. Sol. RRL 2018, 3, 1800296.

119. Brenes, R.; Laitz, M.; Jean, J.; de Quilettes, D. W.; Bulović, V. Benefit from Photon Recycling at The Maximum-Power Point of State-Of-The-Art Perovskite Solar Cells, Phys. Rev. Applied, 2019, 12, 014017.

120. Abebe, M. G.; Abass, A.; Gomard, G.; Zschiedrich, L.; Lemmer, U.; Richards, B. S.; Rockstuhl, C.; Paetzold, U. W. Rigorous Wave-Optical Treatment of Photon Recycling in Thermodynamics of Photovoltaics: Perovskite Thin-Film Solar Cells, Phys. Rev. B 98, 2018, 075141.

121. Yang, Z.; Rajagopal, A.; Jen, A. K.-Y. Ideal Bandgap Organic–Inorganic Hybrid Perovskite Solar Cells, Adv. Mater., 2017, 29, 1704418.

122. Grånäs, O.; Vinichenko, D.; Kaxiras, E. Establishing The Limits Of Efficiency of Perovskite Solar Cells From First Principles Modelling, Sci. Rep., 2016, 6, 36108.

123. Koç, M.; Soltanpoor, W.; Bektaş, G.; Bolink, H. J.; Yerci, S. Guideline for Optical Optimisation of Planar Perovskite Solar Cells, Adv. Opt. Mater., 2019, 7, 23, 1900944.

124. Li, L.; Zhang, F.; Hao, Y.; Sun, Q.; Li, Z.; Wang, H.; Cui, Y.; Zhu, F. High Efficiency Planar Sn–Pb Binary Perovskite Solar Cells: Controlled Growth of Large Grains via a One-Step Solution Fabrication Process, J. Mater. Chem. C, 2017, 5, 2360-2367.

125. Zhang, W.; Li, X.; Fu, S.; Zhao, X.; Feng, X.; Fang, J. Lead-lean and MA-free Perovskite Solar Cells with an Efficiency over 20%, Joule, 2021, 5, 2904–2914.

126. Guo, W.; Zhu, Y.; Zhang, M.; Du, J.; Cen, Y.; Liu, S.; He, Y.; Zhong, H.; Wanga, W.; Shi, J. The Dion–Jacobson Perovskite CsSbCl4: a Promising Pb-free Solar Cell Absorber with Optimal Bandgap ~ 1.4 eV, Strong Optical Absorption ~10^5 cm^{-1} , and Large Power-Conversion Efficiency Above 20%, J. Mater. Chem. A, 2021, 9, 16436.

127. Reza, K. M.; Maruf, A. A. ; Zhou, Y. ; Qiao, Q. ; Logue, B. Morphology Control by Optimising Process Conditions for Efficient Wide-Bandgap Perovskite Solar Cells, APS March Meeting, 2021, abstract id.H71.085

128. Wang, J.; Zhang, J.; Zhou, Y.; Liu, H.; Xue, Q.; Li, X.; Chueh, C.-C.; Hin-Lap Yip, H.-L.; Zonglong Zhu, Z.; Jen, A. K. Y., Highly Efficient All-Inorganic Perovskite Solar Cells with Suppressed Non-Radiative Recombination by a Lewis Base, Nat. Commun., 202, 11, 177.

129. Guo, Z.; Jena, A. K.; Takei, I.; Kim, G. M.; Kamarudin, M. A.; Sanehira, Y.; Ishii, A.; Numata, Y.; Hayase, S.; Miyasaka, T. V_{oc} Over 1.4 V for Amorphous Tin-Oxide-Based Dopant-Free $CsPbI_2Br$ Perovskite Solar Cells, J. Am. Chem. Soc. 2020, 142, 21, 9725–9734.

130. Aktas, E.; Phung, N.; Köbler, H.; González, D. A.; Méndez, M.; Kafedjiska, I.; Turren-Cruz, S. H.; Wenisch, R.; Lauermann, I.; Abate, A.; Palomares, E. Understanding The Perovskite/Self-Assembled Selective Contact Interface for Ultra-Stable and Highly Efficient p–i–n Perovskite Solar Cells, Energy Environ. Sci., 2021, 14, 3976-3985.

131. Zai, H.; Su, J.; Zhu, C.; Chen, Y.; Ma, Y.; Zhang, P.; Ma, S.; Zhang, X.; Xie, H.; Fan, R.; Huang, Z.; Li, N.; Zhang, Y.; Li, Y.; Bai, Y.; Gao, Z.; Wang, X.; Hong, J.; Sun, K.; Chang, J.; Zhou, H.; Chen, Q. Sandwiched Electrode Buffer for Efficient and Stable Perovskite Solar Cells with Dual Back Surface Fields Joule, 2021, 5, 8, 2148-2163.

132. Z. Chen, Q. Dong, Y. Liu, C. Bao, Y. Fang, Y. Lin, S. Tang, Q. Wang, X. Xiao, Y. Bai, Y. Deng, J. Huang, Thin Single Crystal Perovskite Solar Cells to Harvest Below-Bandgap Light Absorption, Nat. Commun., 2017 8, 1890.

133. Miloud, K. A.; Abdellah, K. ; Ahmed, H. Performances Study of Multi-Layer Linear Gradient Index Antireflective Based on Oxynitride Silicon, Journal of the Technical University Fundamental Sciences and Applications Vol. 22, 2016.

134. Shockley, W.; Read Jr., W.T. Statistics of the Recombinations of Holes and Electrons Phys. Rev., 1952, 87, 835.

135. Sah, C.T.; Noyce, R.N.; Shockley, W. Carrier Generation and Recombination in P-N Junctions and P-N Junction Characteristic Proc. IRE, 1957, 45, 1228-1243.